Dissertation ETH Nr. 15983

Measurement of the W Boson Polarisation using the L3 Detector at LEP II

A dissertation submitted to the
SWISS FEDERAL INSTITUTE OF TECHNOLOGY ZÜRICH

for the degree of
Doctor of Sciences

presented by

Radoslaw Adrian Ofierzynski

Dipl.-Phys. ETH-Zürich

born November 29th, 1973

citizen of Poland

accepted on the recommendation of

Prof. Dr. F. Pauss   examiner
Prof. Dr. A. Rubbia   co-examiner
Dr. M. Dittmar   co-examiner

- 2005 -

Seite Leer /
Blank leaf

Contents

Abstract

The three different helicity states of W bosons produced in the reaction $e^+e^- \rightarrow$ $W^+W^- \rightarrow \ell\nu q_1\bar{q}_2$ at LEP are studied in a model independent way using leptonic and hadronic W decays. Data at centre-of-mass energies $\sqrt{s} = 183 - 209$ GeV, corresponding to a luminosity of 630 pb^{-1}, are used to measure the polarisation of W bosons. The fraction of longitudinally polarised W bosons is measured to be $(21.8 \pm 2.7 \pm 1.6)\%$ where the first uncertainty is statistical and the second systematic, in agreement with the Standard Model expectation of $(24.1 \pm 0.3)\%$.

Separate measurements in $e\nu q_1\bar{q}_2$ and $\mu\nu q_1\bar{q}_2$ samples are found to be in agreement with each other. Separate measurements of W^- and W^+ samples are performed, their results are in agreement with CP invariance. The helicity fractions are shown to vary strongly over the W^- boson scattering angle with respect to the e^- beam direction, in agreement with the Standard Model.

The model independent method is also used to study correlations of the spin of W bosons. The variations of the W helicity states measured with leptonic W decays are investigated by enhancing or reducing the fraction of transversely polarised W bosons which decay into hadrons. Indications of spin correlations, never observed before, are found.

In addition, the correlations between the W decay planes are studied in $e^+e^- \rightarrow$ $W^+W^- \rightarrow \ell\nu q_1\bar{q}_2$ and $e^+e^- \rightarrow W^+W^- \rightarrow q_1\bar{q}_2 q_3\bar{q}_4$ events. These are found to be consistent with expectations.

Seite Leer /
Blank leaf

Zusammenfassung

Die drei verschiedenen Helizitätszustände von W Bosonen, erzeugt in der Reaktion $e^+e^- \to W^+W^- \to \ell\nu q_1\bar{q}_2$ am LEP Beschleuniger, werden mit Hilfe einer modellunabhängigen Methode in leptonischen und hadronischen W Zerfällen untersucht. Die Messungen werden durchgeführt unter Verwendung von Daten, die bei Schwerpunktsenergien von $\sqrt{s} = 183 - 209$ GeV genommen wurden, was einer Luminosität von 630 pb^{-1} entspricht. Der Anteil von longitudinal polarisierten W Bosonen wurde gemessen als $(21.8 \pm 2.7 \pm 1.6)\%$, wobei die erste Unsicherheit statistisch, die zweite systematisch ist, in Übereinstimmung mit der Vorhersage des Standardmodells von $(24.1 \pm 0.3)\%$.

Getrennte Messungen werden mit $e\nu q_1\bar{q}_2$ und $\mu\nu q_1\bar{q}_2$ Endzuständen gemacht, und deren Ergebnisse stimmen überein. Getrennte Messungen der Helizität von W^- und W^+ Bosonen werden vorgestellt, deren Ergebnisse in Übereinstimmung mit CP Invarianz sind. Es wird gezeigt, dass die Anteile der verschiedenen Helizitätszustände stark mit dem Streuwinkel des W^- Bosons variieren, in Übereinstimmung mit dem Standardmodell.

Die modellunabhängige Messmethode wird auch für Messungen von Spinkorrelationen von W Bosonen verwendet. Die Variation der Helizitätszustände von W Bosonen, gemessen in leptonischen W Zerfällen, wird untersucht indem der Anteil der transversal polarisierten hadronisch zerfallenden W Bosonen erhöht oder reduziert wird. Anzeichen für Spinkorrelationen werden zum ersten Mal beobachtet.

Ausserdem werden Korrelationen zwischen den Zerfallsebenen der W Bosonen in den Reaktionen $e^+e^- \to W^+W^- \to \ell\nu q_1\bar{q}_2$ und $e^+e^- \to W^+W^- \to q_1\bar{q}_2 q_3\bar{q}_4$ untersucht. Die gemessenen Korrelationen zwischen den Zerfallsebenen stimmen mit der Erwartung überein.

Introduction

The Standard Model of electroweak interactions as it stands today was developed 30 years ago as an interpretation of experimental results. Since then, it has been a very successful theory to describe the world of particle physics. The Standard Model can be used to obtain predictions for many processes. The goal of an experimental particle physicist is to ask new physics questions allowing him to see whether the Standard Model gives the right answers. Another goal is to find answers to questions for which the Standard Model has intrinsically no answer, *i.e.* to measure parameters of the Standard Model, and to find new phenomena, usually new particles which are either assumed to exist, like the Higgs-boson, or need to be interpreted in the framework of new theories like the Supersymmetry.

During the last 30 years, not only have the W and the Z bosons been discovered at CERN, but also a vast number of tests of the Standard Model, measurements and searches, have been performed. Measurements have been performed not only at LEP (e^+e^- collider), but are also being performed at various hadron-hadron or electron-hadron colliders like the Tevatron, HERA and in future the LHC. Experiments are performed to test the neutrino sector (Gran Sasso Experiments, Super Kamiokande, SNO). The physics of the b quark was studied at LEP and specialised questions are explored at b-factories like BaBar and Belle. The LEP collider was built in order to study first electroweak physics around the Z pole. Then, in its second phase, the beam energy was raised above the threshold for W-pair production and many parameters of the W boson could be measured to a high precision. Searches have been performed for the Higgs particle and for other phenomena.

From this point of view, the work presented in this thesis is a small part of the tests of the Standard Model. Even if the Higgs particle has so far not been observed directly, another consequence of the Higgs theory can be checked: the longitudinal W boson. This helicity state is created as a consequence of electroweak symmetry breaking, the additional longitudinal degree of freedom being taken from one of the vanishing Goldstone bosons.

In this thesis, the polarisation of the W bosons in W-pair events is measured, and a search for W-spin correlations and decay-plane correlations is performed. Some correlations are expected in the Standard Model and are accessible with the size of the data sample collected at LEP. While other measurements, like the studies of triple-gauge-couplings ZWW and γWW or the measurement of the W boson spin density matrix, have an implicit sensitivity to the polarisation fractions and spin correlations, the aim of the presented analysis is a direct and model independent measurement. This study

1

2

also introduces a new technique for the measurement of spin-correlations which could be exploited at future high-luminosity lepton colliders.

Generally, two different strategies can be applied for measurements. Either the raw data distributions can be compared to fully simulated and reconstructed Monte Carlo events combined with background events. This allows to make statements on the agreement between data and Monte Carlo. By using different types of Monte Carlo with possible new physics implemented, conclusions can also be made on limits for this new physics.

For the present measurements, we chose to correct the raw data distributions back to a "generated" level. This method has the advantage that the corrected distributions can be compared directly to distributions generated by any Monte Carlo program or even calculations based on analytical formulæ. The corrected data are what can be used by other physicists. They allow not only to make a statement on the agreement with a Monte Carlo generator, but also to measure numbers which can be used directly for comparison with theoretical models.

A first measurement of W polarisation fractions was performed before this thesis. The L3 paper [1] focuses on the measurement of W polarisation fractions at centre-of-mass energies of $\sqrt{s} = 183$ and 189 GeV. In my diploma thesis [2], ways were studied to search for W-spin and decay-plane correlations, and a first measurement was performed at centre-of-mass energies $\sqrt{s} = 183 - 202$ GeV.

The enlarged statistics collected with L3 at centre-of-mass energies up to 209 GeV allows to update the previous measurements with higher accuracy and to perform detailed systematic studies. The analysis methods were optimised to account for the higher precision which is possible with an enlarged data sample. Finally, it was possible to check the previously observed slight disagreement between Standard Model Monte Carlo and the data in W-spin correlations [2]. The tests and measurements described in this thesis were published in [3, 4].

This thesis is structured as follows: In Chapter 1, a short overview of the Standard Model and experimental tests is given. After a theoretical introduction in Chapter 2, describing the investigated processes and the theoretical formalism for the calculation, Chapter 3 describes the experimental apparatus used to collect the data. Chapter 4 discusses the selection of the event samples to be analysed. Chapter 5 describes the analysis of W helicity states, Chapter 6 the analysis of W spin correlations in flight direction. The analysis of W decay plane correlations is discussed in Chapter 7. A summary and conclusions are given in Chapter 8.

Chapter 1

The Standard Model and W Physics

1.1 The Standard Model

The Standard Model of electroweak interactions [5, 6, 7] and the theory of strong inter-actions describe three out of the four basic forces which are known: the electromagnetic, the weak and the strong interactions. Up to now it has not been possible to describe the fourth force, gravity, as a field theory. Gravity is therefore not included in the Standard Model. Besides this, gravity is too weak to play a role at the masses and energies considered in Particle Physics. In the following, the relevant principles of the Standard Model are presented, following the formalism in standard books like [8].

1.1.1 Particles and Forces

The scenario of the Standard Model is made up of two types of particles: fermions and gauge bosons. Fermions are the constituents of matter and have spin $\frac{1}{2}$. The interactions between the fermions are mediated in the Standard Model by gauge fields which couple to the fermions. The carriers of the interactions are the gauge bosons, the quantum units of the gauge fields. They have spin 1. Three families of elementary particles, which constitute matter, are known. Each of these families consists of two leptons and two quarks, the constituents of the nucleons. Additionally, each of the leptons and quarks has an anti-particle, differing from the particle only in the electrical charge which is opposite. While QCD is limited to the quark sector only, the electroweak theory applies to quarks and leptons.

The formalism of the Standard Model consists of the symmetry group $SU(3)_C$ of QCD and the symmetry group $SU(2)_L \times U(1)_Y$ of the electroweak theory. In group theory, the gauge bosons correspond to the elements of the basic representation of the corresponding symmetry group. Hence the number of gauge bosons for each interaction is determined by the dimension of the group. The gauge bosons of the electroweak theory are the three massive bosons W^+, W^- and Z and the massless photon, γ.

	family			T_3	Y	Q
	1	2	3			
leptons	$\begin{pmatrix} \nu_e \\ e \end{pmatrix}_L$	$\begin{pmatrix} \nu_\mu \\ \mu \end{pmatrix}_L$	$\begin{pmatrix} \nu_\tau \\ \tau \end{pmatrix}_L$	$+1/2$ $-1/2$	-1 -1	0 -1
	e_R	μ_R	τ_R	0	-2	-1
quarks	$\begin{pmatrix} u \\ d \end{pmatrix}_L$	$\begin{pmatrix} c \\ s \end{pmatrix}_L$	$\begin{pmatrix} t \\ b \end{pmatrix}_L$	$+1/2$ $-1/2$	$+1/3$ $+1/3$	$+2/3$ $-1/3$
	u_R	c_R	t_R	0	$+4/3$	$+2/3$
	d_R	s_R	b_R	0	$-2/3$	$-1/3$

Table 1.1: Leptons and quarks and their electroweak quantum numbers: the third component of the weak isospin, T_3, the weak hypercharge Y and the electromagnetic charge, Q. The subscripts L and R indicate left- and right-handedness. In the Standard Model, the left-handed fermions constitute a doublet, the right-handed fermions singlets of the symmetry group $SU(2)_L$.

1.1.2   The Electroweak Theory

The description of weak interactions is based on the symmetry group $SU(2)_L$ with the Pauli-matrices as generators. Following experimental evidence from beta-decay, we know that the weak force couples only to left-handed fermions and right-handed anti-fermions (V-A interaction). While the left-handed fermions are grouped into doublets of the weak isospin T, right-handed fermions are singlets of the weak isospin. Table 1.1 summarises the leptons and quarks together with their quantum numbers.

The weak eigenstates d', s' and b' of the quark field are not identical to the mass eigenstates d, s and b. However, they are linked directly via a rotation, which is described by the Cabibbo-Kobayashi-Maskawa (CKM) matrix:

$$\begin{pmatrix} d' \\ s' \\ b' \end{pmatrix} = V_{CKM} \begin{pmatrix} d \\ s \\ b \end{pmatrix} \tag{1.1}$$

The electromagnetic charge, the weak isospin and the weak hypercharge are linked by the Gell-Mann Nishijima equation:

$$Q = T_3 + \frac{Y}{2} . \tag{1.2}$$

The fermions are solutions of the Dirac-equation and the description of their interactions is based on the principle of gauge invariance. The Dirac equation must be invariant under local gauge transformations:

$$\psi \longrightarrow \psi' = \exp\left(-ig\vec{T}\vec{W}^\mu - ig'\frac{Y}{2}B^\mu \right) \psi . \tag{1.3}$$

The operators $\vec{T}$ and Y are the generators of $SU(2)_L$ and $U(1)_Y$ which act on the weak isospin and the hypercharge of the fields, and g and g' are the coupling strengths of $SU(2)_L$

and U(1)$_Y$, respectively. The gauge transformation is generated by the triplet of gauge fields W_1^μ, W_2^μ and W_3^μ of the group SU(2)$_L$ and the gauge field B^μ of the group U(1)$_Y$. The invariance of the Dirac equation requires the introduction of the covariant derivative

$$D^\mu = \partial^\mu + ig\vec{T}\vec{W}^\mu + ig'\frac{Y}{2}B^\mu \ . \tag{1.4}$$

The physical boson fields follow from a rotation of the gauge fields. The field of the photon is given by the expression

$$A^\mu = B^\mu \cos\theta_W + W_3^\mu \sin\theta_W \ , \tag{1.5}$$

with the coupling strength to an electron which corresponds to the elementary charge e. g and g' are linked to the elementary charge via the weak mixing angle θ_W:

$$e = g\sin\theta_W = g'\cos\theta_W \ . \tag{1.6}$$

The weak neutral current is orthogonal to the photon current

$$Z^\mu = -B^\mu \sin\theta_W + W_3^\mu \cos\theta_W \ , \tag{1.7}$$

while the fields of the weak charged current are a linear combination of the remaining two generators of SU(2)$_L$

$$W^{\pm\mu} = \frac{1}{\sqrt{2}}\left(W_1^\mu \mp W_2^\mu\right) \ . \tag{1.8}$$

1.1.3 The Higgs Sector of the Standard Model

To generate the masses of the particles without destroying the renormalisability of the electroweak theory, a spontaneous symmetry breaking is needed. In the Standard Model, this happens through the introduction of a scalar field, the so-called Higgs field. The masses of particles are generated via the coupling to this field.
The Higgs field is described by the Lagrangian

$$\mathcal{L}_{\text{Higgs}} = (D^\mu\phi)^\dagger D_\mu\phi + \mu^2\phi^\dagger\phi - \lambda(\phi^\dagger\phi)^2 \ . \tag{1.9}$$

The Higgs field consists of two complex fields which are a doublet of weak isospin with the hypercharge $Y(\phi) = 1$. According to the Gell-Mann-Nishijima relation from Equation 1.2, the upper field is charged while the lower one is neutral:

$$\phi = \begin{pmatrix} \phi^+ \\ \phi^0 \end{pmatrix} \ . \tag{1.10}$$

The potential of the Higgs field has a non-zero minimum at

$$\frac{v^2}{2} = \frac{\mu}{2\lambda} \ . \tag{1.11}$$

Because of gauge invariance, the choice of the vacuum expectation value is limited by the requirement that the charged component must vanish. The ground state is thus

$$\langle 0|\phi|0\rangle = \frac{1}{\sqrt{2}} \begin{pmatrix} 0 \\ v \end{pmatrix} . \tag{1.12}$$

This choice of the phase corresponds to a global gauge and breaks the gauge invariance spontaneously.

After symmetry breaking, three out of four of the degrees of freedom of the complex Higgs field are absorbed in the gauge boson sector as the additional helicity 0 (called longitudinally polarised) states of the W^+, W^- and Z. This also means that these gauge bosons obtain a mass, while the photon stays massless, which is in agreement with observation. Due to the rotation of the gauge fields, the weak mixing angle appears in the expressions for the W and Z boson masses:

$$m_W = \frac{gv}{2} = \frac{ev}{2\sin\theta_W} , \tag{1.13}$$

$$m_Z = \frac{\sqrt{g^2 + g'^2}\, v}{2} = \frac{ev}{2\sin\theta_W \cos\theta_W} . \tag{1.14}$$

The weak mixing angle thus relates directly the masses of the heavy gauge bosons:

$$\sin^2\theta_W = 1 - \frac{m_W^2}{m_Z^2} . \tag{1.15}$$

The mass of the scalar Higgs boson which remains after the symmetry breaking is given by the expression:

$$m_H = \sqrt{2\lambda}\, v . \tag{1.16}$$

Fermion masses may be generated with the same mechanism. The left-handed fermion doublets and the right-handed singlets are given Yukawa couplings with the Higgs field. This results in an additional term in the Standard Model Lagrangian. For example, the gauge invariant term for the first fermion family is:

$$\mathcal{L}_{\text{Yukawa}} = -\frac{v + H}{\sqrt{2}} (g_\nu \bar{\nu}_e \nu_e + g_e \bar{e}e + g_u \bar{u}u + g_d \bar{d}d) , \tag{1.17}$$

and a corresponding mass term for each fermion: $m_f = v g_f/\sqrt{2}$.

1.1.4   Spin, Helicity and Polarisation of Gauge Bosons

The fundamental particles - leptons and quarks - have spin one half, while the force-carrying bosons, hence also W bosons, have spin one. We define the normalised projection of the spin on the flight direction of the particle as the helicity of the particle:

$$h = \frac{\vec{s} \cdot \vec{p}}{|\vec{s}| \cdot |\vec{p}|} . \tag{1.18}$$

Thus fermions can have helicity ± 1, while the massive W and Z bosons can have helicity ± 1 or 0. Massless bosons like photons and gluons can not exist in a helicity 0 state. Virtual photons or gluons however do have mass, so they can also exist in the helicity 0 state. Particles with helicity ± 1 are called transversely polarised, particles with helicity 0 longitudinally polarised [1].

What makes the helicity 0 state so interesting is exactly the fact that only massive bosons can be in this state. The Higgs-mechanism, through which particles acquire mass, generates also the longitudinal polarisation. This fact is expressed in the equivalence theorem [9, 10]: The amplitude for emission or absorption of a longitudinally polarised gauge boson becomes equal to the amplitude for emission or absorption of the Goldstone boson that was eaten during electroweak symmetry breaking. This Goldstone boson is often called the "Higgs ghost".

1.2 Tests of the Electroweak Standard Model

The most important confirmation for the electroweak theory was the discovery of the W and Z boson by the UA1 and UA2 collaborations at the CERN SPS collider [11, 12, 13, 14]. The picture of the Standard Model and its particles was rounded off by the direct evidence for the top-quark by the CDF and D0 collaborations [15, 16] and the tau-neutrino by the DONUT collaboration [17]. However, the Higgs boson has not been observed yet.

Precision tests have been performed at the LEP and SLC colliders. The LEP collider was built to study the electroweak part of the Standard Model in the process $e^+e^- \to Z$ and, at a later stage called LEP II, to probe the electroweak physics at higher energies.

An e^+e^- collider has several advantages compared to hadron colliders, which allows the study of many aspects of the Standard Model in detail, and also simplifies the search for new physics. First of all, the entire event (apart from initial state radiation going along the beam-pipe) can be captured in a detector and the centre-of-mass energy is well known. This allows for the full kinematic information to be used in the analysis. In addition, the Standard Model processes at e^+e^- colliders have a relatively simple topology and many rates are precisely calculable, thus allowing Standard Model parameters like $\sin^2 \theta_W$ and the W and Z boson masses to be constrained. At LEP II energies, the largest cross-sections are those of $\gamma\gamma$ collisions and the radiative annihilation process $e^+e^- \to Z\gamma \to q\bar{q}(\gamma)$, which proceeds via a recoil Z. Even if these processes constitute background for many studies and searches for new phenomena, they can be strongly reduced by using simple cuts on the visible energy or on the number of jets. Furthermore, at e^+e^- colliders, a typical cross-section is of the order of the square of the gauge charges times the QED cross-section of the $e^+e^- \to \mu^+\mu^-$ process:

$$\sigma_{\mu^+\mu^-} = \frac{4\pi\alpha^2}{3s} = \frac{86.8\text{nb}}{(E_{CM}(\text{GeV}))^2} \,, \qquad (1.19)$$

---

[1] The origin of the naming is the following. The first spin-1 particle which was known was the photon, the carrier of the electromagnetic force. The transverse polarisation of the photon refers to the fact that both the electric and magnetic field vectors are perpendicular to the flight direction of the photon. In analogy to the photon, also the transversely polarised W boson is the one with helicity -1 or $+1$.

with $s = E_{\mathrm{CM}}^2$ and α the fine-structure constant. Also many exotic processes occur at the rates similar to those of Standard Model processes.

The results of LEP were a success for the Standard Model. Figure 1.1 shows the results for some important parameters measured at LEP, using also results from SLC and $p\bar{p}$-colliders.

In the first LEP-phase, many parameters of the Z boson were measured to a high precision [18, 19]. The mass and the total width of the Z-boson was measured, and precise results of the partial decay widths to hadrons and leptons and the pole asymmetries were obtained. The results were used to obtain the number of light neutrino species: the ratio of the Z decay width into invisible particles over the leptonic decay width is determined to be $\Gamma_{\mathrm{inv}}/\Gamma_{\ell\ell} = 5.942 \pm 0.016$. From the Standard Model value for the ratio of the partial width to neutrinos and charged leptons, $\Gamma_{\nu\nu}/\Gamma_{\ell\ell} = 1.9912 \pm 0.0012$, the number of light neutrino species is obtained as the ratio of the above expressions: $N_\nu = 2.9841 \pm 0.0083$ [18], which is 0.5%, or two standard deviations, below the Standard Model value of 3.

In a second phase, the centre-of-mass energy of LEP was raised above the W-pair production threshold, and then further up to $\sqrt{s} = 209$ GeV. At these energies, precise measurements of the W properties were performed, along with studies using Z-pair events, and searches for the Higgs boson. Of particular interest at LEP II were the four-fermion processes $e^+e^- \rightarrow W^+W^- \rightarrow f_1\bar{f}_2f_3\bar{f}_4$ and $e^+e^- \rightarrow ZZ \rightarrow f_1\bar{f}_2f_3\bar{f}_4$. The latter ones have been used to determine the total cross-sections and the branching fractions for the Z-pair process. In this process, also neutral gauge couplings, *i.e.* couplings involving three or four neutral gauge bosons (Z or γ) have been studied. In addition, photon-pair production and fermion-pair production processes, $e^+e^- \rightarrow f\bar{f}$, have been studied, with $f\bar{f} = q\bar{q}, \mu^+\mu^-, \tau^+\tau^-$. For all these processes, the cross-sections have been found to be in agreement with the Standard Model Monte Carlo predictions, although the combined hadronic cross-sections are on average 1.7 standard deviations above the predictions. For further information and results see [18]. As an example, Figure 1.2 shows an overview of the cross-sections measured with the L3 detector.

Searches for the Standard Model Higgs boson have also been performed at LEP [20]. At LEP, the Higgs is expected to be produced mainly together with the Z boson through the Higgsstrahlung process $e^+e^- \rightarrow Z^* \rightarrow ZH$. The Higgs boson is then expected to decay mainly into $b\bar{b}$ quark pairs (with 74% branching ratio for a Higgs mass of 115 GeV), other possible decays include $\tau^+\tau^-$, W^+W^{-*}, gg (about 7% each), and $c\bar{c}$ (about 4%). Therefore the searches at the four LEP experiments are performed in the four-jet final state (H $\rightarrow$ b$\bar{b}$, Z $\rightarrow$ q$\bar{q}$), the missing energy final state (H $\rightarrow$ b$\bar{b}$, Z $\rightarrow$ $\nu\bar{\nu}$), the leptonic final state (H $\rightarrow$ b$\bar{b}$, Z $\rightarrow$ $\ell^+\ell^-$ with ℓ = e, μ), and the tau final states (H $\rightarrow$ b$\bar{b}$, Z $\rightarrow$ $\tau^+\tau^-$ and H $\rightarrow$ $\tau^+\tau^-$, Z $\rightarrow$ q$\bar{q}$). A test statistic is calculated for two scenarios, either background only or signal plus background, where a Higgs boson of test mass m_{H} is also contributing. The resulting confidence levels for the two scenarios are used to derive a lower bound on the mass of the Standard Model Higgs boson. The observed 95% confidence level lower limit on this mass as obtained by the combination of the four LEP experiments is 114.4 GeV.

Constraints on the Higgs mass can be found also using the measurements of Standard Model parameters. Several Standard Model fits can be performed with the measured

Summary 2004

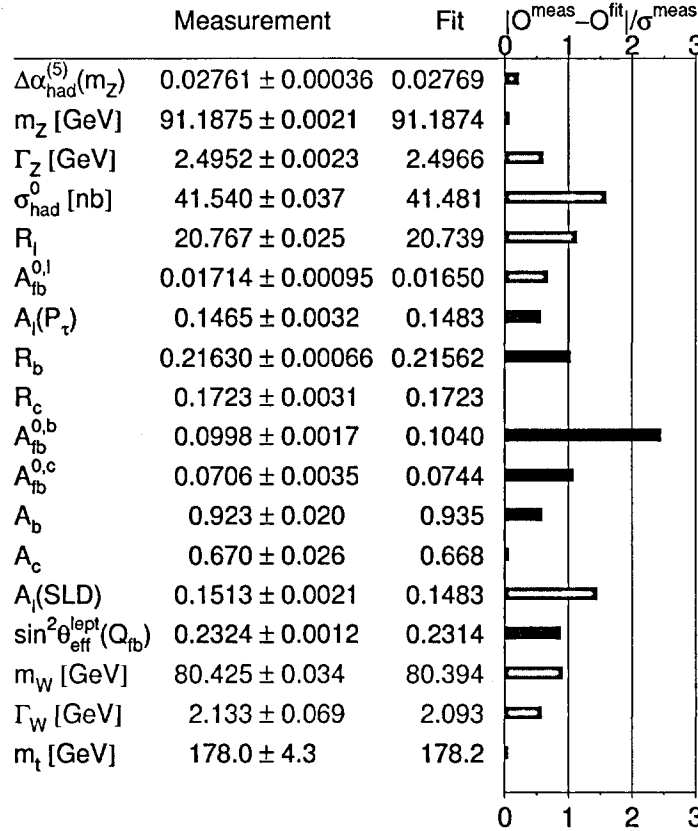|	Measurement	Fit	$\frac{|O^{meas}-O^{fit}|}{\sigma^{meas}}$
$\Delta\alpha_{had}^{(5)}(m_Z)$	0.02761 ± 0.00036	0.02769	
m_Z [GeV]	91.1875 ± 0.0021	91.1874	
Γ_Z [GeV]	2.4952 ± 0.0023	2.4966	
σ_{had}^0 [nb]	41.540 ± 0.037	41.481	
R_l	20.767 ± 0.025	20.739	
$A_{fb}^{0,l}$	0.01714 ± 0.00095	0.01650	
$A_l(P_\tau)$	0.1465 ± 0.0032	0.1483	
R_b	0.21630 ± 0.00066	0.21562	
R_c	0.1723 ± 0.0031	0.1723	
$A_{fb}^{0,b}$	0.0998 ± 0.0017	0.1040	
$A_{fb}^{0,c}$	0.0706 ± 0.0035	0.0744	
A_b	0.923 ± 0.020	0.935	
A_c	0.670 ± 0.026	0.668	
A_l(SLD)	0.1513 ± 0.0021	0.1483	
$\sin^2\theta_{eff}^{lept}(Q_{fb})$	0.2324 ± 0.0012	0.2314	
m_W [GeV]	80.425 ± 0.034	80.394	
Γ_W [GeV]	2.133 ± 0.069	2.093	
m_t [GeV]	178.0 ± 4.3	178.2	

0   1   2   3

Figure 1.1: A summary of Standard Model measurements obtained from LEP, SLC and $p\bar{p}$-colliders. For further explanations see [18].

parameters. As an example, Figure 1.3 shows the comparison of indirect measurements of the top-quark and the W boson mass compared to direct measurements and the Standard Model relationship for these masses as a function of the Higgs mass between 114 GeV and 1000 GeV. As one can see in that figure, the indirect and direct measurements are in good agreement, and both sets prefer a low value of the Higgs mass. The best constraints on the mass of the Higgs are obtained when all high Q^2 measurements are used in the fit. The resulting 95% confidence level upper limit on m_H is 260 GeV [18]. In future, the LHC experiments are expected either to find direct evidence for the Standard Model Higgs boson or to demonstrate physics beyond the Standard Model.

The LEP experiments have also performed searches for "exotic" new particles and other new phenomena, like Supersymmetry and extra dimensions. None of these searches however have found any signs of phenomena beyond the Standard Model at centre-of-mass energies up to 209 GeV [21, 22]. Again, the LHC experiments will enlarge the current sensitivity by about a factor of 10 for many phenomena.
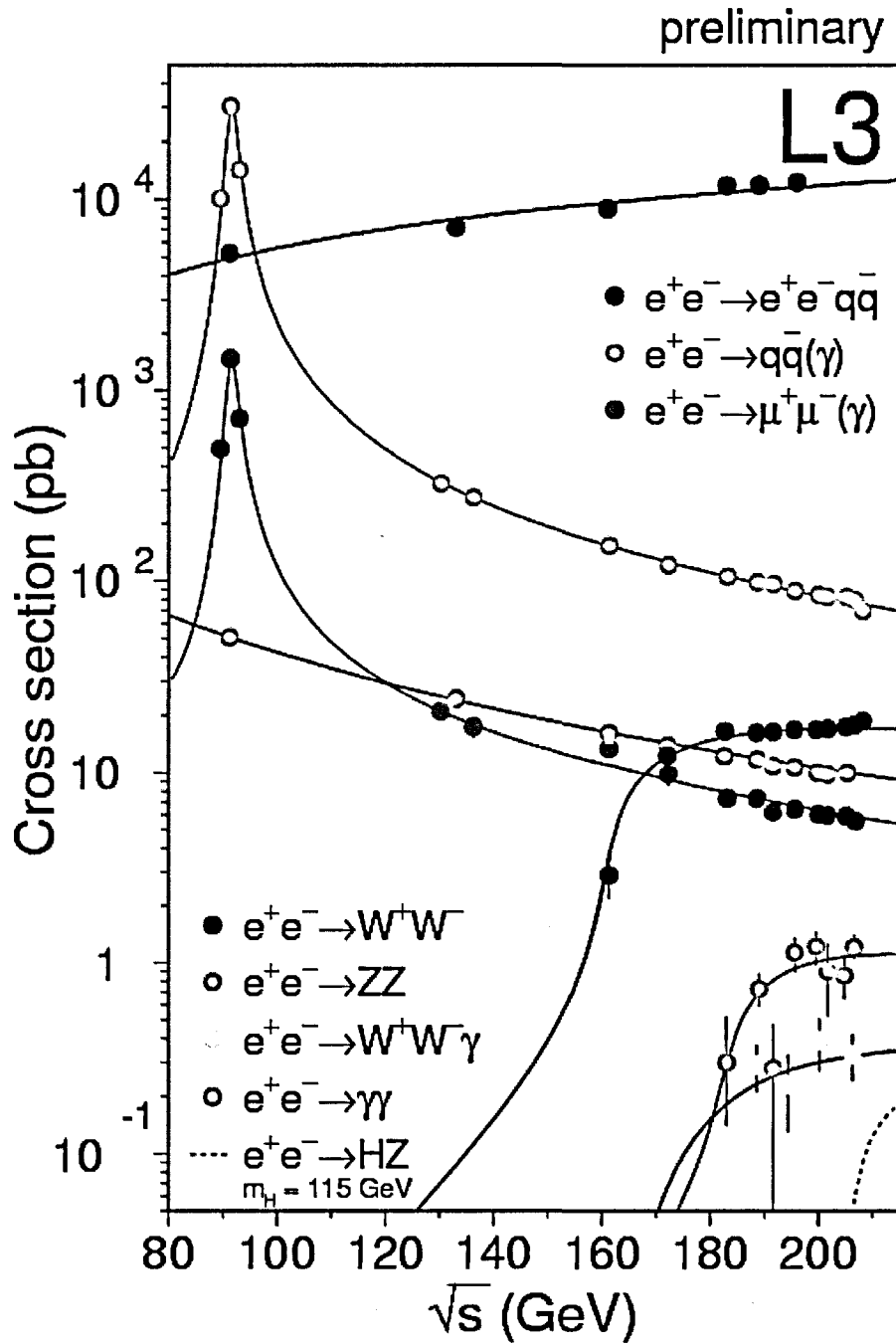
preliminary

L3

$e^+e^- \rightarrow e^+e^- q\bar{q}$

$e^+e^- \rightarrow q\bar{q}(\gamma)$

$e^+e^- \rightarrow \mu^+\mu^-(\gamma)$

$e^+e^- \rightarrow W^+W^-$

$e^+e^- \rightarrow ZZ$

$e^+e^- \rightarrow W^+W^-\gamma$

$e^+e^- \rightarrow \gamma\gamma$

$e^+e^- \rightarrow HZ$

m_H = 115 GeV

Cross section (pb)

$\sqrt{s}$ (GeV)

Figure 1.2: A summary of cross-section measurements performed using the L3 detector at LEP.
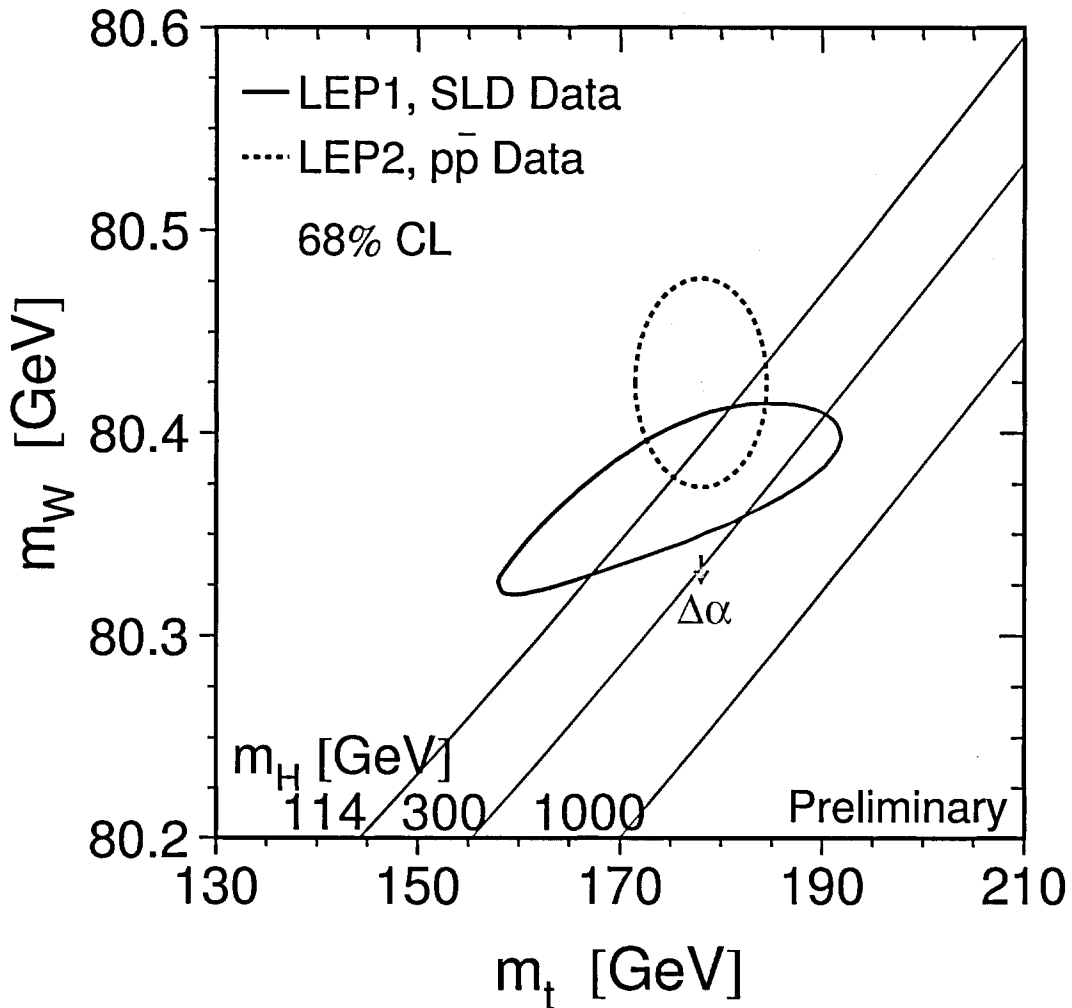
Figure 1.3: Measurements of the masses of the W boson and the top quark, m_W and m_t. Both the indirect measurements using LEPI and SLC data, and the direct measurements using LEP II and p$\bar{\text{p}}$-collider data are shown. The Standard Model relationship between those two masses is also indicated for various Higgs masses [18].

1.2.1 W Physics at LEP II

In the following, the most important results in W boson physics are summarised. Most of the measurements have been performed by all four LEP experiments and were combined.

W Boson Cross-Section and Decay Channels

The results of the total cross-section measurement for the process $e^+e^- \rightarrow W^+W^-$ show an overall agreement with the Standard Model predictions. Figure 1.4 shows the LEP combination for the measurement of the W-pair cross-section.

The W boson decays either leptonically, $W \rightarrow \ell\nu_\ell$, or hadronically into a quark-
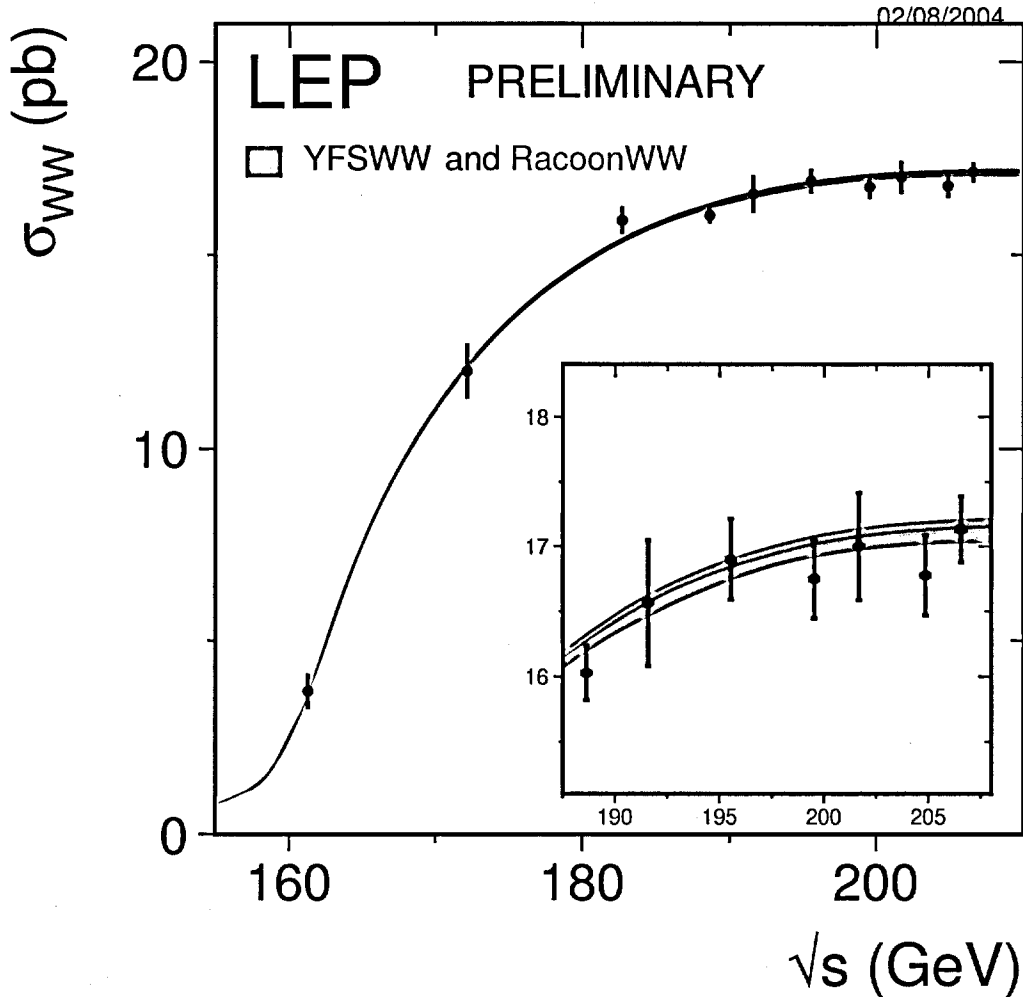
Figure 1.4: LEP combined measurement of the W-pair production cross-section, compared to the predictions of YFSWW and RacoonWW Monte Carlo. The shaded area represents the uncertainty on the Monte Carlo predictions [18].

antiquark pair, $W \rightarrow q_1 \bar{q}_2$. Thus W^- decays into $e^- \bar{\nu}_e, \mu^- \bar{\nu}_\mu, \tau^- \bar{\nu}_\tau, \bar{u}d'$, and $\bar{c}s'$, where d' and s' are the Cabibbo-rotated states of the d and s quarks. The decay channels are expected by the Standard Model to have the same branching ratio, taking into account that three colour states exist for quarks. Thus the W branching ratios within the Standard Model for the channels listed above are 1:1:1:3:3. QCD processes however cause a small correction of these ratios [23]. The universal part of the QCD corrections for massless quarks is expressed by the factor C:

$$C = 1 + \frac{\alpha_s}{\pi} + 1.409 \, \frac{\alpha_s^2}{\pi^2} - 12.77 \, \frac{\alpha_s^3}{\pi^3} \, . \tag{1.20}$$

		Lepton non-universality	Lepton universality	Standard Model
BR(W → e⁻ν̄ₑ)	[%]	10.66 ± 0.17		
BR(W → μ⁻ν̄_μ)	[%]	10.60 ± 0.15	10.84 ± 0.09	10.83
BR(W → τ⁻ν̄_τ)	[%]	11.41 ± 0.22		
BR(W → hadrons)	[%]		67.49 ± 0.28	67.51

Table 1.2: Summary of the combined LEP results for the W branching fractions derived from W-pair production cross-section measurements up to $\sqrt{s} = 209$ GeV. Two fits are performed: one without an assumption of lepton-universality, and one flavour blind, *i.e.* assuming lepton-universality. The error reflects both statistical error and systematics. [18]

Thus the partial decay width of W → f₁f₂ is

$$\Gamma(W \to \ell\nu_\ell) = \frac{G_F M_W^3}{6\sqrt{2}\pi} \quad \text{and} \quad \Gamma(W \to q_i\bar{q}_j) = \frac{C \cdot 3 \cdot G_F M_W^3}{6\sqrt{2}\pi} |V_{ij}|^2 , \tag{1.21}$$

and the branching ratio is

$$BR(W \to q_i\bar{q}_j) = 3C |V_{ij}|^2 BR(W \to \ell\nu_\ell), \tag{1.22}$$

where V_{ij} is the CKM matrix element. This QCD correction enlarges the branching ratio of the hadronic final states from 66.6% to 67.5%.

The branching ratios have been measured accurately at LEP. Table 1.2 shows the combined results from all LEP experiments. Two fits are performed: one without assumption of lepton-universality, to check the agreement of the branching ratios in the particular leptonic decay modes, and one flavour blind. The LEP combined numbers show good agreement between the leptonic decay channels and with the Standard Model prediction. It has to be mentioned that the result of the measurement of the branching ratio for the tau channel is somewhat higher than for the electron and muon channel. A simple explanation would be that, in addition to statistical fluctuations, the effects of electron and muon misidentification are slightly underestimated. In the following, we use only the Standard Model branching ratios.

W Boson Mass and Width

Using the W-pair events recorded at all four LEP experiments, the W mass and width was determined to a great precision. The LEP combined numbers are [18]:

$$m_W = 80.412 \pm 0.042 \text{ GeV} \tag{1.23}$$

$$\Gamma_W = 2.150 \pm 0.091 \text{ GeV} \tag{1.24}$$

Gauge Boson Couplings

One of the main goals of the measurements at LEP is the determination of the gauge boson couplings and possible anomalous contributions due to new physics. The charged triple gauge boson couplings of interest in W-physics are the ZWW and γWW vertices. The parametrisation of these vertices is described in detail in reference [24]. The most general Lorentz-invariant Lagrangian has fourteen independent complex couplings, seven for each of the vertices. Using the assumption of gauge invariance as well as C and P conservation, the number of independent triple gauge couplings can be reduced to five. These couplings are considered as real, with the imaginary parts fixed to zero.

Using all these assumptions, the five parameters are measured by the four LEP experiments. The existence of triple gauge boson couplings among the electroweak gauge bosons is experimentally verified. To date, no significant deviation from the Standard Model couplings has been found and the data were used to set confidence limits for the parameters. For a detailed discussion of the triple gauge couplings see [18, 24, 25], where also the latest limits on the anomalous TGC parameters are given.

The Spin Density Matrix (SDM) measurement has proven to be a possible way of searching for CP- and CPT-violating triple gauge couplings. The method itself follows References [26, 27, 28]. The SDM measurement allows also the determination of the inclusive fractions of W helicity states. The latest results are summarised in [29, 30, 31]. No significant deviation from the Standard Model prediction has been found.

Chapter 2

The $e^+e^- \to W^+W^-$ Process

In this chapter, the W-pair production and decay is described, with emphasis on the polarisation properties of W bosons.

The process $e^+e^- \to W^+W^- \to f_1\bar{f}_2f_3\bar{f}_4$ proceeds to lowest order via the Feynman graphs shown in Figure 2.1. These graphs are usually referred to as CC03 diagrams[1]. Other diagrams contributing to the same final states can involve only one or no W bosons at all. A complete classification of these four fermion processes can be found in [32]. The complete set of diagrams is usually denoted by CC56. For example, for final states with electrons or electron-neutrinos, the additional diagrams which have to be taken into account are denoted by CC20.

2.1 Definitions

In the following, the coordinate system and the angles in the $e^+e^- \to W^+W^-$ process used for the measurements presented in this thesis are described.

The origin of the laboratory coordinate system lies in the interaction point of the L3 detector, *i.e.* the geometrical point where the electron and the positron collide. This point can slightly differ from the geometrical centre of the detector and is determined for each measurement period from the data. It is worthwhile mentioning that the laboratory frame is also the centre-of-mass frame of the e^+e^- system. In this coordinate system, the z-axis is along the beam pipe, pointing into the flight direction of the electron. The x-axis points towards the centre of the LEP ring, and the y-axis points vertically upwards. In the corresponding polar coordinate system the coordinates used are r, the polar angle Θ, describing the angle between the z-axis and $\vec{r}$, and the azimuthal angle ϕ.

The axis y', which is used in the analysis is defined as the cross-product of the z axis (normalised e^- momentum vector) and the normalised W^- momentum vector, $\vec{y}' = \hat{z} \times \hat{p}_{W^-} = \hat{p}_{e^-} \times \hat{p}_{W^-}$. Figure 2.2 shows the angles used in this thesis:

- Θ_{W^-} is the W^- scattering angle, *i.e.* the angle between the e^- and the W^- momentum vectors in the laboratory frame; the helicity composition depends strongly

---

[1]CC stands for Charged Current, because the production of the four-fermion final state proceeds via weak charged current W^+ and W^-.
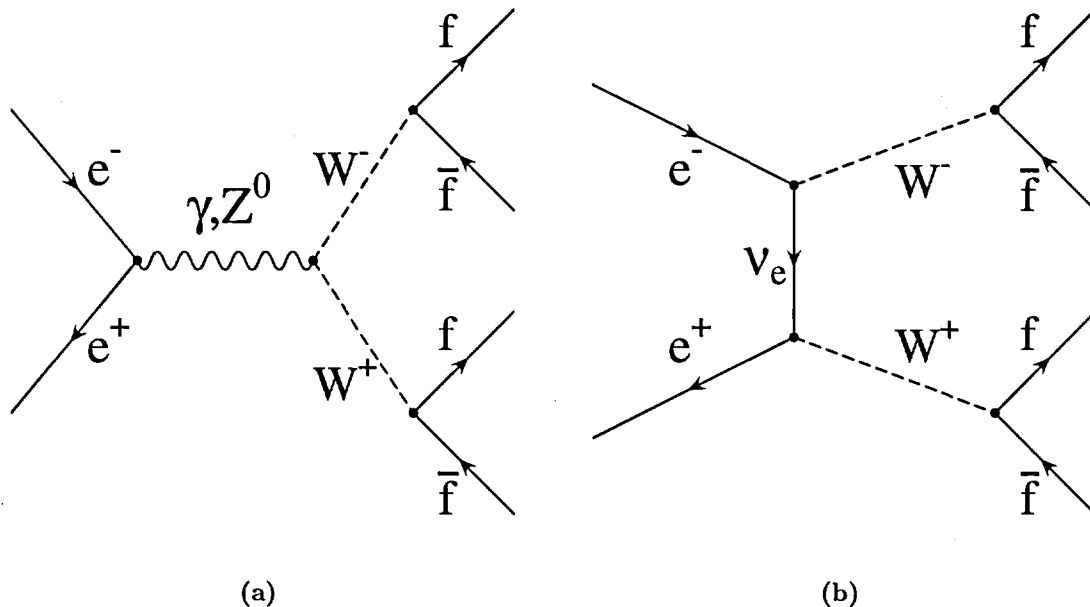
15

Figure 2.1: Tree level diagrams for the process $e^+e^- \to W^+W^- \to f_1\bar{f}_2f_3\bar{f}_4$: (a) s-channel ($\gamma$, Z exchange) and (b) t-channel (ν exchange) graphs.

on this angle and is also part of the presented measurement,

- θ_ℓ^* (θ_q^*) is the polar decay angle of the charged lepton (down-type quark d, s or b) in the centre-of-mass frame of the leptonically (hadronically) decaying W boson; these are the angles used for the measurement of the helicity, as each helicity shows a characteristic distribution in these angles,

- ϕ_ℓ (ϕ_q) is the azimuthal decay angle of the charged lepton (the down-type quark) with respect to the y' axis; this angle is invariant w.r.t. boosts along the W flight direction and thus the same in the laboratory frame and the centre-of-mass frame of the W boson, and is used in the measurement of the decay plane orientation.

2.2 W-Pair Production and Decay

In this section, the on-shell WW production and decay within the Standard Model are described using the approximation of massless fermions, following the paper by Hagiwara *et al.* [33] and the LEP Yellow Report on Physics at LEP2 [24].

The contributions of the s-channel and the t-channel processes (see Figure 2.1) to the helicity amplitudes are:

$$\mathcal{M}(\sigma, \lambda, \bar{\lambda}) = \mathcal{M} = \mathcal{M}_\gamma + \mathcal{M}_Z + \mathcal{M}_\nu , \tag{2.1}$$

with σ ($\bar{\sigma}$) denoting the helicity of the incoming electron (positron), $\sigma = +1$ or -1, and λ ($\bar{\lambda}$) the helicity of the W$^-$ (W$^+$), $\lambda = +1, 0$ or -1.

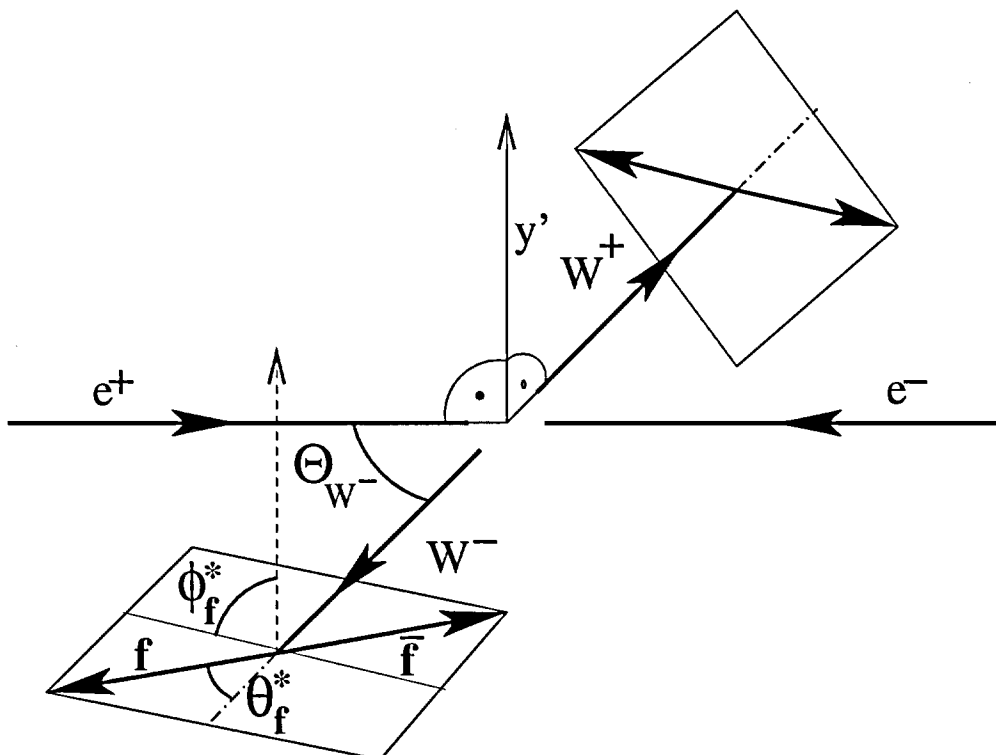**Figure 2.2:** Definition of angles in the $e^+e^-\to W^+W^-\to f_1\bar{f}_2 f_3\bar{f}_4$ reaction.

The helicity amplitudes can be written with extracting some factors and the leading angular dependence in terms of the d-functions [23], d^{J_0}, where $J_0 = 1, 2$ denotes the lowest angular momentum contributing to a given helicity combination:

$$\mathcal{M}_{\sigma,\bar{\sigma},\lambda,\bar{\lambda}}(\Theta_{W^-}) = \sqrt{2}\, e^2\; \tilde{\mathcal{M}}_{\sigma,\bar{\sigma},\lambda,\bar{\lambda}}(\Theta_{W^-})\; \epsilon\; d^{J_0}_{\Delta\sigma,\Delta\lambda}(\Theta_{W^-})\,, \tag{2.2}$$

where $\epsilon = \Delta\sigma\,(-1)^\lambda$ is a sign factor, $\Delta\sigma = \frac{1}{2}(\sigma-\bar{\sigma})$, $\Delta\lambda = \lambda-\bar{\lambda}$, and $J_0 = \max(|\Delta\sigma|, |\Delta\lambda|)$. Table 2.1 provides a list of the relevant d-functions.

The reduced amplitude $\tilde{\mathcal{M}}$ is not a partial wave amplitude as it can still have a Θ_{W^-} dependence. Rather, J_0 is the minimum angular momentum of the system and the amplitude includes partial waves of $J = J_0, J_0 + 1, \ldots$.

The s-channel Feynman diagrams have only $J = 1$ partial wave because of angular momentum conservation. The t-channel ν-exchange diagram has all partial waves with $J \geq J_0$. We consider the cases for $J_0 = 1$ and $J_0 = 2$ separately[2]. In the case that $J_0 = 2$, only the t-channel ν-exchange diagram contributes to this final state. The final W bosons are both transverse, $(\lambda, \bar{\lambda}) = (+1, -1)$ or $(-1, +1)$. Hence the reduced amplitude has the form:

$$\tilde{\mathcal{M}} = -\frac{\sqrt{2}}{\sin^2\theta_W}\frac{1}{1 + \beta^2 - 2\beta\ \cos\Theta_{W^-}}\ \delta_{\Delta\sigma,-1}\,. \tag{2.3}$$

---

[2]Conservation of electron chirality excludes the case $J_0 = 0$ in the approximation of massless electrons, because $\Delta\sigma$ is either 1 or -1.

$$
\begin{array}{rcl}
d^2_{1,2} = -d^2_{-1,-2} &=& \tfrac{1}{2}(1 + \cos\Theta_{W^-})\sin\Theta_{W^-} \\
d^2_{1,-2} = -d^2_{-1,2} &=& -\tfrac{1}{2}(1 - \cos\Theta_{W^-})\sin\Theta_{W^-} \\
d^1_{1,1} = d^1_{-1,-1} &=& \tfrac{1}{2}(1 + \cos\Theta_{W^-}) \\
d^1_{1,-1} = d^1_{-1,1} &=& \tfrac{1}{2}(1 - \cos\Theta_{W^-}) \\
d^1_{1,0} = -d^1_{-1,0} &=& -\sqrt{\tfrac{1}{2}}\sin\Theta_{W^-}
\end{array}
$$

Table 2.1: The d-functions used for the calculation of the helicity amplitudes.

$\Delta\lambda$	$(\lambda\bar{\lambda})$	$A^{\gamma,Z}_{\lambda\bar{\lambda}}$	$B_{\lambda\bar{\lambda}}$	$C_{\lambda\bar{\lambda}}$
1	$(+1,0), (0,-1)$	2γ	2γ	$2(1+\beta)/\gamma$
-1	$(0,+1), (-1,0)$	2γ	2γ	$2(1-\beta)/\gamma$
0	$(+1,+1), (-1,-1)$	1	1	$1/\gamma^2$
0	(00)	$2\gamma^2+1$	$2\gamma^2$	$2/\gamma^2$

Table 2.2: The coefficients $A^\gamma_{\lambda\bar{\lambda}} = A^Z_{\lambda\bar{\lambda}}$, $B_{\lambda\bar{\lambda}}$ and $C_{\lambda\bar{\lambda}}$ for the Standard Model ($\beta = \sqrt{(1 - 4m_W^2/s)}$ and $\gamma = \sqrt{s}/2m_W$).

For $J_0 = 1$ we obtain the other seven final helicity combinations, five of them having at least one longitudinal W boson. The reduced amplitudes for $J_0 = 1$ are:

$$
\tilde{\mathcal{M}}_\gamma = -\beta \, \delta_{|\Delta\sigma|,1} \, A^\gamma_{\lambda\bar{\lambda}}, \tag{2.4}
$$

$$
\tilde{\mathcal{M}}_Z = \beta \, A^Z_{\lambda\bar{\lambda}} \left[\delta_{|\Delta\sigma|,1} - \delta_{\Delta\sigma,-1}\frac{1}{2\sin^2\theta_W} \right] \frac{s}{s - m_Z^2}, \tag{2.5}
$$

$$
\tilde{\mathcal{M}}_\nu = \delta_{\Delta\sigma,-1} \, \frac{1}{2\beta \, \sin^2\theta_W} \left[B_{\lambda\bar{\lambda}} - \frac{1}{1 + \beta^2 - 2\beta \, \cos\Theta_{W^-}}C_{\lambda\bar{\lambda}} \right], \tag{2.6}
$$

where $\sqrt{s}$ is the e^+e^- centre-of-mass energy and $\beta = \sqrt{1 - 4m_W^2/s}$ the $W^\pm$ velocity. The coefficients $A^\gamma_{\lambda\bar{\lambda}} = A^Z_{\lambda\bar{\lambda}}$, $B_{\lambda\bar{\lambda}}$ and $C_{\lambda\bar{\lambda}}$ for the Standard Model are given in Table 2.2.

Considering the decay of the W bosons into (massless) fermions, the polarisation-summed squared matrix elements are:

$$
\sum |\mathcal{M}_{\text{all}}|^2 = \sum_{\sigma,\bar{\sigma},\sigma_i} \left| \mathcal{M}_{\text{all}}(k,\sigma;\bar{k},\bar{\sigma};p_i,\sigma_i) \right|^2 =
$$

$$
= e^4 \left| g_-^{Wf_1f_2} g_-^{Wf_3f_4} \right|^2 C^2\bar{C}^2 \; q^2\bar{q}^2 \; \left| D_W(q^2)D_W(\bar{q}^2) \right|^2 \; \mathcal{P}^{\lambda,\bar{\lambda}}_{\lambda',\bar{\lambda}'} \, \mathcal{D}^\lambda_{\lambda'} \, \bar{\mathcal{D}}^{\bar{\lambda}}_{\bar{\lambda}'}, \tag{2.7}
$$

where $\sigma_i (i = 1, \ldots 4)$ are the spins of the decay fermions, $g_-^{Wf_1f_2}$ the standard V-A coupling $\frac{V_{ij}}{\sqrt{2}\sin\theta_W}$ with V_{ij} the Cabibbo-Kobayashi-Maskawa matrix elements for three generations, and C the effective colour factor which is 1 for leptons and $\sqrt{3}$ for quarks. This equation gives the general structure of the matrix for the process $e^+e^- \to W^+W^- \to f_1\bar{f}_2f_3\bar{f}_4$ with pure V-A couplings of the W bosons to massless fermions. The production tensor (spin

density matrix) is expressed in terms of the production amplitudes:

$$\mathcal{P}^{\lambda,\bar\lambda}_{\lambda',\bar\lambda'} = \sum_{\sigma,\bar\sigma} \mathcal{M}_{\sigma,\bar\sigma,\lambda,\bar\lambda}(\Theta_{W-})\, \mathcal{M}^*_{\sigma,\bar\sigma,\lambda',\bar\lambda'}(\Theta_{W-})\,, \tag{2.8}$$

with the production amplitudes given by Equation 2.2. The decay tensors are:

$$\mathcal{D}^{\lambda}_{\lambda'} = l_\lambda l^*_{\lambda'}\,, \quad \bar{\mathcal{D}}^{\bar\lambda}_{\bar\lambda'} = \bar{l}_{\bar\lambda} \bar{l}^*_{\bar\lambda'} \tag{2.9}$$

with

$$\begin{aligned}
(l_-, l_0, l_+) &= \left(\frac{1}{\sqrt{2}}(1+\cos\theta^*)e^{-i\phi},\, -\sin\theta^*,\, \frac{1}{\sqrt{2}}(1-\cos\theta^*)e^{i\phi}\right)\,, \\
(\bar{l}_-, \bar{l}_0, \bar{l}_+) &= \left(\frac{1}{\sqrt{2}}(1+\cos\bar\theta^*)e^{i\bar\phi},\, -\sin\bar\theta^*,\, \frac{1}{\sqrt{2}}(1-\cos\bar\theta^*)e^{-i\bar\phi}\right)\,.
\end{aligned} \tag{2.10}$$

The differential cross-section is obtained by integrating over the virtual W mass squared, q^2 and $\bar{q}^2$:

$$\frac{\mathrm{d}\sigma}{\mathrm{d}\cos\Theta_{W-}\ \mathrm{d}\theta^*\mathrm{d}\phi\ \mathrm{d}\bar\theta^*\mathrm{d}\bar\phi} = \frac{9\beta}{8192\pi^3 s}\mathrm{BR}(\mathrm{W}\to \mathrm{f}_1\bar{\mathrm{f}}_2)\,\mathrm{BR}(\mathrm{W}\to \mathrm{f}_1\bar{\mathrm{f}}_2)\mathcal{P}^{\lambda,\bar\lambda}_{\lambda',\bar\lambda'}\mathcal{D}^{\lambda}_{\lambda'}\bar{\mathcal{D}}^{\bar\lambda}_{\bar\lambda'}\,. \tag{2.11}$$

The differential cross-section for the process $\mathrm{e^+e^-}\to \mathrm{W^+W^-}$ follows after integrating over all the decay fermion angles:

$$\frac{\mathrm{d}\sigma}{\mathrm{d}\cos\Theta_{W-}} = \frac{\beta}{128\pi s}\mathcal{P}^{\lambda,\bar\lambda}_{\lambda',\bar\lambda'}\,. \tag{2.12}$$

Symmetry Properties

Some general symmetry properties apply to the full amplitudes of Equation 2.2. CPT-invariance leads to the equation:

$$\tilde{\mathcal{M}}_{\sigma,\bar\sigma,\lambda,\bar\lambda} = \tilde{\mathcal{M}}^*_{-\bar\sigma,-\sigma,-\bar\lambda,-\lambda}\,, \tag{2.13}$$

while CP-invariance leads to:

$$\tilde{\mathcal{M}}_{\sigma,\bar\sigma,\lambda,\bar\lambda} = \tilde{\mathcal{M}}_{-\bar\sigma,-\sigma,-\bar\lambda,-\lambda}\,. \tag{2.14}$$

These two relations connect the same initial state for non-vanishing amplitudes:

$$(\sigma,\bar\sigma) = (\pm 1, \mp 1) = (-\bar\sigma, -\sigma) \tag{2.15}$$

For the final state, they relate states with the same $\Delta\lambda$:

$$\begin{aligned}
\Delta\lambda = \quad +1: \quad & (\lambda,\bar\lambda) = \quad (+1,0) \leftrightarrow (0,-1)\,, \\
0: \quad & (+1,+1) \leftrightarrow (-1,-1)\,, \\
-1: \quad & (0,+1) \leftrightarrow (-1,0)\,.
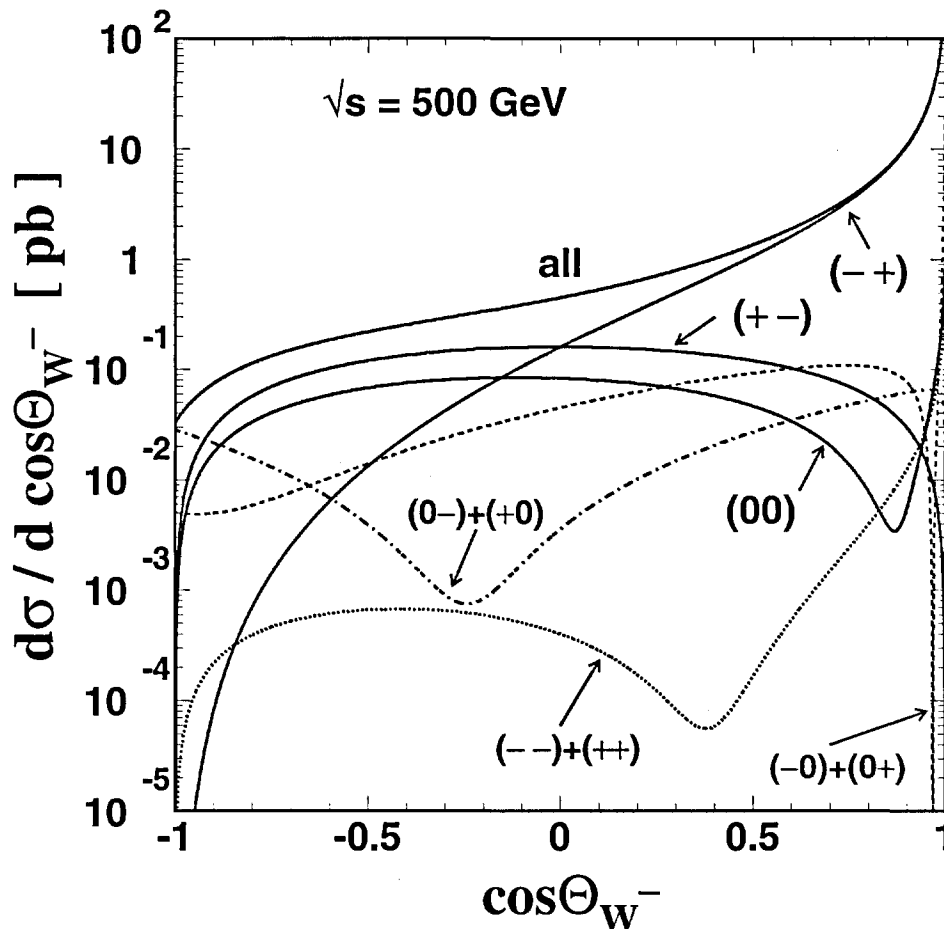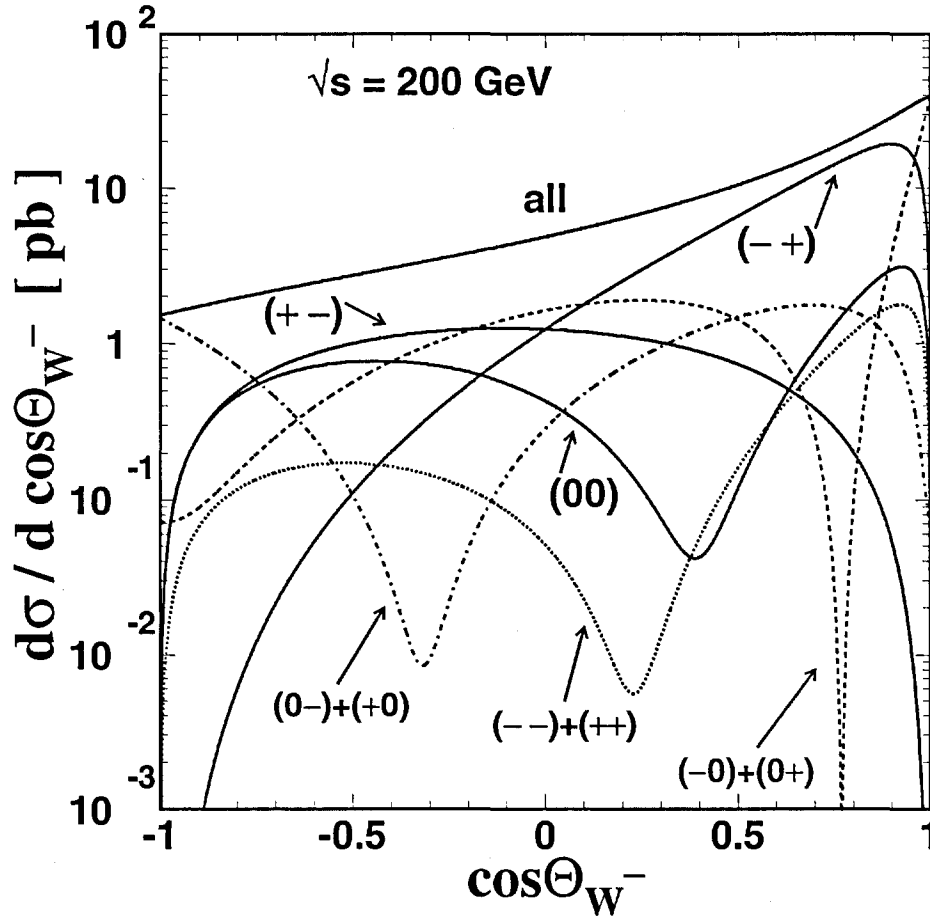\end{aligned} \tag{2.16}$$

Figure 2.3: Differential cross section for pair production of polarised W bosons at $\sqrt{s} = 500$ GeV, averaged over initial electron polarisations. The W^- and W^+ helicities $(-, +, 0)$ in the laboratory frame are given in parentheses.

2.3 Leading Order Analytical Calculation

In order to demonstrate the most important properties of the $e^+e^- \to W^+W^-$ process at different energies, the formulae introduced in Section 2.2 have been used to generate distributions at different centre-of-mass energies[3].

To calculate the differential cross-section for the particular helicity combinations, Equation 2.12 is used. First the helicity amplitudes are calculated, using Equations 2.2 and 2.3, 2.4, 2.5 and 2.6. The production amplitudes are calculated using Equation 2.8, summing over initial electron helicities. According to the symmetry properties listed in Equation 2.16, the corresponding contributions are summed.

A longitudinal state can lead to a "bad" high-energy behaviour, *i.e.* to a possible breakdown of unitarity. The longitudinal polarisation vectors contain a factor $\gamma = \sqrt{s}/m_W$ which causes this behaviour. In the formulae discussed in the previous section this be-

---

[3]The calculations have been done using a routine which I developed for this analysis.

Figure 2.4: Differential cross section for pair production of polarised W bosons at $\sqrt{s} = 200$ GeV, averaged over initial electron polarisations. The W^- and W^+ helicities $(-, +, 0)$ in the laboratory frame are given in parentheses.

comes obvious when looking at the A and B coefficients which are used in the calculation of the reduced helicity amplitudes for $J_0 = 1$ (see Equation 2.6). $J_0 = 2$ states, $(-1, +1)$ and $(+1, -1)$, do not involve longitudinal states and their high-energy behaviour is safe. At high energies, without cancellations between different terms, the amplitudes would diverge.

In the Standard Model, the terms from the particular contributions cancel however, and thus reduce the power of γ by 2. This is observed in Figure 2.3, which shows the total differential cross-section and the differential cross-sections for the different helicity combinations[4], $(\lambda, \bar{\lambda})$, as a function of $\cos \Theta_{W^-}$ for $\sqrt{s} = 500$ GeV. It demonstrates that at a relatively high energy (within reach of a possible future linear e^+e^- collider) basically only three terms survive: the t-channel $(-1, +1)$ and $(+1, -1)$ and the s-channel (00) contributions.

Figure 2.4 shows that the same tendencies already appear at $\sqrt{s} = 200$ GeV, *i.e.* at

---

[4] Here and in similar plots, the W helicities are denoted by $-, +, 0$, which is short for $-1, +1, 0$.

energies relatively close to the WW production threshold. At these energies, the fraction of longitudinally polarised W bosons is around 0.25.

Thus it can be said that the self-coupling of gauge bosons ensures that the sum of the three diagrams from Figure 2.1 is finite, even though the individual diagrams diverge. However, if the structure of the ZWW and γWW triple gauge couplings were anomalous, this cancellation, and thus the behaviour, is modified.

Another very important example of cancellations through self-couplings is the WW scattering process, $W^+W^- \to W^+W^-$. The Feynman diagrams for this process consist of an s-channel γ/Z process, a t-channel γ/Z exchange and a four-W-boson vertex. To ensure the renormalisability, the s-channel and t-channel Higgs boson exchange has to be introduced. Without the Higgs scalar, the sum of the Feynman diagrams would diverge as s/m_W^2.

Using the methods presented in this thesis, the behaviour of the helicity fractions presented above could be well tested at a future high-luminosity linear collider. In contrast to a hadron collider, the whole event can be well measured at a lepton linear collider, and all the angles can be determined in the same way as presented in this thesis. As a next step, the analysis methods presented in the following should be used at such a collider to obtain results with a much larger event sample and thus yielding a large improvement in the significance.

Chapter 3

Experimental Apparatus

3.1 The Large Electron Positron Collider (LEP)

The Large Electron Positron Collider [34] was built at CERN to study electron-positron collisions at centre-of-mass energies from around 90 GeV to above 200 GeV and especially the Standard Model physics of the W and Z bosons.

In a first phase, LEP ran at and around the Z-resonance (1989–1995), then – in a second phase called LEP II, starting at the end of 1995 – at higher energies. From 1995 onwards the centre-of-mass energy was increased in steps from 130 GeV to 209 GeV. In November 2000, the LEP collider and the experiments were terminated and dismantled to make space for the Large Hadron Collider.

LEP was situated in a tunnel of 26.66 km circumference at the border between France and Switzerland (Figure 3.1). The large circumference is a compromise between two opposite requirements. On one hand costs, feasibility of the construction and geographical possibilities make it desirable to keep the radius as small as possible. On the other hand by enlarging the bending radius, the loss of energy due to synchrotron radiation is reduced and thus higher beam energies can be reached with the same accelerating power.

The collider consisted of eight bending sections of 2.8 km each and eight straight sections, four of which housed the experiments ALEPH, DELPHI, L3 and OPAL. The electrons and positrons were accelerated on the straight sections, from an injection energy of 22 GeV to the final energy. The injection system consisted of the accelerators PS and SPS, together with the linear accelerator LIL (LEP Injector Linac) and an accumulation ring to enhance positron intensity (Figure 3.2).

In its final state, the RF system of LEP II contained 288 super-conducting cavities (cooled with helium at 4.5 K) that were supplied by 36 klystrons plus the required waveguides, and 56 copper cavities, supplied by 8 klystrons plus the required waveguides [35]. LEP II was operating mostly in a mode with four bunches of electrons and four bunches of positrons (4×4 mode).

Generally, the achievable beam energy in a storage ring is determined by the following factors:

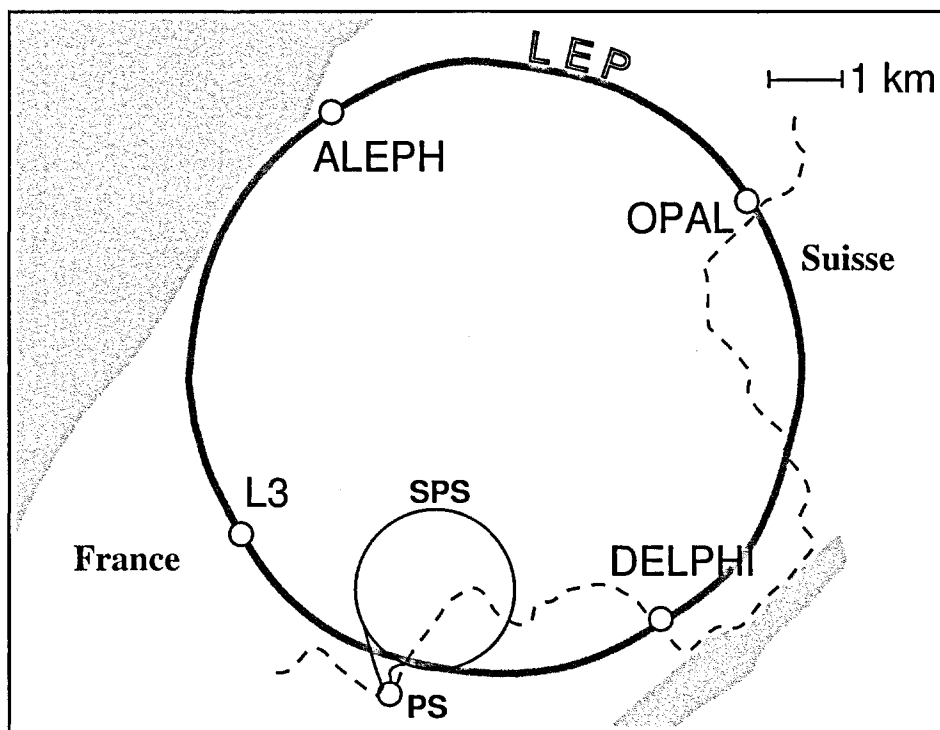- The accelerating field which is needed to accelerate the particles to their final energy

23

Figure 3.1: The LEP accelerator and the location of the four experiments.

and compensating for losses due to synchrotron radiation in the bending sections. The mean energy loss of electrons in a circular orbit per revolution due to synchrotron radiation is

$$W_r = 8.85 \cdot 10^{-5} \frac{\text{GeV}^{-3}}{\text{m}} \cdot \frac{E^4}{r} \, ,$$

(3.1)

and thus scales with the fourth power of the beam energy. At LEP, this was the limiting factor for the maximum achievable energy. At the highest reached beam energy of 104.45 GeV the loss due to synchrotron radiation amounted to about 3.3 GeV per revolution. Additionally, the accelerating field was needed for longitudinal beam stability (for 104 GeV beam energy, about 14% over-voltage was required).

- The achievable field strength of the magnetic elements needed for guiding the beam in the bending sections. The required field scales linearly with the beam energy. At LEP, the field was well below the achievable limits.

- The dynamical behaviour of the stored particle beams is limited by factors like dynamic aperture, transverse beam size and so on.

The operation scheme in the last years was tuned in order to obtain centre-of-mass energies as high as possible. During the year 2000, the accelerating gradient of the superconducting cavities was set to 7.5 MV/m which was far above the design value of 6 MV/m. The available RF voltage in LEP was significantly higher than the nominal voltage in the
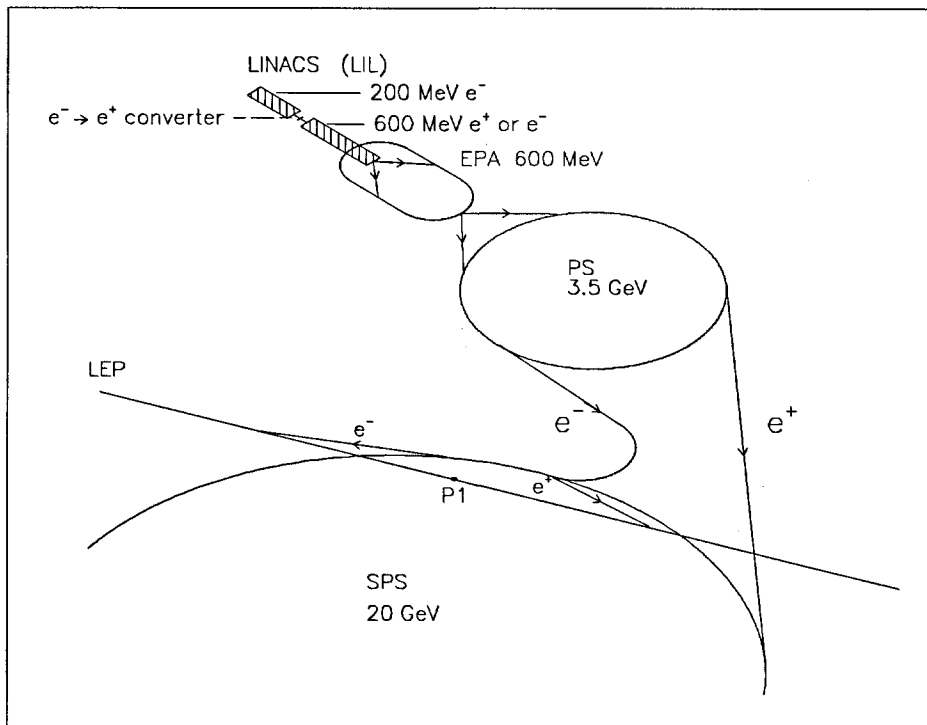
Figure 3.2: The LEP accelerator injection system.

years before. The high energies however resulted also in a lower luminosity and larger background.

To achieve a good efficiency of LEP, the effective beam energy was always set below the maximum possible energy. This safety margin was needed to provide an overhead for the case of klystron trips in the RF-system. Typically, the beam energy was kept 0.8 GeV (1 klystron trip) or 1.6 GeV (2 klystrons trip) below the maximum energy. As a compromise between an energy as high as possible and a sufficiently stable beam a mini-ramp procedure was used. A physics fill was established at a lower energy (2 klystrons margin), then ramped in collision, while the experiments were taking data, to a medium energy (1 klystron margin) and ended with maximum energy (no margin). The maximum reached beam energy using this approach was 104.45 GeV.

The luminosity at a circular collider is expressed generally as:

$$\mathcal{L} = \frac{N_1 N_2}{A} fn \ ,$$ (3.2)

with N_1, N_2 the number of particles, f the revolution frequency of the beams (at LEP $\approx$ 11.3kHz), n the number of circulating bunches, and $A = 4\pi\sigma_x\sigma_y$ the cross-sectional area of the beam. In terms of the beam current $I_i = N_i efn$, the luminosity formula reads:

$$\mathcal{L} = \frac{I_1 I_2}{4\pi\sigma_x\sigma_y e^2 fn} \ .$$ (3.3)

Typical values for LEP II were $2000 - 2500\mu$A for I, 150 μm for σ_x and 5 μm for σ_y.

To achieve a high luminosity, it is therefore important to maximise the currents and to minimise the size of the beams in the interaction points. Several factors however caused a reduction of instantaneous luminosity at highest energies during the year 2000 run [35].

Figure 3.3 shows the integrated luminosities delivered to the experiments during the LEP operation. Each line represents one year of operation. The last three years of LEP II were the most productive in terms of luminosity with integrated luminosities above 200pb^{-1} per year. During the last year of LEP II (2000) the trade-off between luminosity and beam-energy is visible. After a final effort to reach the highest possible energies, the LEP collider was shut down at the end of the year. Figure 3.4 shows the historic last luminosity diagram from 2nd November 2000.

3.2   The L3 Detector

The L3 detector (Figure 3.5) was one of the four omni-purpose detectors at LEP [19, 36]. All subdetectors were installed within a 7800 ton magnet with an inner radius of 5.93 m and a length of 11.90 m, providing a 0.5 Tesla field. The inner part of the detector was placed within a 32m long, 4.45m diameter steel tube which was concentric with the LEP beam line, as shown in Figure 3.6. The muon chambers were mounted in three layers on the outside of this support tube, as shown in Figure 3.7. The tube contained the inner subdetector barrel and endcap elements.

The barrel elements were from inside to outside: the beam pipe, the Silicon Microvertex Detector (SMD), the Time Expansion Chamber (TEC), the electromagnetic calorimeter (made of BGO crystals), the hadron calorimeter (made of depleted uranium) and the muon chambers. The endcap elements were from inside to outside an electromagnetic calorimeter, a hadron calorimeter and the forward muon chambers. The BGO luminosity monitors were mounted at small angles around the beampipe.

3.2.1   The Tracking System

Silicon Microvertex Detector (SMD)

The silicon microvertex detector [37] was built in 1994 as the innermost tracking device. It consisted of two cylindrical layers of 12 microstrip ladders, each of them divided into two wafers. They were mounted between the radii of 5.5 cm to 8.0 cm. The polar angle coverage was 22° to 158°.

The single point resolution is intrinsically 7 μm for the R-ϕ measurement and 14 μm for the z-coordinate measurement [38]. The alignment was made using Bhabha and dimuon events. The error on the distance of closest approach to the vertex (DCA) is between 25 and 40 μm, depending on the pattern of SMD hits which are included in the fit.

Time Expansion Chamber (TEC)

The TEC [39], shown in Figure 3.8, was the main tracking device of the L3 detector. It was installed on a beryllium pipe of 9 cm radius and was surrounded by an aluminium cylinder
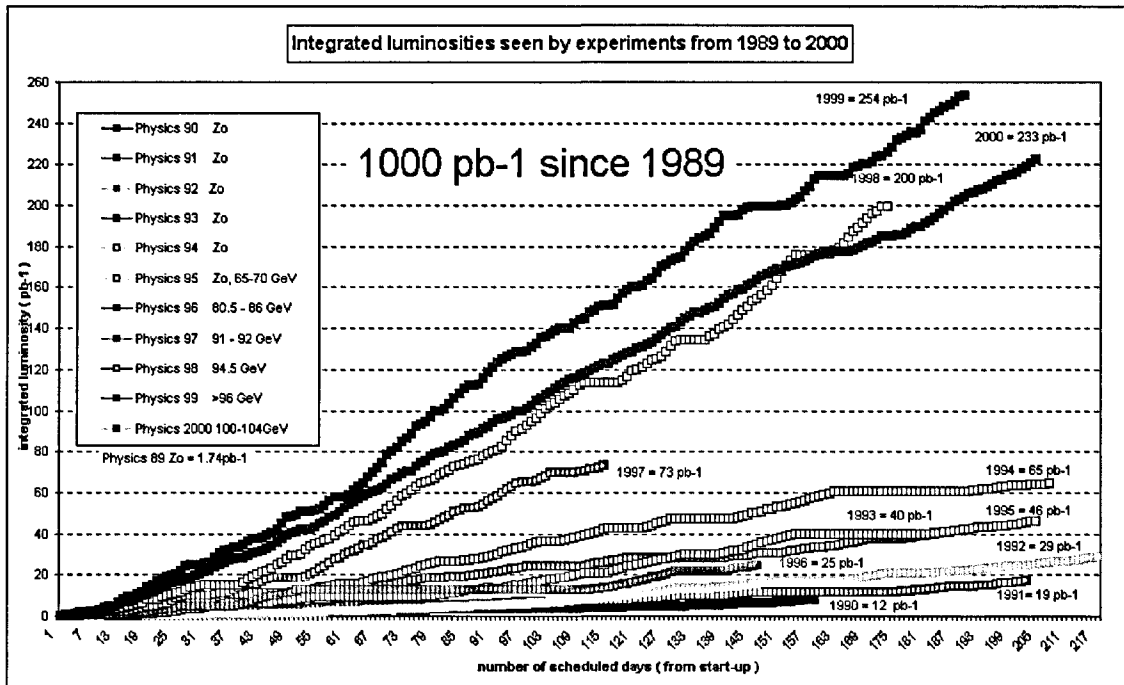
Figure 3.3: Integrated luminosity per experiment versus time for LEP. The particular lines represent the different years of operation.
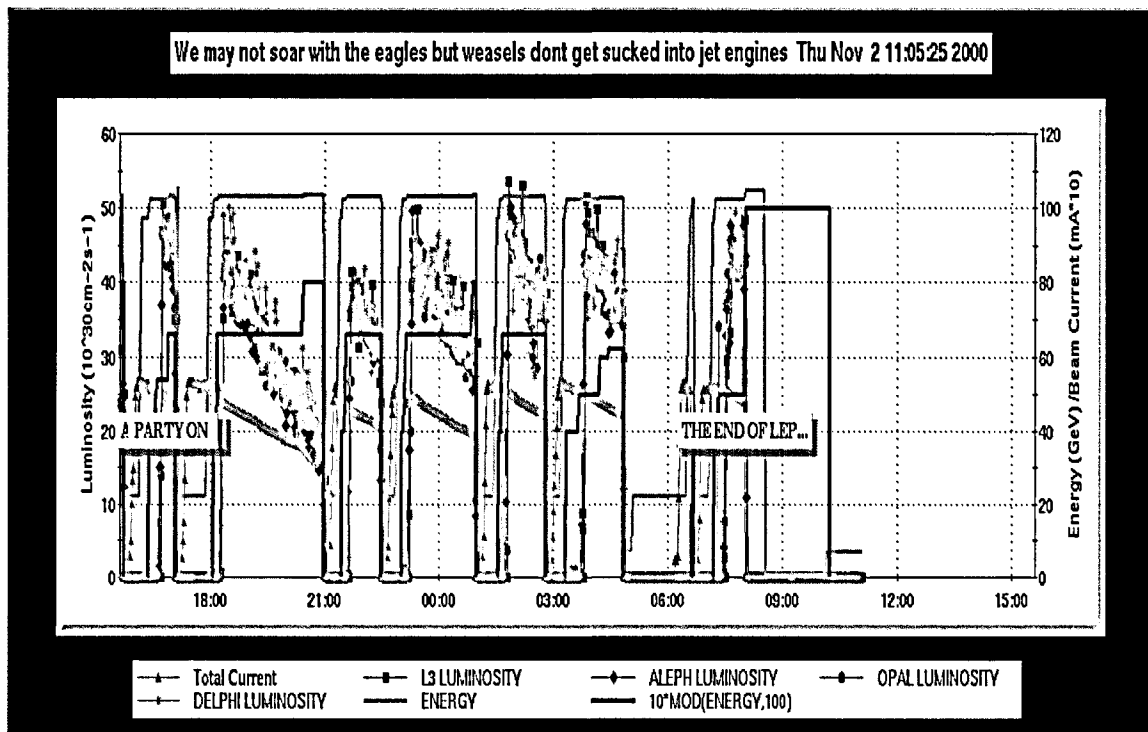

Figure 3.4: A historical picture: total current, energy and luminosities in the four detectors on the last day of LEP. After 12 years of operation with an extension in the last year to track down the longingly awaited Higgs boson, the LEP collider was shut down on 2nd November 2000 to be dismantled to make space for the LHC.
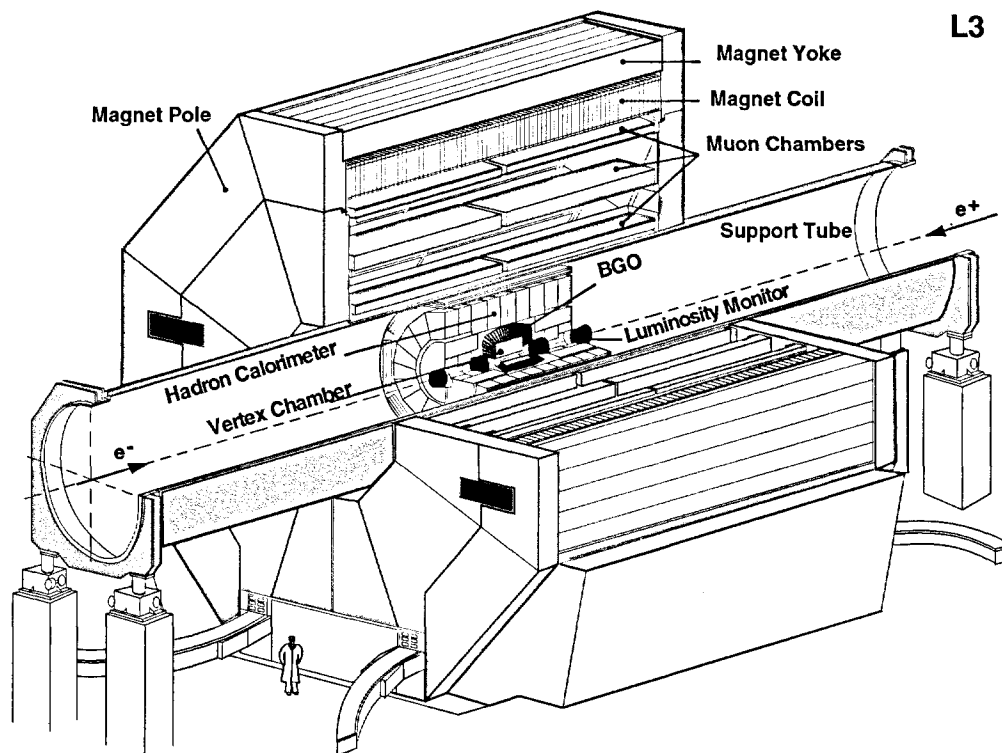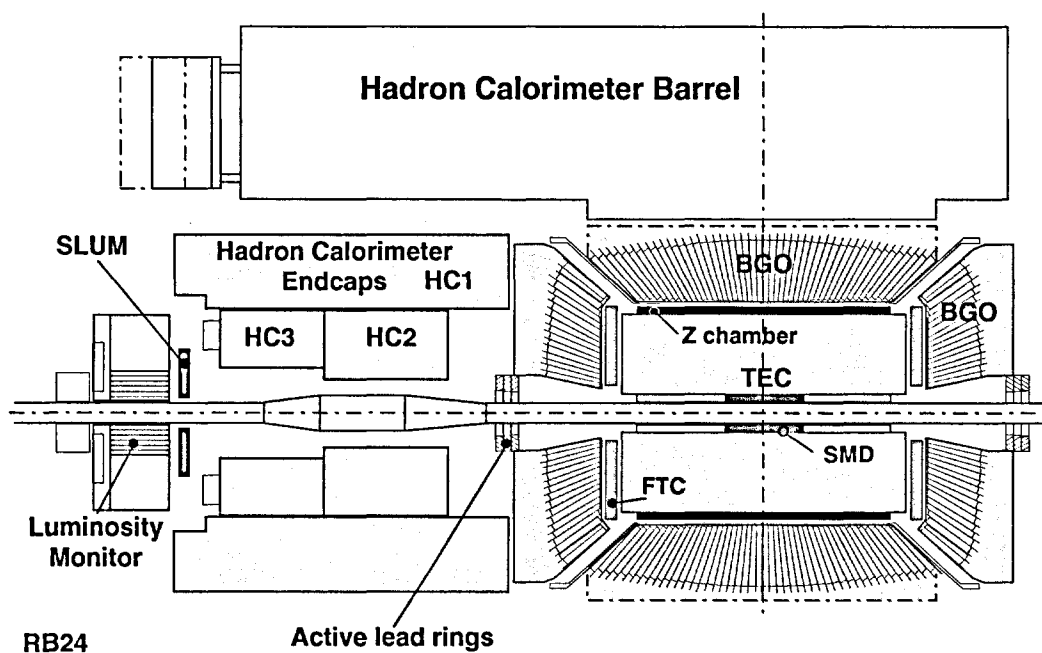
Figure 3.5: The L3 detector at LEP.

Figure 3.6: Side view of the inner detectors of L3, showing the central tracking system and the calorimetry system components. The luminosity monitor and its silicon tracker (SLUM) are also shown.
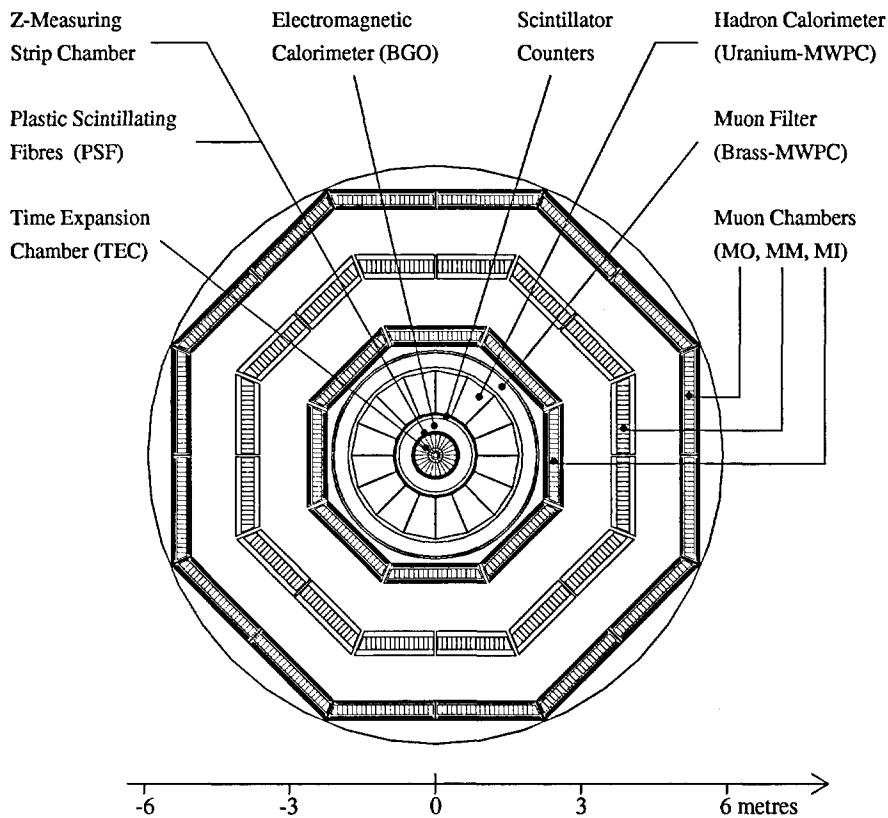
Z-Measuring
Strip Chamber

Electromagnetic
Calorimeter (BGO)

Scintillator
Counters

Hadron Calorimeter
(Uranium-MWPC)

Plastic Scintillating
Fibres (PSF)

Muon Filter
(Brass-MWPC)

Time Expansion
Chamber (TEC)

Muon Chambers
(MO, MM, MI)

-6   -3   0   3   6 metres

Figure 3.7: The L3 detector, view in the r-ϕ plane.

of 46 cm radius. The total lever arm for coordinate measurement was 31.7 cm radially, the sensitive length being 98 cm. The TEC consisted of two parts: the inner chamber, which was subdivided radially into 12 sectors, and the outer chamber, subdivided into 24 sectors. The sectors were surrounded by cathode wires, the anode wires were in the middle of the sectors (see Figure 3.9 (a)). A charged particle crossing the TEC radially could be measured by a maximum of 8 anode wires in the inner chamber and 54 wires in the outer chamber.

The TEC chamber was operated according to the time expansion principle, shown in Figure 3.9 (b): The drift area consists of a region with a low and homogeneous electric field (drift region) and a narrow region with a high electric field (amplification region) where the anodes are installed. In the drift region, the velocity of the drifting electrons is thus significantly lower, giving an improved time resolution. The amplification region with its high electric field ensures a high multiplication of the signal and thus a clean readout. The gas mixture used in the TEC consisted of 80% CO_2 and 20% iso-butane and was operated at a pressure of 1.2 bar and a temperature of 18°C.

The average spatial single wire resolution was 51 μm, the double-track separation 650 μm. The resolution on the distance of closest approach to the vertex (DCA) was 130 μm, and the average resolution on the ϕ angle was 5 mrad.
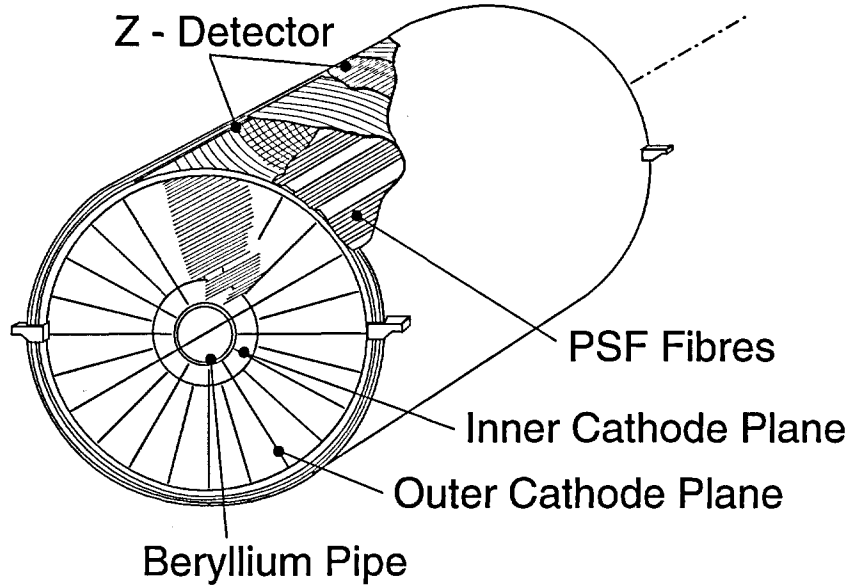
Figure 3.8: The TEC with its subcomponents.

The transverse momentum resolution of a wire chamber due to position measurement is described by the Gluckstern-formula [40]:

$$\frac{\sigma_{p_T}}{p_T^2} = \frac{\sigma_{R-\phi}}{0.3 \cdot B \cdot L^2} \sqrt{\frac{720}{N+4}}, \tag{3.4}$$

where p_T is the transverse momentum in GeV/c, B the magnetic field in Tesla, L the length of the lever arm in meters and N the number of equally spaced measurement points.

The momentum resolution of the L3 TEC was experimentally determined to be:

$$\frac{\delta_{p_T}}{p_T} = 0.02 \cdot p_T, \tag{3.5}$$

which was in reasonable agreement with the expected resolution from the Gluckstern formula. Tracks reconstructed using both the TEC and SMD have a slightly better momentum resolution of

$$\frac{\delta_{p_T}}{p_T} = 0.015 \cdot p_T. \tag{3.6}$$

The Z-detector [41], that covered the outer cylinder of the TEC, allowed the measurement of the z-coordinate of charged particles. It consisted of two cylindrical multiwire proportional chambers with cathode strip readout. The cathode strips were inclined with respect to the beam direction by 69° and 90° for the inner chamber, and by -69° and 90° for the outer chamber. This 69° angle was needed to measure the ϕ coordinate accurately enough to match a track measured in the Z-chamber with a TEC track. The single track resolution was 320 μm, the double-track resolution 10 mm.

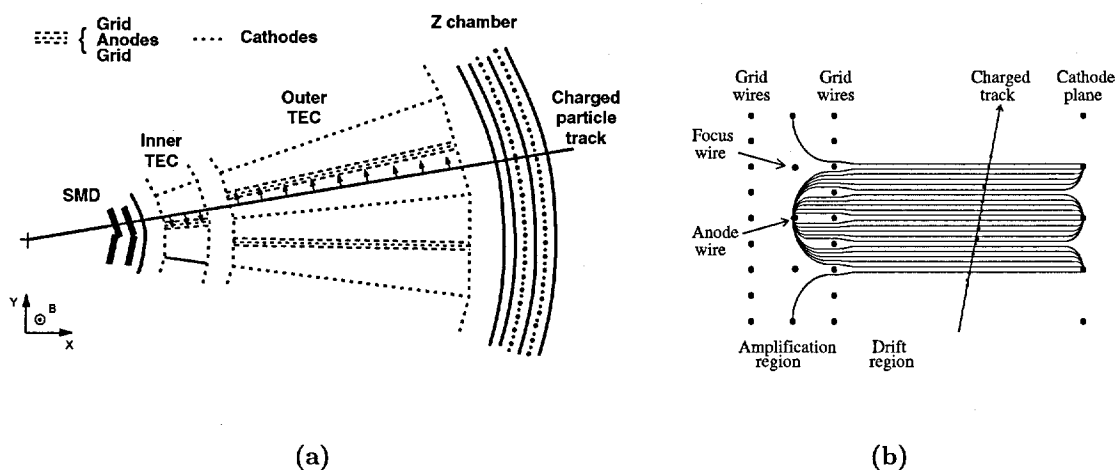(a)   (b)

Figure 3.9: (a) Schematic view of one inner sector and two outer sectors of the TEC. (b) The principle of the TEC. The region between anode and cathode wires is divided by grid wires into a drift region with a low field strength and an amplification region with high field strength.

3.2.2 The Calorimetric System

The calorimetric system of L3 consisted of an electromagnetic calorimeter, where electrons and photons were stopped, and a hadron calorimeter where all other particles entered. Most particles apart from muons and some punch-through hadrons would be stopped in the calorimeters and the additional muon filter on the outside of the hadron calorimeter.

Electromagnetic Calorimeter (BGO)

The L3 electromagnetic calorimeter [36] had an excellent energy resolution for photons and electrons over a wide energy range, from 100 MeV to 100 GeV. It consisted of about 11000 bismuth germanium oxide (BGO) crystals which were used both as showering and detecting medium. Figure 3.10 shows a schematic view of one such crystal. BGO crystals have a radiation length of 1.12 cm; this made it possible to keep the electromagnetic calorimeter relatively compact. The readout was done using two silicon photodiodes on each BGO crystal.

The whole subdetector consisted of two half-barrels and two endcaps. The BGO crystals were 24 cm long, and had a front surface of 2×2 cm^2 and a back surface of 3×3 cm^2. All crystals pointed towards the interaction point, with a small angular offset to reduce gaps for photon leakage.

As the light yield of BGO crystals is temperature dependent with a light output variation of (-1.55)% per °C, the BGO had to be maintained at a stable temperature. The stability within a few tenths of a degree was provided by a cooling system which dissipated the heat produced by the electronics located at the rear face of the crystals. Additionally, to prevent heat transfer from the outside, the calorimeter was surrounded
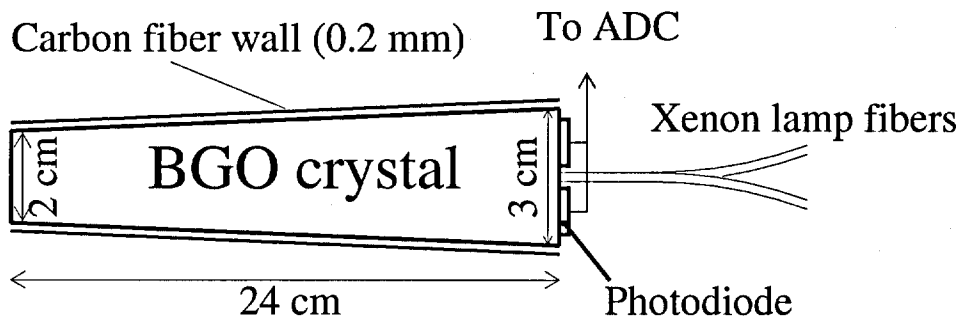
Figure 3.10: BGO crystal and part of the Xenon calibration system.

by very thin active thermal shields. The temperature at the front and the back of the crystals was monitored and the information was stored in a database and used in the reconstruction software.

The transparency of a BGO crystal is sensitive to ionising radiation doses, for instance one beam loss at LEP close to the L3 detector deposited a few Gray on the inner endcap crystals. The crystals recovered their transparency within a few days at room temperature. The scintillation efficiency was not affected by irradiation.

Generally, the energy resolution of calorimeters is composed of resolution effects due to statistical processes in the development of showers, and all other energy independent effects like noise, effects due to calibration errors, non-uniformities and non-linearities in photomultipliers, proportional counters, etc., which are a constant:

$$\frac{\sigma_E}{E} = \underbrace{\left(\frac{\sigma_E}{E}\right)_{\text{stat}}}_{\propto \frac{1}{\sqrt{E}}} + \underbrace{\left(\frac{\sigma_E}{E}\right)_{\text{syst}}}_{\propto \text{ const}} . \tag{3.7}$$

Before the installation, the crystals were calibrated to better than 1% in a test beam, using electrons with 2, 10 and 50 GeV momentum. The result of the calibration in the test beam was parametrised as:

$$\frac{\sigma(E)}{E} = \frac{a}{\sqrt{E}} + b , \quad \text{with } a = 1.54 \cdot 10^{-2} \text{ GeV}^{0.5}, b = 0.38 \cdot 10^{-2}, \tag{3.8}$$

which yields a resolution of 250 MeV at 45 GeV [42] for a single crystal. The resolution of the entire BGO achieved under running conditions at LEP was around 700 MeV at 45 GeV.

Figure 3.11 shows the energy resolution of the electromagnetic calorimeter for electrons as a function of the energy for test beam data and for events measured during LEP data taking. One sees that the achieved energy resolution at LEP for energies greater than 1 GeV is better than 2%.
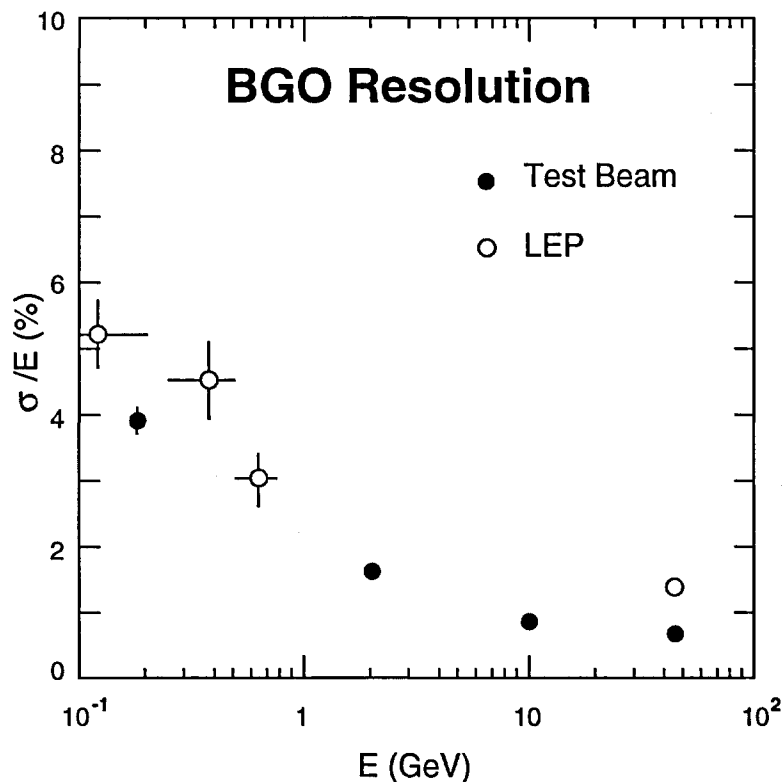
Figure 3.11: Energy resolution of the electromagnetic calorimeter as a function of the electron energy for test beam data and during LEP data taking.

As BGO crystals show a small signal loss with time, the calibration was repeated regularly using different methods. One method was using Xenon lamps. The light pulses generated by 16 Xenon flash lamps were guided to the back of the crystals using optical fibres; each crystal received high energy ($\sim$35 GeV) and low energy ($\sim$1.5 GeV) equivalent light pulses. Another method was to use a radiofrequency quadrupole accelerator (RFQ) to shoot 1.5 MeV protons on a Lithium target located near the centre of the L3 detector, producing Berillium and monochromatic photons of 17.7 MeV.

The global alignment of the electromagnetic calorimeter was done with respect to the tracking chamber. Bhabha events were used to achieve the alignment, comparing the predicted impact point of the particles on the BGO crystals from the tracking chamber with the actual position of the crystals.

Electromagnetic Gap Calorimeter

To improve the hermeticity of the calorimeter for LEP II, the gaps between the barrel and the endcap electromagnetic calorimeter were filled with a plastic scintillator (EGAP) [43], as shown in Figure 3.12. Hermeticity requirements are particularly important for searches for new particles. The EGAP calorimeter was divided into two halves, each composed of
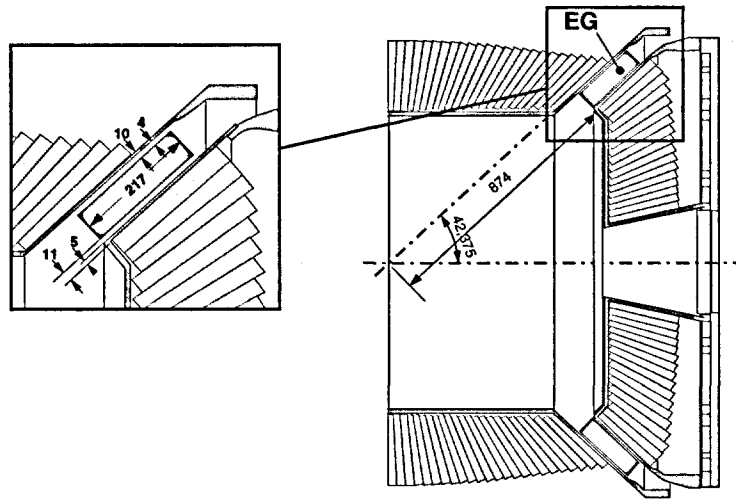
Figure 3.12: The position of the EGAP calorimeter within the electromagnetic calorimeter.

24 modules of trapezoidal shape. The relatively large modules resulted in a rather bad resolution of the azimuthal angle. To allow 24 groups of cables from the inner tracking device to be led out, some space was left between the modules.

The EGAP was used mainly as a veto to reject events with a considerable energy deposition outside the BGO range, and also for energy measurement. Its energy resolution for electromagnetically interacting particles was

$$\frac{\sigma(E)}{E} \approx 8\% \ . \tag{3.9}$$

Scintillators

The scintillation counter system [19], mounted between the electromagnetic and the hadron calorimeter had two goals. The scintillator hit multiplicity was used to trigger hadronic events and to measure the time of flight. This allowed to distinguish between dimuon events and cosmic ray background. A single cosmic ray muon which passed close to the interaction point could fake a dimuon event.

The time difference between opposite scintillation counters had been used for identification. For beam events, the time difference was approximately zero, while for cosmic events it was around 5.8 ns. The scintillation system consisted of 30 single plastic counters, which were mounted parallel to the beam pipe on the outer side of the barrel electromagnetic calorimeter and were read out on both sides by photomultipliers. The scintillators had a time resolution of 460 ps.
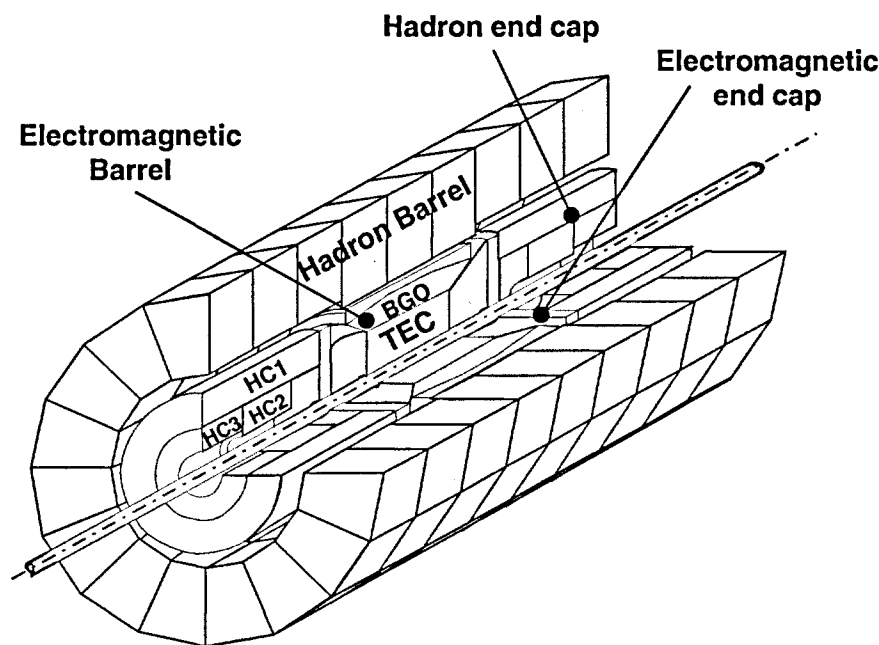
Figure 3.13: View of the inner detector with electromagnetic and hadron calorimeter.

The Hadron Calorimeter

The energy of hadrons was mainly measured in the hadron calorimeter [36]. Hadrons emerging from e^+e^- collisions were measured by the total absorption technique. The absorption was provided by plates made of depleted uranium, while particles were detected by proportional wire chambers. The intrinsic energy resolution for hadrons as obtained at a testbeam for the hadron and electromagnetic calorimeter together was [44]:

$$\frac{\sigma(E)}{E} = \frac{a}{\sqrt{E}} + b , \quad \text{with } a = 0.55 \text{ GeV}^{0.5}, b = 0.05 . \tag{3.10}$$

At LEP, the total energy of hadronic events from Z decay was measured with a resolution better than 10% [19].

The hadron calorimeter turned out to have quite good muon tracking properties, and this was used indirectly, *e.g.* for calibration or as a muon veto.

The barrel part covered angles between 35 and 145 degrees and consisted of depleted uranium absorber plates interspersed with proportional wire chambers. It was divided into 9 rings with 16 modules each, as shown in Figure 3.13. The wires in each module were grouped to form readout towers. For the absorber material, uranium was chosen for its short absorption length. The thickness of the electromagnetic and the hadron calorimeter including support structure was at least six nuclear absorption lengths.

The endcap hadron calorimeters extended the coverage of the calorimetry from $|\cos\theta| = 35$ down to 5.5 degrees, *i.e.* to 99.5% of 4π. Each endcap consisted of three separate rings

(HC1, HC2, HC3), with each ring split vertically into half-rings. Also the endcap part consisted of proportional chambers interspersed with depleted uranium absorber plates. The amount of material a particle passes through in the hadron calorimeter endcaps was at least six nuclear absorption lengths.

The hadron calorimeter, together with the dedicated muon filter, acted also as a filter. The muon filter was mounted between the barrel hadron calorimeter and the support tube (which was a passive absorber) and added 1.03 absorption lengths. It consisted of eight octants made of six 1 cm thick brass absorber plates, interleaved with five layers of proportional tubes and followed by 1.5 cm thick absorber plates.

3.2.3 Muon Detection System

The barrel muon system [45] consisted of two "Ferris wheels", each having eight independent octants. On each octant, five precision (P) drift chambers were mounted which measure track coordinates in the bending (r-ϕ) plane. Additionally, there were six chambers (z) which measure the z coordinate along the beam. All the chambers were mounted in three layers, with four z-chambers and two P-chambers in the outer layer (MO), two P-chambers in the middle layer (MM) and two z-chambers and one P-chamber in the inner layer (MI). Figure 3.14 shows the setup of the chambers in layers and a detailed view on the middle layer.

The momentum of a muon passing the chambers is determined from the sagitta (Figure 3.15), the deviation of the bent trajectory from a straight line. Each of the chambers in the middle layer contained 24 signal wires; the inner or outer chambers contained each 16 signal wires. The single wire resolution was about 150 μm.

The spectrometer covered polar angles between 44° and 136° with all three layers, angles between 36° and 144° with two layers. To achieve the design resolution, systematic errors in the alignment of the octants had to be kept to below 30 μm. For this, four different alignment systems were used.

The best momentum measurement was achieved if the muon was reconstructed in all three P-chambers (a so-called triplet). Then the momentum resolution is about 2.5% at $p_\mu = 45$ GeV. Figure 3.16 shows the momentum resolution for triplet muons. Doublets (muons with segments in only two of the P-chambers) had a momentum resolution of 21.3% [47].

The endcap muon spectrometers [48] were added in 1995 in order to cover a range down to 24° w.r.t. the beam axis. Figure 3.17 shows the design: 96 drift chambers were mounted in three layers - one inside the magnet doors, two on the outside of them, on both sides of the detector. One chamber consisted of two layers measuring the r-ϕ coordinate, and one layer measuring the r-z coordinate. The single wire resolution was about 250 μm. The momentum resolution varies from 4% (tracks having also hits in the MI and MM layers of the barrel muon chambers) to about 30% (very forward tracks, with hits only in MI).

A trigger was provided by Resistive Plate Chambers (RPC) attached to the drift chambers.
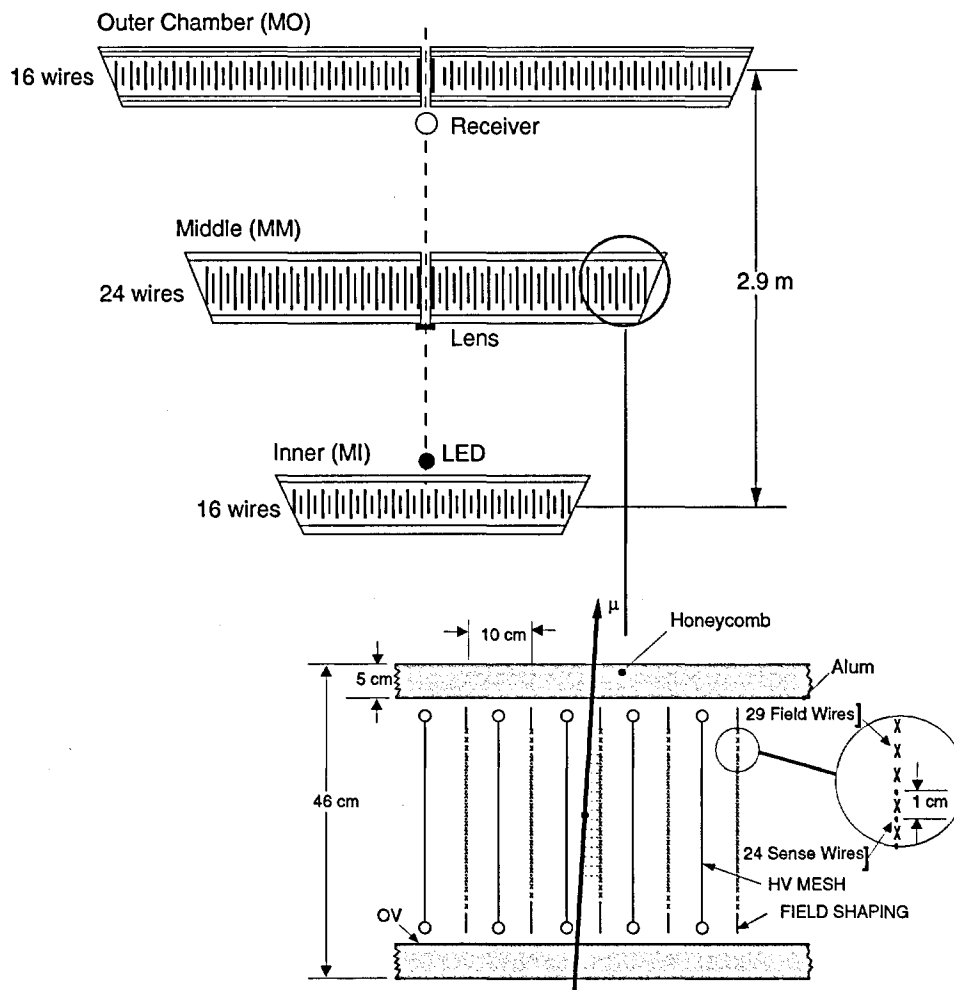
Outer Chamber (MO)

16 wires

○ Receiver

Middle (MM)

24 wires

2.9 m

Lens

Inner (MI) ● LED

16 wires

μ

Honeycomb

10 cm

5 cm

Alum

29 Field Wires

X
X
X
X
X

1 cm

46 cm

24 Sense Wires

HV MESH

OV

FIELD SHAPING

Figure 3.14: Setup of the chambers in layers and a detailed view on the middle layer.

2.9 m

$\vec{B}$ ⊗

s_2

S

s_1

s_3

μ⁻ Track

I : 16 wires

M : 24 wires

O : 16 wires
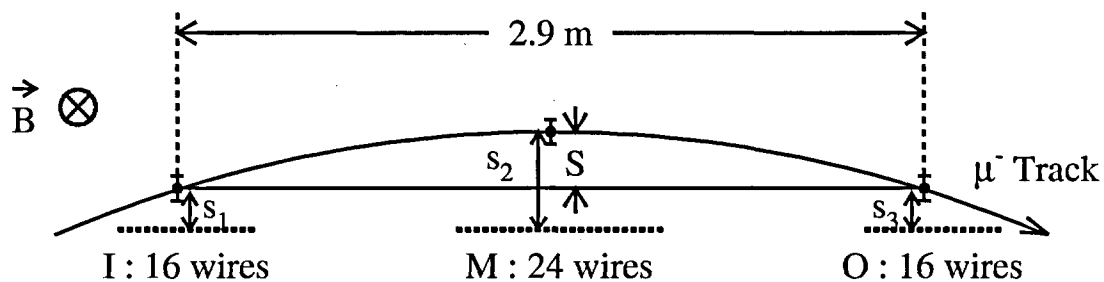
Figure 3.15: Schematical view of a track of a muon in the muon chambers.

$$e^+e^- \rightarrow Z^0 \rightarrow \mu^+ \mu^- (\gamma)$$
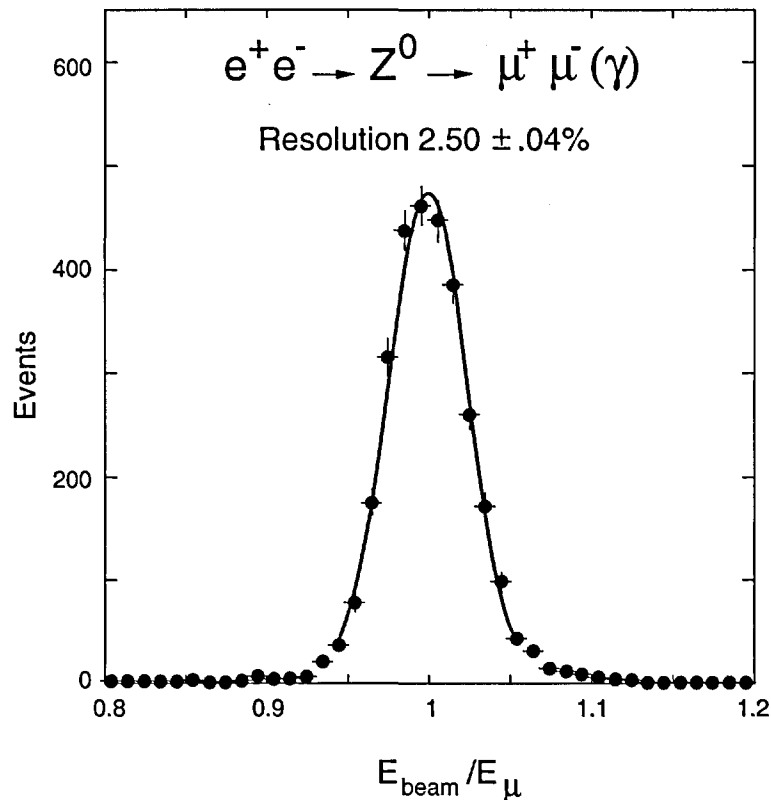
Resolution 2.50 ± .04%

Figure 3.16: Momentum resolution for muons measured in all three barrel muon chambers [46].

3.2.4 Magnet

The magnet in L3 consisted of a coil with an inside radius of 5.93 m and a length of 11.90 m, the return yoke on the outside of the coil, an active thermal shield on the inside to protect the detectors and the two magnet doors acting as poles. It needed about 4.2 MW for operation and gave a homogeneous field of 0.5 T over a large volume [36]. The poles were serving as a support for the 5600 tons of filling material which was needed for the magnetic flux return, both in the poles and in the barrel. The two poles were made as doors in order to access the muon detectors. In the inner volume of the support tube, the magnetic field was monitored by Hall probes, in the remaining volume with magnetoresistors, permanently installed on the muon chambers. Additionally, five NMR probes monitored the absolute value of the field.

3.2.5 Luminosity Monitors

The luminosity was determined from the number of Bhabha events, $e^+e^- \rightarrow e^+e^-$, measured at low scattering angles.

The L3 luminosity measurement system [49] consisted of a silicon tracker (SLUM) and an electromagnetic calorimeter (LCAL). The calorimetric luminosity monitor consisted of
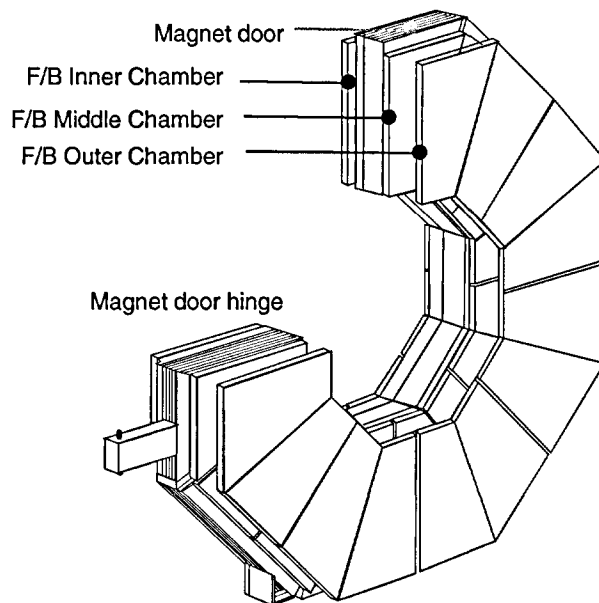
Figure 3.17: Design of the magnet doors and the endcap muon chambers.

BGO crystals, arranged as two symmetric half-detectors. Its purpose was to measure electrons and photons coming from Bhabha scattering. It was installed around the beam pipe on either side of the L3 detector, 2.8m from the interaction point. The LCAL covered the full ϕ-range from a radius of 68.2 mm to a radius of 191.4 mm. Each of the half-detectors contained a crystal matrix of 304 BGO crystals. To avoid radiation damage of the crystals during LEP filling, the detector was moved away from the beam pipe. Each half-detector was mounted on a hydraulic system which split the half-detector vertically w.r.t. the beam pipe. Each crystal was equipped with a LED for online monitoring of the efficiency loss and recovery due to radiation damage.

The silicon tracker was installed in 1993 in front of the LCAL to allow a better determination of its angular acceptance and a more precise measurement of the entry point of the particles into the LCAL. Each tracker consisted of three silicon wafers: two R-measuring layers with one ϕ-measuring layer in between.

The total systematic error of the luminosity measurement, $\Delta\mathcal{L}/\mathcal{L}$, was determined to be 0.5%, using the BGO calorimeter alone. The use of the silicon tracker allowed to reduce these uncertainties to around 0.15%.

3.2.6 Trigger System

At LEP the bunch crossing rate was 45 kHz in the 4×4 mode. The trigger system ensured that only interesting events were read out from the subdetectors and written to tape. The L3 trigger system was built up in three levels. At the first level, every subdetector system had its own trigger, which had to take the decision before the next bunch crossing 22.2 μs

later. If a positive decision was taken, the digitisation of the analog signal started. In parallel, all the analog data and the first level trigger decisions were passed to the second level trigger. The function of the second level trigger was to reject background selected by the first level trigger. If a negative decision was taken, the digitisation of the analog signals was stopped and the buffers were cleared to be ready for the next bunch crossing. The third level trigger took the digitised data as input and performed further checks before the data were written to tape.

First Level Trigger

The first level trigger consisted of five independent triggers: TEC trigger, inner TEC trigger, scintillator trigger, muon trigger and energy trigger. The TEC trigger was used to select events with charged particles. 14 out of 54 anode wires of the outer TEC were used to determine if good tracks are found. The inner TEC trigger was added in 1996. It used the 8 anode wires from the inner TEC sectors. The trigger was based on a Neural Network approach and took into account also matches with the outer sectors. The scintillator trigger selected high multiplicity events and rejected cosmic rays. The muon trigger consisted of two distinct parts: the barrel muon trigger and the forward-backward muon trigger. Decisions were taken independently. The triggers searched for hits in the chambers and scanned for predefined patterns. To rejects cosmic rays, a coincidence of the muon trigger and of the scintillator trigger was required. The energy trigger took its decision based on the signals of all calorimeters, *i.e.* the electromagnetic and hadronic calorimeter and the luminosity monitor calorimeter. The total level 1 trigger rate was of the order of 10 Hz, *i.e.* almost every signal in the detector was triggered.

Second Level Trigger

The second level trigger was invoked if only one of the first level triggers came to a positive decision. Events flagged as good by more than one first level trigger passed unhindered. The second level trigger based its decision on three filter algorithms: an energy, a muon, and a TEC algorithm. The rejection power was usually set to 20 to 30%.

Third Level Trigger

The third level trigger took as input the fully digitised event data. Several algorithms were used to analyse the event with the same granularity as during the offline analyses, dependent on the first level trigger which selected the event. Also here, events selected by more than one first level trigger passed unhindered. The typical rate reduction was between 40 and 60%, with an output rate of 2 to 3 Hz.

The output from this trigger was delivered to the main online computer, where all events were written to tape and selected events were delivered to ten separate monitoring programs.

3.2.7 Reconstruction of Events

The raw data taken at the detector have to be processed into quantities which are necessary for a physics analysis. Here, the L3 event reconstruction program REL3 is used. It decodes the raw data offline, applies calibration constants, and reconstructs the physics event. TEC and muon chamber tracks are reconstructed using the tracking chamber hits and the muon chamber hits, respectively. Calorimeter bumps from the electromagnetic and the hadron calorimeter are grouped into clusters to make the later physics analyses possible. All these reconstructed quantities are stored in files.

The most important file format for the physics analysis is the DVN which contains only reconstructed quantities, but only very little information from the detector is included. Its advantage is the smaller file-size[1], and thus higher processing speed during the physics analysis. Besides the DVN, L3 data are stored also in other formats which contain to a certain extent the raw information like hits and channel-by-channel calorimeter data etc., which are used mainly for calibration purposes or to understand the reconstructed objects on a lower level.

---

[1]A typical size per hadron on DAQ (data acquisition) level was 370 kByte, comparing to a size of 5 kByte in the DVN file.

Chapter 4

The W-Pair Event Sample

4.1 Data Sample

The LEP collider was operated from 1989 to 1995 at and around the Z pole. During this phase, called LEP I, a large statistics of about 5 million Z events per experiment was collected. In addition to the detailed study of Z decays, the data were used to understand the detectors in detail and to tune and develop Monte Carlo generators and detector simulation programs. In 1996, the LEP II program started, and the LEP centre-of-mass energy was raised above the W-pair production threshold.

In the following, the selection of $e^+e^- \rightarrow W^+W^-$ final states is described. The data sample consists of events collected during the years 1997-2000 with the L3 detector at LEP II. A luminosity of $684.8\,\text{pb}^{-1}$ has been collected at centre-of-mass energies $\sqrt{s} = 183 - 209$ GeV. This data sample is used for the measurement of W polarisation fractions. The data are grouped into several centre-of-mass energy bins, as shown in Table 4.1. For the study of W spin correlations and W decay-plane correlations, only data collected at centre-of-mass energies above 189 GeV, corresponding to a luminosity of 629.3pb^{-1}, are used.

Combining the decays of two W bosons (see Chapter 1.2.1), the final states of the process $W^+W^- \rightarrow f_1\bar{f}_2f_3\bar{f}_4$ are classified into the following categories:

- fully leptonic: $W^+W^- \rightarrow \ell_1\nu_1\ell_2\nu_2$, with a branching ratio of:
  $BR(W^+W^- \rightarrow \ell_1\nu_1\ell_2\nu_2) = BR(W \rightarrow \ell_1\nu_1) \cdot BR(W \rightarrow \ell_2\nu_2)$ per lepton-combination,
  $i.e.$ $(3 \cdot 0.11)^2 = 0.11$,

- semi-leptonic (or semi-hadronic): $W^+W^- \rightarrow \ell\nu q_1\bar{q}_2$, with a branching ratio of:
  $BR(W^+W^- \rightarrow \ell\nu q_1\bar{q}_2) = BR(W \rightarrow \ell\nu) \cdot BR(W \rightarrow q_1\bar{q}_2) \cdot 2$, $i.e.$ $(3 \cdot 0.11) \cdot 0.67 \cdot 2 = 0.44$,

- fully hadronic: $W^+W^- \rightarrow q_1\bar{q}_2q_3\bar{q}_4$, with a branching ratio of:
  $BR(W^+W^- \rightarrow q_1\bar{q}_2q_3\bar{q}_4) = BR(W \rightarrow q_1\bar{q}_2) \cdot BR(W \rightarrow q_3\bar{q}_4)$ per quark-combination,
  $i.e.$ $0.67^2 = 0.45$.

Out of these final states, the semileptonic channel with an electron or a muon offers the best possibilities for almost all measurements and especially the polarisation measure-

Year	1997	1998	1999				2000
$\langle\sqrt{s}\rangle$ [GeV]	182.7	188.6	191.6	195.5	199.5	201.8	205.9
Integrated luminosity [pb^{-1}]	55.5	176.8	29.8	84.1	83.3	37.2	218.1
σ_{WW} [pb]	15.72	16.5	16.8	17.1	17.2	17.3	17.5
$\sigma_{q\bar{q}(\gamma)}$ [pb]	101.8	100.9	97.57	92.51	88.03	85.81	80.97
σ_{ZZ} [pb]	0.59	0.97	1.08	1.19	1.26	1.28	1.33

Table 4.1: Average centre-of-mass energies, integrated luminosities and cross-sections for W-pair events and for the main background processes at different energies.

ments. Its advantages are the possibility of charge assignment for the W boson, using the identified lepton charge and the fact that all W decay angles can be reconstructed in a straightforward way. The events are easy to select and an essentially background free sample can be obtained.

The selection of semileptonic events is based on high multiplicity events with an isolated, energetic electron or muon. The neutrino is indirectly seen in the detector, as its four-vector is reconstructed using the energy and momentum conservation law. The charge of the leptonically decaying W boson is assigned to be the charge of the corresponding lepton. All other particles in the event originate from the two quarks in the decay of one of the W bosons. Figure 4.1 shows an example of a selected candidate for $W^+W^- \rightarrow \mu\nu q_1\bar{q}_2$ as seen in the L3 detector.

For the measurements described in Chapters 5, 6 and 7, events of the type $e^+e^- \rightarrow W^+W^- \rightarrow e\nu q_1\bar{q}_2$, $\mu\nu q_1\bar{q}_2$ are used. These channels constitute about 30% of all W-pair final states.

Fully leptonic events, which include at least two neutrinos, are not used for the analysis, as the two neutrinos lead to a two-fold ambiguity when assigning the missing momentum, which makes a correct determination of the angles impossible. In addition, fully leptonic events (including events involving decays into taus) constitute only about 11% of all W-pair final states, which reduces the importance of this channel in any case.

Fully hadronic events constitute about 46% of all W-pair final states, which makes this channel important in order to increase statistics. However, there are several difficulties: This channel has a large irreducible background of $e^+e^- \rightarrow q\bar{q}(\gamma)$ events. Additionally, there are problems with the correct pairing of the jets to reconstruct the W bosons, which makes it also necessary to consider the wrongly-paired events on a statistical basis as an irreducible background. Also the charge of the W bosons cannot be assigned due to the fact that the charge of the quark in hadronic decays is difficult to measure[1]. Figure 4.2 shows an example of a four-jet event as seen in the L3 detector. Because of these characteristics, fully hadronic events are used only for the measurement of decay plane

---

[1] Through the fragmentation mechanism quarks build jets, hence one could try to identify the charge of the quarks ($-\frac{1}{3}$ for down-type quarks or $+\frac{2}{3}$ for up-type quarks) by "summing up the charges" of all hadrons found in the originating jet, weighted according to their momentum. In practise, the probability to do this right turns out to be only little more than 50%, i.e. little better than guessing, due to problems with jet fluctuations.
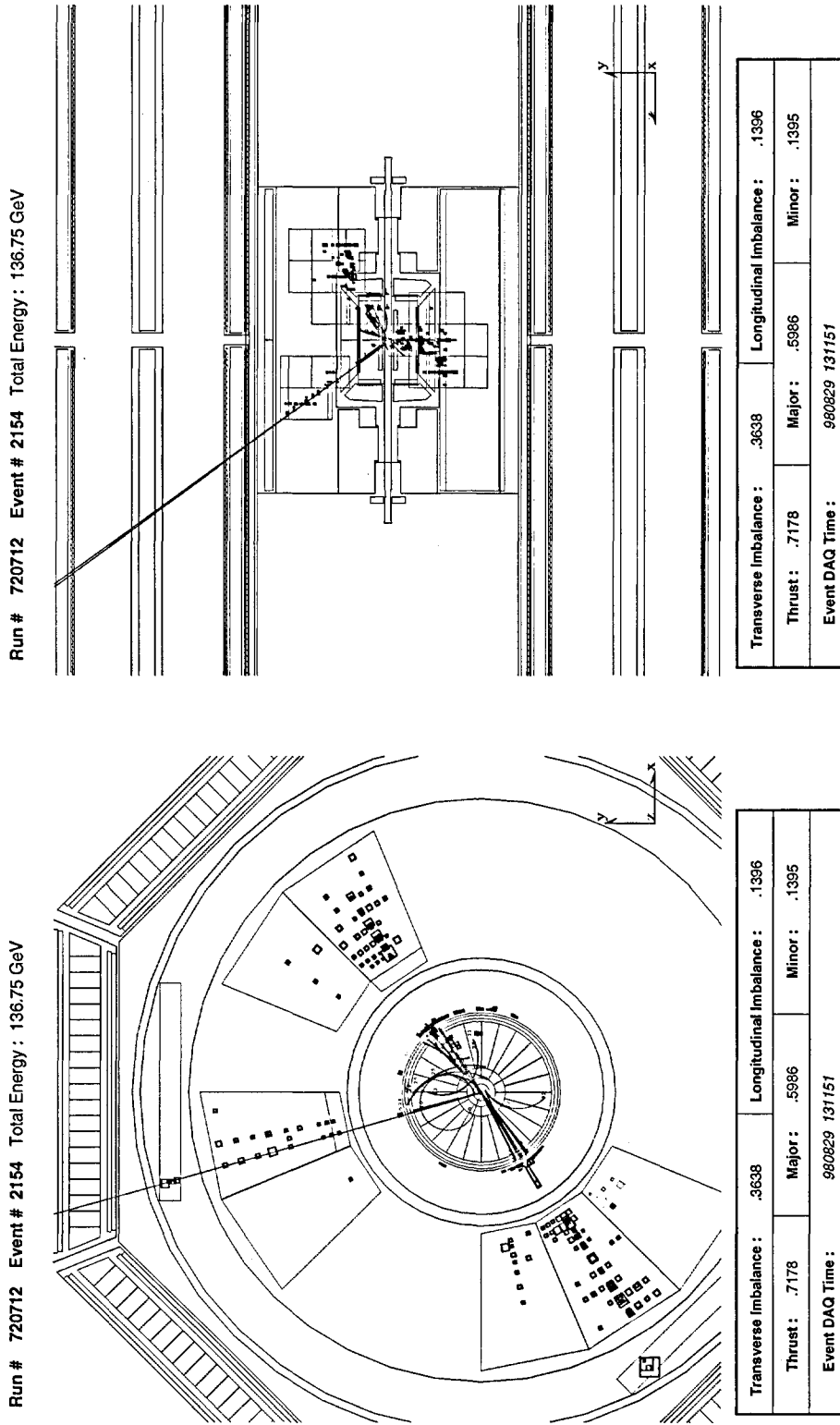
Figure 4.1: A $W^+W^- \to \mu\nu q_1\bar{q}_2$ event as seen in the L3 detector.

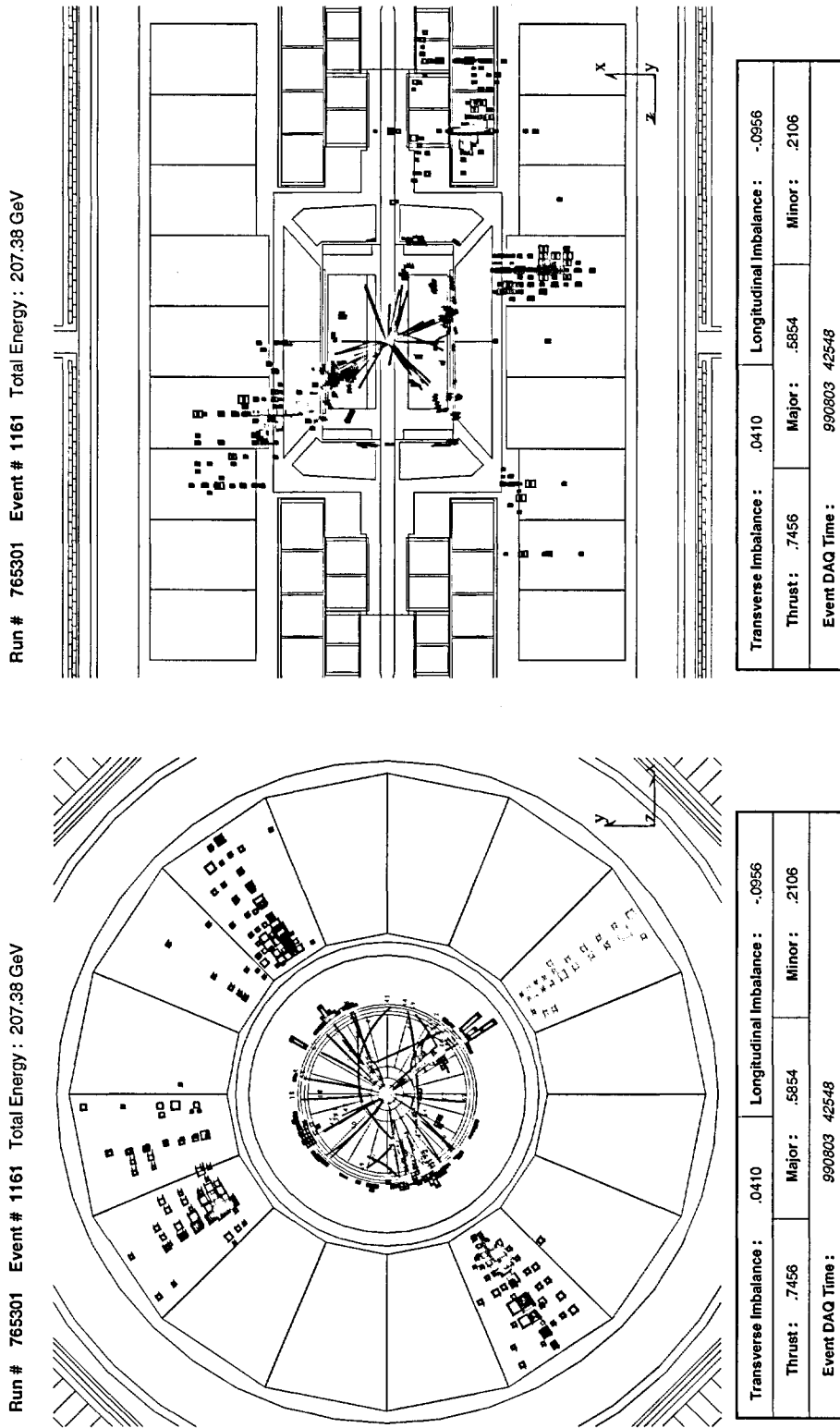Run # 765301   Event # 1161   Total Energy : 207.38 GeV

Transverse Imbalance :	.0410	Longitudinal Imbalance :	-.0956
Thrust : .7456	Major : .5854	Minor : .2106	
Event DAQ Time :	990803 42548		

Run # 765301   Event # 1161   Total Energy : 207.38 GeV

Transverse Imbalance :	.0410	Longitudinal Imbalance :	-.0956
Thrust : .7456	Major : .5854	Minor : .2106	
Event DAQ Time :	990803 42548		

Figure 4.2: Example of a signature of a $e^+e^- \rightarrow W^+W^- \rightarrow q_1\bar{q}_2q_3\bar{q}_4$ event in the L3 detector.

correlations described in Chapter 7.

The kinematics of semileptonic events involving a tau are also difficult to reconstruct accurately due to the fact that the tau decays well before reaching the inner subdetectors, and all tau decays involve at least one additional neutrino. Two or more neutrinos lead to an ambiguity when assigning the missing momentum to the neutrino coming from the W decay, which makes a correct determination of the angles impossible for the measurement described here.

The characteristics of the signal events can thus be summarised as follows:

- $e^+e^- \to W^+W^- \to e\nu q_1\bar{q}_2$, $\mu\nu q_1\bar{q}_2$ have high multiplicity, some missing momentum and an isolated energetic electron or muon. The mass of the two reconstructed W bosons should be close to the on-shell W mass.

- $e^+e^- \to W^+W^- \to q_1\bar{q}_2q_3\bar{q}_4$ have high multiplicity, the observed hadrons can be clustered into four jets. It does not contain any isolated energetic electrons or muons. The mass of the two reconstructed W bosons should be close to the on-shell W mass.

4.2 Background Processes

For comparison, the cross-sections for the W^+W^- and important background processes at the particular $\sqrt{s}$ points are given in Table 4.1. Several backgrounds are considered for semileptonic and fully hadronic W^+W^- final states. Backgrounds coming from other W^+W^- final states are:

- $e^+e^- \to W^+W^- \to \tau\nu q_1\bar{q}_2$
  This final state is a background for the semileptonic W-pair final states. Especially tau decays into $e^-\bar{\nu}_e\nu_\tau$ or $\mu^-\bar{\nu}_\mu\nu_\tau$ (each with about 18% branching ratio) are indistinguishable from the final state electron or muon from the $e^+e^- \to W^+W^- \to e\nu q_1\bar{q}_2$, $\mu\nu q_1\bar{q}_2$ processes.

- $e^+e^- \to W^+W^- \to q_1\bar{q}_2q_3\bar{q}_4$
  These final states, with misidentified electrons or muons are also a potential background for semileptonic final states, although it is strongly reduced by isolation cuts.

- $e^+e^- \to W^+W^- \to e\nu q_1\bar{q}_2$, $\mu\nu q_1\bar{q}_2$
  Some semileptonic events, in particular $W \to \tau\nu$ with the tau decaying into hadrons, can mimic a four jet event under certain circumstances and hence are considered as background for the $q_1\bar{q}_2q_3\bar{q}_4$ selection.

Additionally, backgrounds from other processes need to be investigated:

- $e^+e^- \to q\bar{q}(\gamma)$
  The cross-section for this process is very high, typically around 80 to 100 pb^{-1}, depending on $\sqrt{s}$, which is about 10-20 times larger than the signal. Typically an

energetic photon, called initial state radiation (ISR), is emitted along the beam pipe, leading to a lower energy seen in the detector. The quarks can emit gluons leading to the formation of further jets. This process is an important background for $W^+W^- \to q_1\bar{q}_2q_3\bar{q}_4$ and a negligible background for $W^+W^- \to \ell\nu q_1\bar{q}_2$ events.

- $e^+e^- \to ZZ$
  The cross-section of this process is about 10 times smaller than for signal events. This process is a background for the fully hadronic channel as about 70% of the ZZ events have a four jet final state and can only be distinguished by the mass of the two jet-jet systems, which is equal to the mass of the Z boson. As the cuts around the W mass have to be large to maximise the efficiency, it remains an irreducible background for the $W^+W^- \to q_1\bar{q}_2q_3\bar{q}_4$ signal.

- Single W processes ($e^+e^- \to We\nu \to e\nu q_1\bar{q}_2$)
  This process has the same final states as $W^+W^- \to e\nu q_1\bar{q}_2$. However, due to the fact that their production involves only one on-shell W boson, and the electron is dominantly emitted along the beam pipe, they can be easily removed from the event sample with a few cuts.

4.3   Monte Carlo Samples

Several Monte Carlo programs are used to simulate signal and background events. The L3 detector response is simulated with the GEANT [50] and GHEISHA [51] packages. GEANT delivers a general description concerning geometry and material of the detector and simulates all interactions of the particles with the respective materials. GHEISHA is a simulation package used for hadronic interactions.

Additional detector inefficiencies, which are monitored for every data taking period, are included where relevant. For semileptonic signal Monte Carlo, a reweighting was applied to reproduce the pattern of hits in the muon chambers, *i.e.* the correct ratios of muons reconstructed in three barrel muon chambers (triplet muons), in two barrel muon chambers (doublet muons), in two barrel and one forward muon chambers, and only in the forward muons chambers. Furthermore, the reconstructed visible energy in all signal Monte Carlo events was slightly shifted and smeared in order to reproduce the respective distributions observed in data.

For all Monte Carlo generators, PYTHIA [52] is used to simulate the fragmentation of the final state quarks.

For each centre-of-mass energy, a sample of 100'000 $e^+e^- \to W^+W^-$ events with all final states is generated using the KORALW Monte Carlo [53]. The KORALW program includes radiative corrections, initial state radiation (ISR) processes and first order final state radiation (FSR) processes. These Monte Carlo events are used to obtain efficiencies and to compare with the Standard Model predictions.

The EEWW [54], YFSWW [55] and EXCALIBUR [56] Monte Carlo programs are also used to study systematic effects. The EEWW Monte Carlo contains pure s-channel and t-channel W^+W^- processes only, without radiative corrections, and uses the zero-width

approximation for the W boson. However, it is important for this analysis as it assigns W helicities on an event-by-event basis. The YFSWW Monte Carlo generator includes improved $\mathcal{O}(\alpha)$ corrections. The EXCALIBUR program is used to study systematic effects coming from non double-resonant processes with the same final states as the signal.

As explained in the previous section, misidentified W^+W^- decays of another decay channel constitute background for the analysed final states. Thus the samples generated using KORALW are also used to study background coming from other W^+W^- final states. The Monte Carlo programs used to generate other backgrounds are PYTHIA [52] and KK2F [57] for the $e^+e^- \rightarrow q\bar{q}(\gamma)$ process, and PYTHIA for the $e^+e^- \rightarrow ZZ$ process.

4.4 Particle Identification

Electrons, muons and photons are identified as follows.

High energy electrons are identified in the electromagnetic calorimeter as isolated energy depositions with a shower shape consistent with the expected electromagnetic shower shape. A cut on $\left(\frac{1}{E} - \frac{1}{p}\right)$ is not performed due to the relatively large systematic uncertainty on the momentum of the charged particles measured in the TEC as compared to the energy uncertainty. The electromagnetic shower shape is characterised by a very localised large energy deposition in a few crystals (3 by 3 crystal matrix) and only low energy deposition in the surrounding 16 crystals. The ratio of the energy in the 3×3 matrix of crystals surrounding the maximum energy deposition to the 5×5 crystal matrix, E_9/E_{25}, was chosen to be larger than 0.98. A match of this cluster in azimuthal angle with a reconstructed track in the central tracking chamber is required. A reconstructed track is a track with a momentum of at least 5 GeV and at least 10 TEC hits.

Photons are identified in the electromagnetic calorimeter as isolated energy depositions with an electromagnetic shower shape, which have no track assigned. The number of crystals with an energy deposition must be at least 5, with the energy E_9 larger than 0.1 GeV and the ratio E_9/E_{25} larger than 0.98.

Muons are identified and measured as tracks reconstructed in the muon chambers which point back to the interaction vertex. In order to fulfil the latter requirement, the muon trajectory must have a distance of closest approach (DCA) in the x-y-plane to the interaction point of less than 50 mm and a distance of less than 50 mm in the z-direction parallel to the beam. To reduce any potential bias in the momentum measurement of the muons in the muon chambers, the associated energy deposited in the hadron calorimeter has to be smaller than 10 GeV. To allow a good measurement of the muon momentum, the muons are required to have track elements in at least two chambers measuring the r-ϕ coordinates and one hit in a chamber measuring the z-coordinates.

For this analysis, all other energy depositions in the calorimeters larger than 0.2 GeV are assigned to hadrons. The neutrino momentum vector is defined as the missing momentum vector of the event.

4.5   Event Selection

The analysis starts from data collected at centre-of-mass energies $\sqrt{s} = 183 - 209$ GeV which are processed into the DVN format files (see section 3.2.7). During the DVN processing some minimal quality cuts are set, which reduce background in the detector not coming from an e^+e^- collision like cosmic muons, noise from uranium in the hadron calorimeter, and unused hits in the central tracking chamber [58]. This helps to reduce the size of the files to be processed during the final stages of the selection. These minimal cuts are set very low such that any physics analysis performed later includes or surpasses the cut values. In addition to these cuts, a visible energy of at least 0.3 times the centre-of-mass energy is required.

The selection efficiently separates signal from trivial background events. Its aim is to obtain a clean and almost unbiased well measured signal sample. The quantities efficiency and purity, used to characterise the event selection are defined as follows:

$$\text{efficiency} = \frac{\text{number of accepted signal events}}{\text{total number of signal events}} \qquad (4.1)$$

$$\text{purity} = \frac{\text{number of accepted signal events}}{\text{total number of accepted events}} \qquad (4.2)$$

The efficiency of a selection gives the probability of selecting a signal event, the purity is the probability that the selected events is a signal event. The selection is always a compromise between efficiency and the other requirements, and is based on variables which separate the signal from the background.

In the following, the two selections are described. They are tuned to select clean events corresponding to the topologies described in section 4.1.

4.5.1 $W^+W^- \rightarrow e\nu q_1\bar{q}_2, \mu\nu q_1\bar{q}_2$ Events

Figure 4.3 shows the distribution of the reconstructed visible energy for Monte Carlo, where no selection cut has been applied. We see that the event sample is dominated by background. In the raw data, all processes which have been measured at L3 are included. The additional processes constitute an additional background, their topology however is completely different from the signal process, and they are removed with very few simple cuts which are included implicitly in the selection.

The used event selection variables and cuts are given in the following. Figure 4.4 shows the distributions of those variables for data and Monte Carlo as (N-1) plots, *i.e.* all cuts except the one shown are applied. The distributions from all energies are added to obtain the total distributions.

- The reconstructed electron momentum must be greater than 20 GeV (Fig. 4.4 a),

- The reconstructed muon momentum must be greater than 15 GeV (Fig. 4.4 b).

- Only events which contain exactly one electron or one muon candidate are accepted.
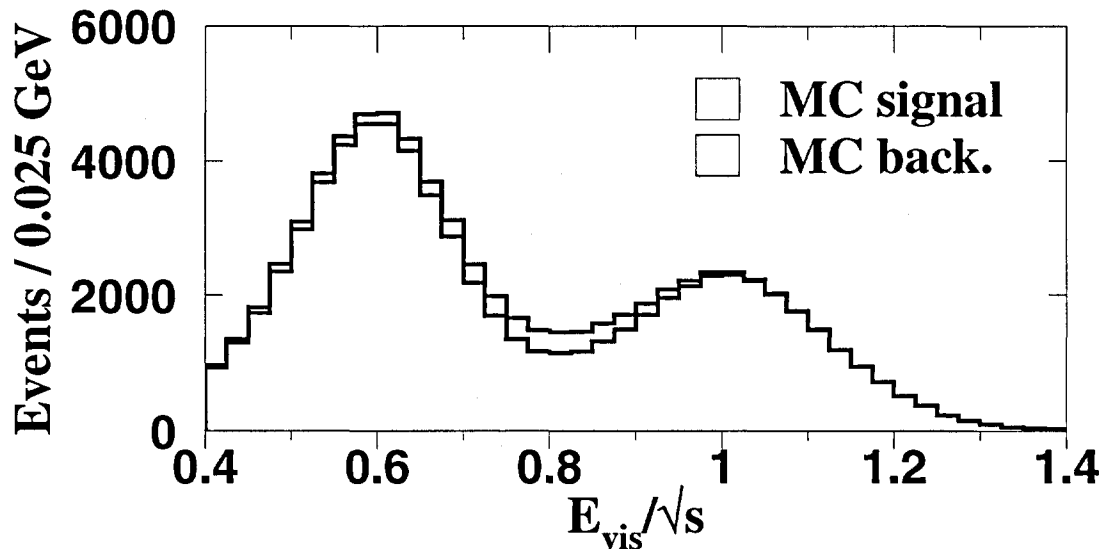
Figure 4.3: Initial distribution for KORALW Monte Carlo $W^+W^- \rightarrow \ell\nu q_1\bar{q}_2$ events for normalised visible energy, where no selection cut has been applied. The background histograms include only the most important processes $e^+e^- \rightarrow q\bar{q}(\gamma)$ and $e^+e^- \rightarrow W^+W^- \rightarrow \tau\nu q_1\bar{q}_2$.

- In order to use the neutrino four vector for the definition of the neutrino polar decay angle, the neutrino momentum must be greater than 10 GeV (Fig. 4.4 c). Looking at the Figure this cut seems not to be needed. It becomes important as soon as the other cuts are changed (*e.g.* for systematics studies), allowing to remove some background.

- To avoid misidentification of particles which escaped through the beam pipe as neutrinos, the neutrino polar angle, θ_ν, has to satisfy $|\cos\theta_\nu| < 0.95$ (Fig. 4.4 d).

- The invariant mass of the lepton-neutrino system has to be consistent with the W boson mass, *i.e.* greater than 60 GeV (Fig. 4.4 e)

- The invariant mass of the hadronic system has to be consistent with the W boson mass, *i.e.* between 50 and 110 GeV (Fig. 4.4 f).

The W boson candidate mass peaks (e) and (f) are slightly shifted in their centre with respect to the Monte Carlo, however the cuts are applied well outside the central region and the precise mass is not relevant to this analysis.

4.5.2 $W^+W^- \rightarrow q_1\bar{q}_2q_3\bar{q}_4$ Events

The selection of the $q_1\bar{q}_2q_3\bar{q}_4$ final states accepts only events with a four-jet topology, thus removing most hadronic events coming from $e^+e^- \rightarrow q\bar{q}(\gamma)$ and $e^+e^- \rightarrow ZZ$.
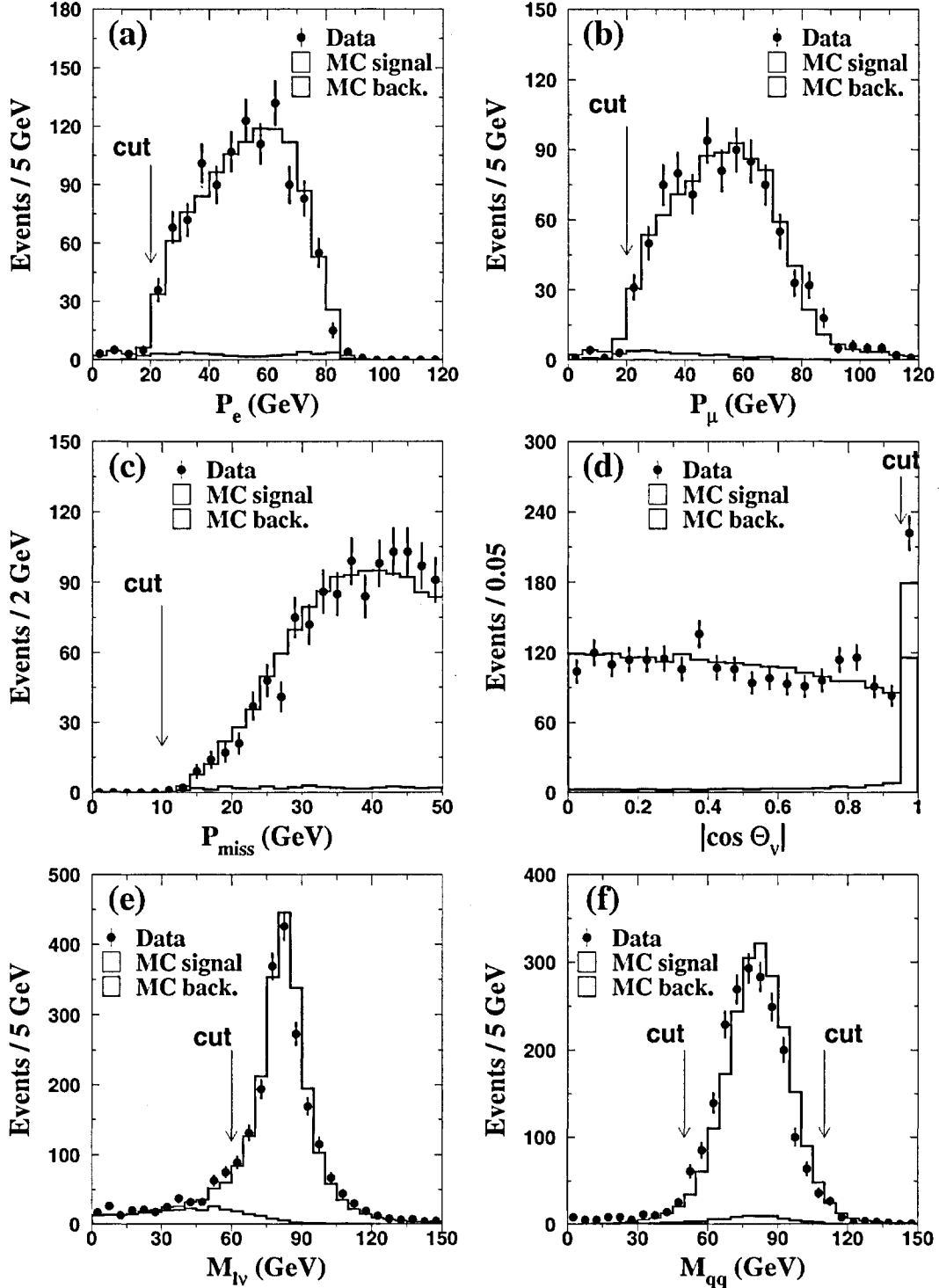
Figure 4.4: Distributions of variables used for the selection of $e^+e^- \rightarrow W^+W^- \rightarrow \ell\nu q_1\bar{q}_2$ events: (a) momentum of the electrons, (b) momentum of the muons, (c) missing momentum (d) absolute value of the cosine of the polar angle of the neutrino, (e) mass of the lepton-neutrino system, (f) mass of the hadronic system. In each plot, all other selection criteria are applied. The arrows indicate cut positions. The distributions are shown for centre-of-mass energies $\sqrt{s} = 183 - 209$ GeV with an average of $\langle\sqrt{s}\rangle = 196.7$ GeV.
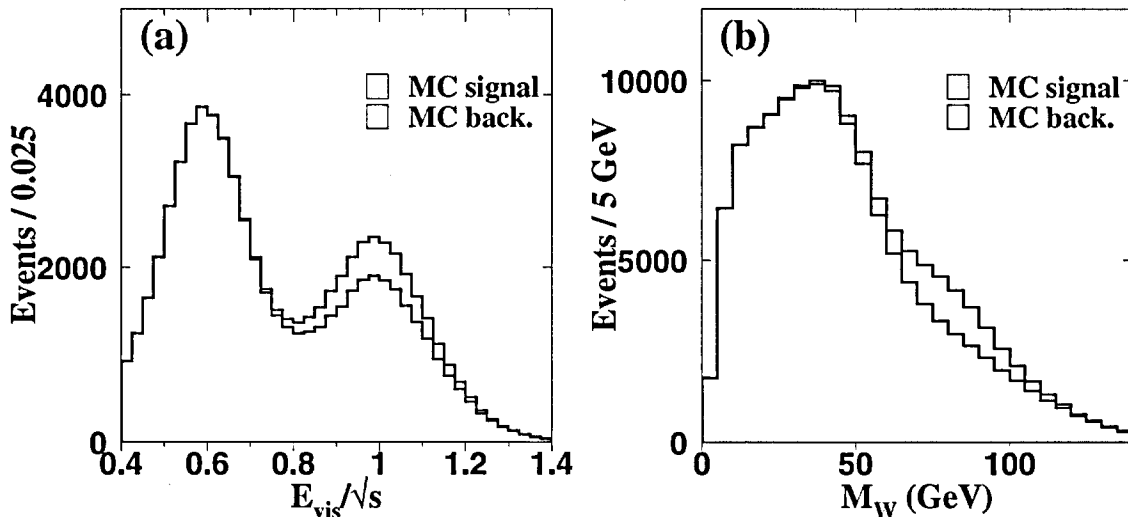
Figure 4.5: Initial distributions for the fully hadronic sample signal, $W^+W^- \rightarrow q_1\bar{q}_2q_3\bar{q}_4$, for (a) normalised visible energy and (b) reconstructed W mass, where no selection cut has been applied. The background histograms include the most important processes $e^+e^- \rightarrow q\bar{q}(\gamma)$, $e^+e^- \rightarrow ZZ$ and $e^+e^- \rightarrow W^+W^-$ decaying not into four quarks.

Figure 4.5 shows two distributions for Monte Carlo where the signal Monte Carlo events are plotted together with the most important background processes without application of any selection cut. The sample shown is clearly dominated by background. The raw data consists of all processes measured at L3, *i.e.* also processes with topologies that are completely different from the signal W pair events. These events are not simulated by the Monte Carlo used and are removed entirely with a few simple cuts, *e.g.* a high-multiplicity cut.

In the following, the selection criteria used for $W^+W^- \rightarrow q_1\bar{q}_2q_3\bar{q}_4$ events are described. Figures 4.6 and 4.7 show the distributions of the selection variables for data and Monte Carlo as (N-1) plots. The distributions from all energies, $\sqrt{s} = 189 - 209$ GeV, are combined.

First, high multiplicity events are selected by requiring more than 20 accepted charged tracks (Fig. 4.6a) and more than 25 accepted calorimetric clusters (Fig. 4.6b). For this analysis, a track is accepted if it has a ratio of the number of hits to its span of more than 0.5, the distance of closest approach (DCA) in the r-ϕ plane to the event vertex is less than 10.0 mm and the transverse momentum is larger than 0.2 GeV. An accepted calorimetric cluster must have an energy of more than 0.3 GeV.

Further selection cuts are based on variables calculated from the particles identified in the events. These variables are the visible energy, the thrust value and the cosine of the polar angle of the thrust axis of the whole event, the total missing momentum of the event, and the energies of the identified electrons, photons and muons. The thrust value is calculated from the four-vectors of all hadrons by maximising the longitudinal

momentum w.r.t. the corresponding thrust axis. The thrust value T is defined as:

$$T = 2 \max_{\vec{n}} \frac{\sum \vec{p} \cdot \vec{n}}{\sum |\vec{p}|} , \tag{4.3}$$

where $\vec{n}$ is the thrust axis, and is chosen in order to maximise T. The sum in the numerator runs over all particles with $\vec{p} \cdot \vec{n} > 0$, the sum in the denominator over all particles. The allowed range for the thrust in a centre-of-mass frame is thus between 0.5 and 1. The cuts placed on these variables are the following:

- The visible energy of the event must satisfy $E_{\text{vis}} > 0.75\sqrt{s}$ (Fig. 4.6c).

- To reject most of the $e^+e^- \to q\bar{q}(\gamma)$ background, the event thrust must be smaller than 0.88 (Fig. 4.6d) and the polar angle of the thrust axis, θ_T, has to satisfy $|\cos\theta_T| < 0.95$ (Fig. 4.6e).

- The missing momentum of the event has to be smaller than 60 GeV (Fig. 4.6f).

- Events containing electrons, muons or photons with energy larger than 20 GeV, 20 GeV or 40 GeV, respectively, are rejected (Fig. 4.7g-i).

If an event has passed the first selection cuts, it is clustered into four jets, using the Durham algorithm [59]. This algorithm follows the binary joining scheme[2]. Starting with all clusters, in every iteration the two clusters with the smallest scaled relative distance are joined into one. The scaled distance measure is given by the jet-resolution parameter y_{ij} for which the event changes from a topology with j jets into a topology with i jets

$$y_{ij} = 2 \, \frac{\min(E_i^2, E_j^2)}{E_{\text{vis}}^2}(1 - \cos\theta_{ij}) , \tag{4.4}$$

with θ_{ij} the opening angle between the momentum vectors of the two clusters. The algorithm stops when the desired number of four final jets is reached.

From the four clustered jets, two pairs are formed, corresponding to two W bosons. Of the three combinations of jet pairs, the optimal pairing of jets is chosen as the one with the smallest mass difference, $\Delta m = m_{q\bar{q},1} - m_{q\bar{q},2}$, disregarding the pairing corresponding to the smallest mass sum, $m_{q\bar{q},1} + m_{q\bar{q},2}$. This algorithm yields the correct assignment of jets to W bosons for about 70% of the selected W-pair Monte Carlo events. The two W boson candidates are reconstructed from the corresponding two jets.

The final cuts are the following:

- The jet-resolution parameter for which the event changes from a four-jet into a three-jet topology, y_{34}, must be greater than 0.0015 (Fig. 4.7j).

- Both reconstructed W boson candidates must have a mass between 40 and 120 GeV (Fig. 4.7k).

---

[2]For a compact review of the different jet clustering algorithms used at e^+e^- colliders see *e.g.* [60].
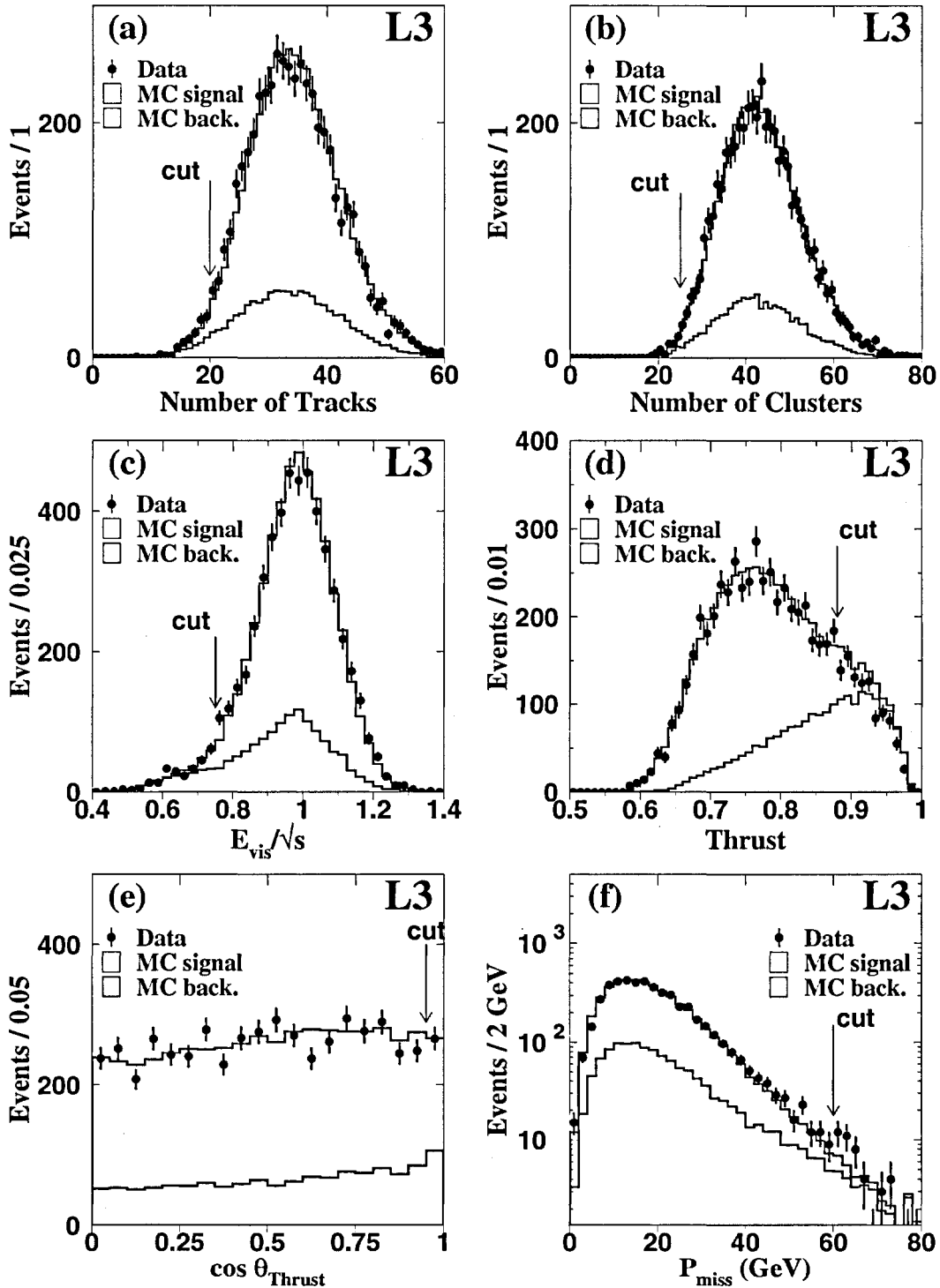
Figure 4.6: Distributions of variables used for the selection of $e^+e^- \to W^+W^- \to q_1\bar{q}_2q_3\bar{q}_4$ events: (a) number of identified tracks, (b) number of identified clusters, (c) normalised visible energy, (d) event thrust, (e) thrust angle w.r.t. beam axis, $\cos\theta_{Thrust}$, (f) missing momentum, P_{miss}. In each plot, all other selection criteria are applied. The arrows indicate the positions of the cuts. The distributions are shown for centre-of-mass energies $\sqrt{s} = 189 - 209$ GeV with an average of $\langle\sqrt{s}\rangle = 197.9$ GeV.
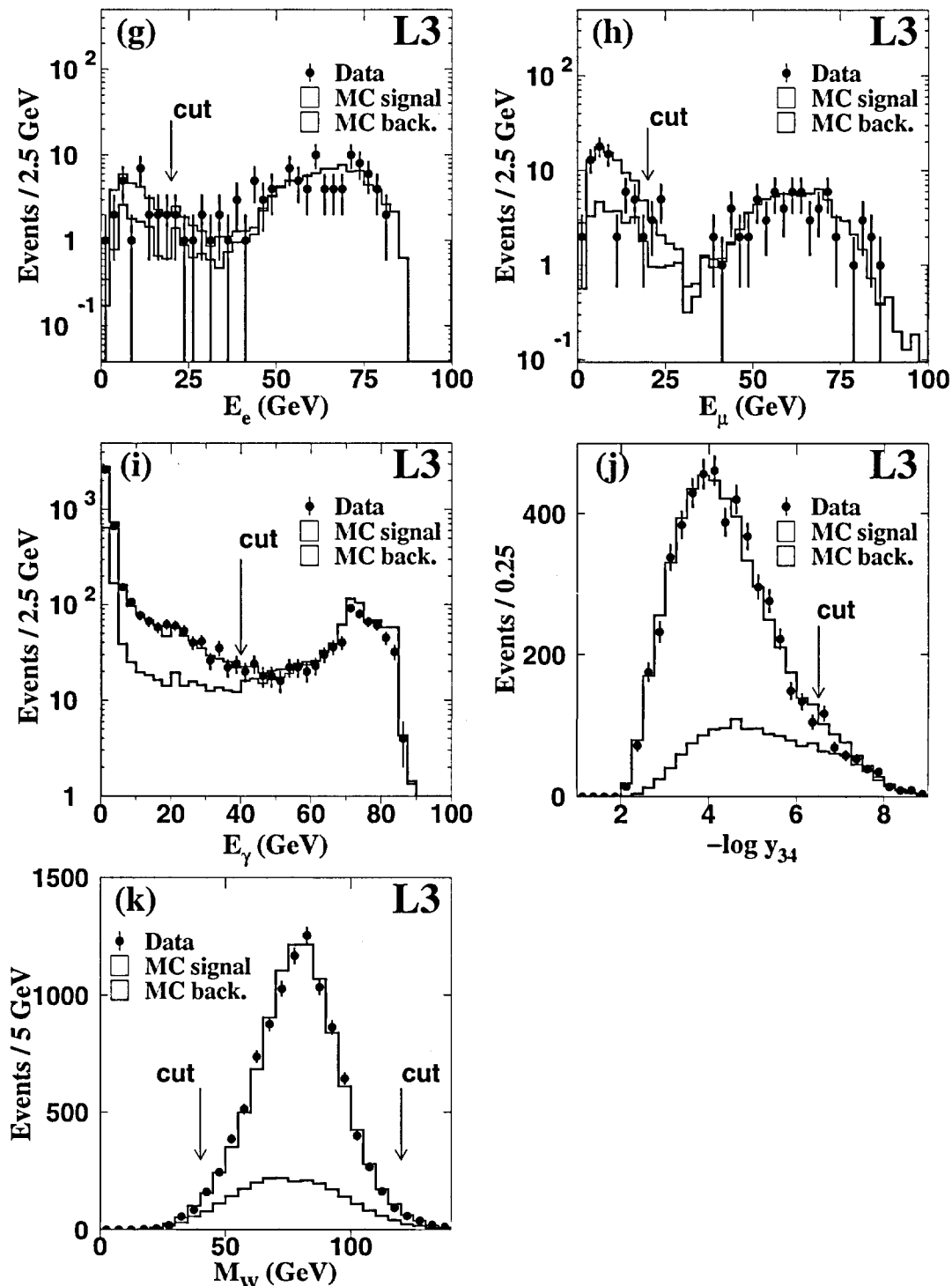
Figure 4.7: Distributions of variables used for the selection of $e^+e^- \to W^+W^- \to q_1\bar{q}_2q_3\bar{q}_4$ events: (g) energy of the most energetic electron, E_e, (h) energy of the most energetic muon, E_μ, (i) energy of the most energetic photon, E_γ, (j) jet-resolution parameter, $-\log y_{34}$, (k) reconstructed mass of the W boson. In each plot, all other selection criteria are applied. The arrows indicate the positions of the cuts. The distributions are shown for centre-of-mass energies $\sqrt{s} = 189 - 209$ GeV with an average of $\langle\sqrt{s}\rangle = 197.9$ GeV.

4.6 The Selected Data and Monte Carlo Sample

The accepted events are used to measure the W^- scattering angle and the polar decay angles of the W bosons. Fully simulated Monte Carlo events are used to determine selection efficiencies. They are also used for comparing to data, for background estimation and for the determination of the reconstruction accuracies.

In the analyses performed with the L3 detector we observe a good agreement between the Monte Carlo reconstructed observables and the ones measured with data. As a simple example we consider the mass resolution of the W boson where the distribution, especially the width of the distribution in data, is reproduced well in Monte Carlo. So it is reasonable to assume that by the comparison of the reconstructed fully simulated signal from KORALW Monte Carlo to the generated signal we obtain a good description of the reconstruction accuracy of the measured angles.

For the measured angles, the reconstruction accuracies have a nearly Gaussian distribution with non-Gaussian tails. To describe the reconstruction accuracy, a fit using multiple Gaussian functions would have to be applied. In order to give a rough estimate, a fit of these distributions to Gaussian functions in the central range is applied, such that about 90% of the events are contained in the fit. The obtained central value and standard deviation of the Gaussian is taken as a measure of the reconstruction accuracy of the considered quantity.

4.6.1 Selected $W^+W^- \rightarrow \ell\nu q_1\bar{q}_2$ Events

The number of selected $W^+W^- \rightarrow \ell\nu q_1\bar{q}_2$ candidate events are listed in Table 4.2 together with the efficiencies and purities at the particular centre-of-mass energies. The efficiency and purity varies only slightly with centre-of-mass energy.

In total, 2010 events are selected as $W^+W^- \rightarrow \ell\nu q_1\bar{q}_2$ ($\ell = e, \mu$) candidates with an efficiency of 67.8% and a purity of 96.6%. The contamination from $W^+W^- \rightarrow \tau\nu q_1\bar{q}_2$ and $e^+e^- \rightarrow q\bar{q}(\gamma)$ is 2.3% and 1.1%, respectively.

For the selected events, the W boson four-vector momenta are calculated from the lepton and neutrino four-vector momenta. All particles are boosted back into the rest frame of their parent W boson and the decay angles θ_ℓ^* and θ_q^* of the lepton and the quarks are determined.

$\langle\sqrt{s}\rangle$ [GeV]	182.7	188.6	191.6	195.5	199.5	201.8	205.9
$e\nu q_1\bar{q}_2$ candidates	82	293	59	133	110	56	355
$\mu\nu q_1\bar{q}_2$ candidates	67	255	43	110	99	59	289
total efficiency [%]	69.5	70.2	69.5	67.7	67.4	67.1	65.6
total purity [%]	96.3	96.7	97.1	96.6	96.5	96.2	96.6

Table 4.2: Average centre-of-mass energies and numbers of selected events in the $W^+W^- \rightarrow \ell\nu q_1\bar{q}_2$ channel.

The charge of the leptonically decaying W boson is given by the charge of the corresponding charged lepton.

The distributions of the electron and muon polar angles, $\cos\theta$, for data and Monte Carlo are shown in Figures 4.8 and 4.9, respectively. The agreement between data and KORALW Monte Carlo is very good.

The reconstruction accuracies for $\cos\theta_\ell^*$, obtained from Monte Carlo samples at $\sqrt{s} = 189$ GeV, are presented in Figure 4.10 for electrons and in Figure 4.11 for muons. A fit with a Gaussian as described above yields a small shift of 0.03 and a standard deviation of 0.10 for electrons. For muons, a shift of 0.05 and a standard deviation of 0.11 is obtained. The reconstruction accuracies for electrons and muons differ only slightly.

In the centre-of-mass frame of the W boson which decays hadronically, the quarks are produced back-to-back and generate hadrons via the fragmentation process. It is also possible that a gluon is radiated from one of the quarks and also generates hadrons. The hadrons are boosted along the direction of the jet initiating quark. Therefore, and taking into account the principle of energy and momentum conservation, one expects the momenta of the hadrons to point mainly in the direction of their parent quark. Thus an axis in the centre-of-mass frame of the hadronically decaying W boson which maximises the longitudinal momentum would be a good approximation for the original quark direction. Such an axis is the thrust axis introduced in Equation 4.3.

Using this approach, the angle θ_q^* is approximated by the polar angle of the thrust axis with respect to the W flight direction in the rest frame of the hadronically decaying W boson. Such an approach is also justified by the experience from the hadronic decay of the Z boson, $e^+e^- \rightarrow Z \rightarrow q\bar{q}(\gamma)$. In this decay, where the centre-of-mass frame is identical to the laboratory frame, a $(1 + \cos^2\theta)$ distribution is expected for the decay products of the Z. Using the approximation of the polar angle of the thrust axis of the hadrons with respect to the beam axis for the scattering angle of the quarks, the expected distribution can be well reproduced. For the W bosons in W-pair events the situation in the centre-of-mass frame of the W boson is similar to the hadronic Z boson decay, and thus the approximation of the quark polar angle can be applied.

The reconstruction accuracy for $|\cos\theta_q^*|$ is calculated as the difference between the $\cos\theta^*$ of the thrust axis and the generated $|\cos\theta_q^*|$. This reconstruction accuracy, obtained from Monte Carlo samples at $\sqrt{s} = 189$ GeV, is shown in Figure 4.12. A fit of this distribution with a Gaussian in the central range yields a shift of -0.01 and a standard deviation of 0.14.

The kinematics of the reconstructed W bosons is also well reproduced. Figure 4.13 shows the $\cos\Theta_{W^-}$ distributions for data and Monte Carlo. The corresponding Monte Carlo reconstruction accuracy is shown in Figure 4.14. It consists of a relatively narrow Gaussian-shaped peak and non-Gaussian tails. The fit with a Gaussian as described above yields no shift in the reconstruction accuracy and a standard deviation of 0.06.

4.6.2   Selected $W^+W^- \rightarrow q_1\bar{q}_2q_3\bar{q}_4$ Events

The numbers of $W^+W^- \rightarrow q_1\bar{q}_2q_3\bar{q}_4$ events selected by the presented criteria at different values of $\sqrt{s}$ are listed in Table 4.3, together with the efficiencies and purities. The
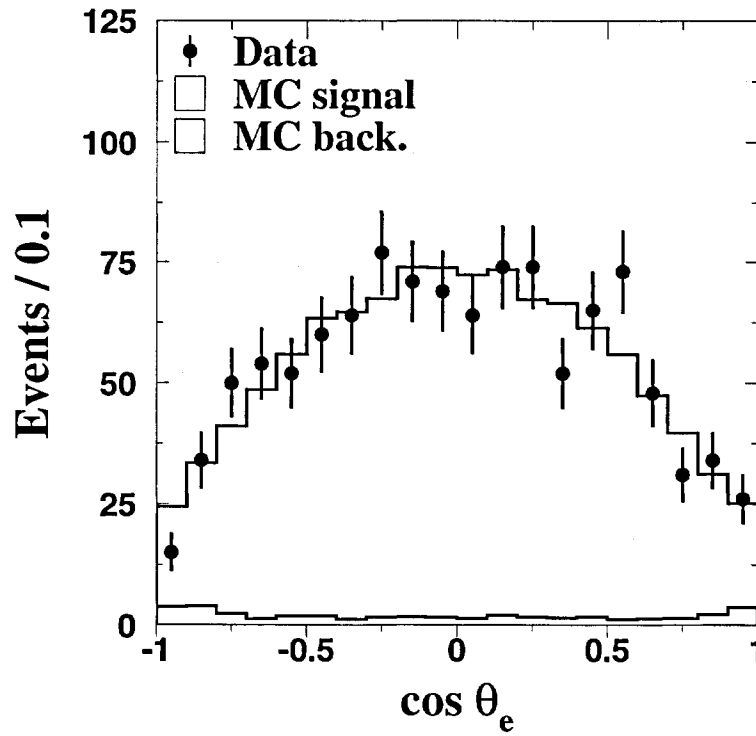
Figure 4.8: $\cos\theta$ for electrons produced in the process $e^+e^- \to W^+W^- \to e\nu q_1\bar{q}_2$.

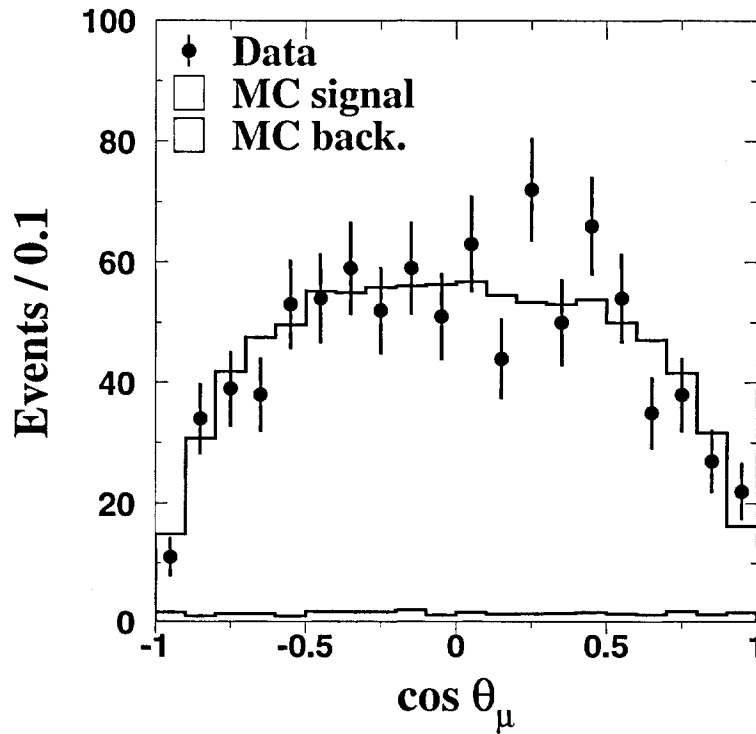**Figure 4.9:** $\cos\theta$ for muons produced in the process $e^+e^- \to W^+W^- \to \mu\nu q_1\bar{q}_2$.
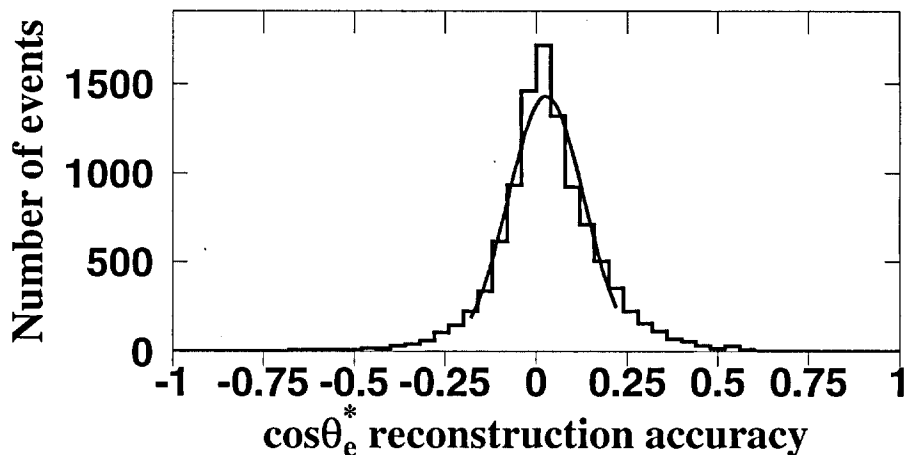
Figure 4.10: Reconstruction accuracy of $\cos\theta^*$ for electrons in the semileptonic W^+W^- decay channel at $\sqrt{s} = 189$ GeV.
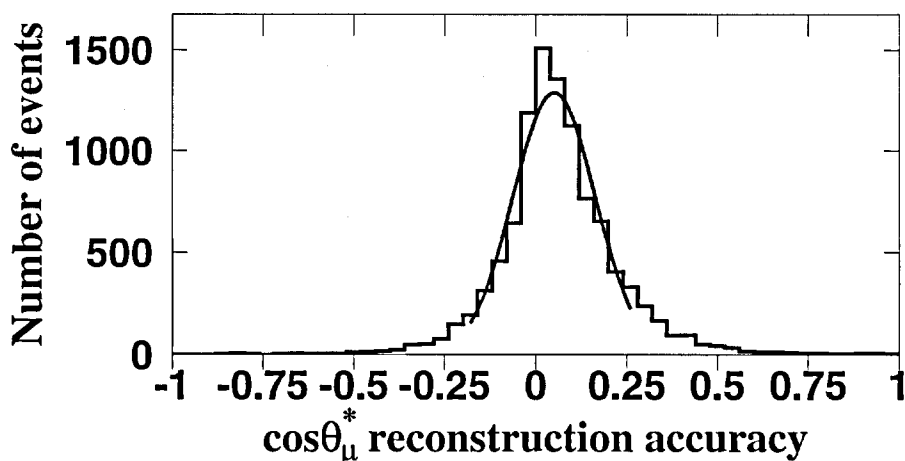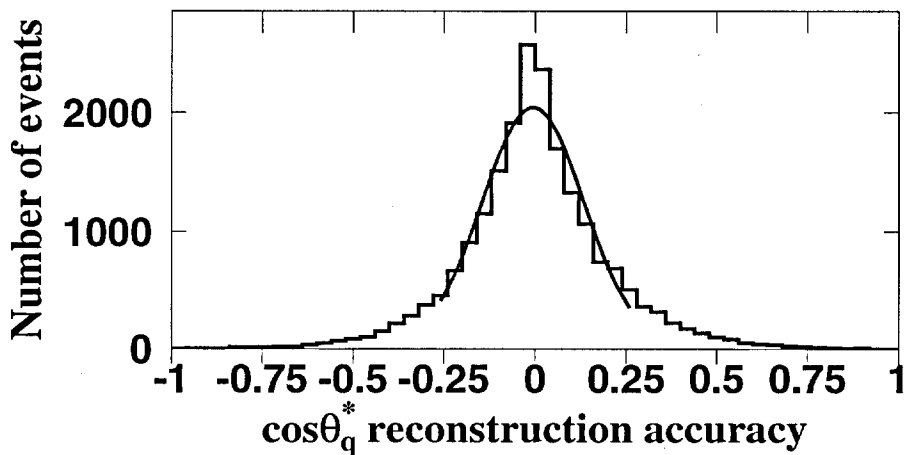
Figure 4.11: Reconstruction accuracy of $\cos\theta^*$ for muons in the semileptonic W^+W^- decay channel at $\sqrt{s} = 189$ GeV.

Figure 4.12: Reconstruction accuracy of $\cos\theta^*$ for hadrons in the semileptonic W^+W^- decay channel at $\sqrt{s} = 189$ GeV.

$\langle\sqrt{s}\rangle$ [GeV]	188.6	191.6	195.5	199.5	201.8	205.9
$e^+e^- \rightarrow q_1\bar{q}_2q_3\bar{q}_4$ candidates	1447	224	640	683	269	1656
efficiency [%]	77.8	78.2	77.6	76.5	76.5	74.4
purity [%]	74.0	74.9	75.3	75.7	73.2	78.0

Table 4.3: Average centre-of-mass energies and numbers of selected events in the $W^+W^- \rightarrow q_1\bar{q}_2q_3\bar{q}_4$ channel.

efficiency and purity vary slightly with energy.

In total, 4919 candidate events for $W^+W^- \rightarrow q_1\bar{q}_2q_3\bar{q}_4$ are selected with an efficiency of 76.3% and a purity of 75.7%. The background contamination is 18.9% from the $e^+e^- \rightarrow q\bar{q}(\gamma)$ process, 4.9% from the $e^+e^- \rightarrow ZZ$ process and 0.5% from other final states of W-pair production.

According to Monte Carlo studies, the pairing of the jets and thus the flight direction of the reconstructed W bosons is correct for about 70% of the events.

Figure 4.15 shows the distributions of the W scattering angle, $|\cos\Theta_{W^-}|$, for data and Monte Carlo, the corresponding reconstruction accuracy is shown in Figure 4.16. The fit with a Gaussian in the central region yields a small shift of 0.02 in the reconstruction accuracy and a standard deviation of 0.09. It is slightly worse than in the semileptonic channel, which has a standard deviation of 0.06, due to the reconstruction method of the quark directions.

For several reasons the selected $W^+W^- \rightarrow q_1\bar{q}_2q_3\bar{q}_4$ events are not used for the measurement of the polarisation:

- The pairing of the four jets is difficult to determine, the fraction of correctly paired jets is only about 70%. At much higher energies, due to the boost of the quarks in the W centre-of-mass frame, the jets coming from one W boson would be much closer to each other in space, and the pairing would be much easier to determine.

- Even with the correct pairing, the charge of the quarks cannot be determined correctly, and also the W boson charge cannot be assigned. As both charges are needed to distinguish between the +1 and the −1 helicity states, only helicity 0 and helicity ±1 states could be measured.

- As the charge of the W bosons cannot be assigned, only the absolute value of the W^- scattering angle can be determined. Thus only a measurement with the inclusive W boson sample would be possible.
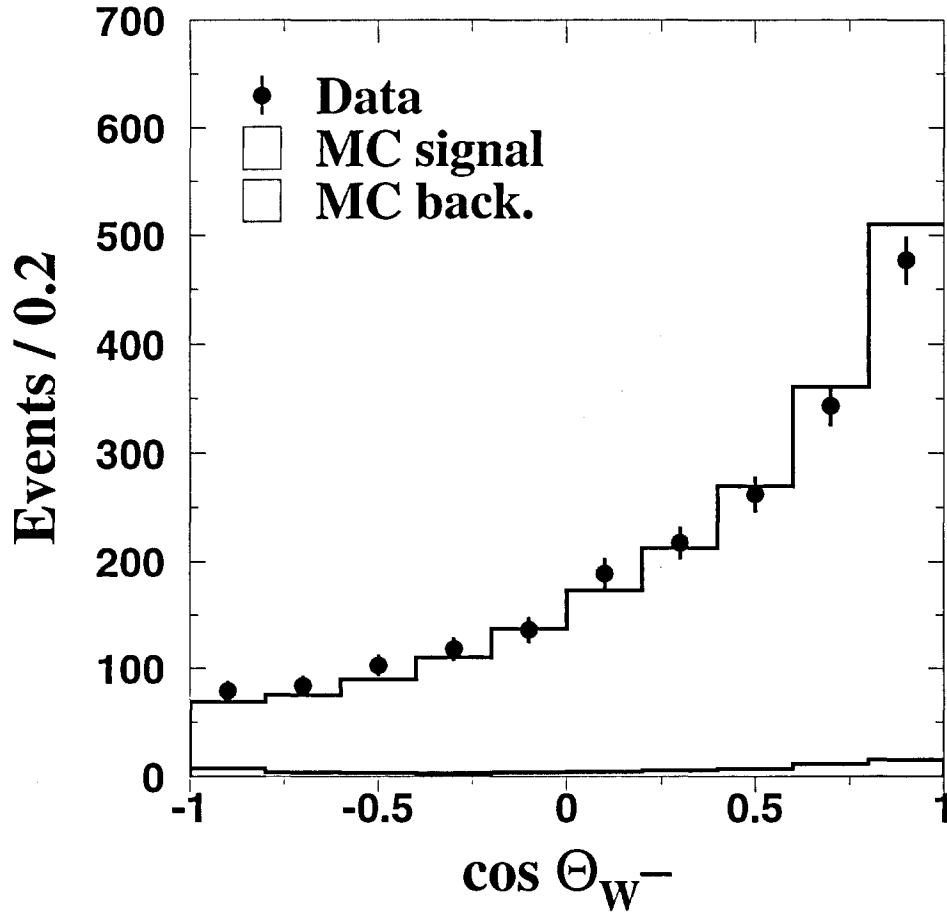
Figure 4.13: Reconstructed $\cos\Theta_{W^-}$ in the semileptonic W^+W^- decay channel.
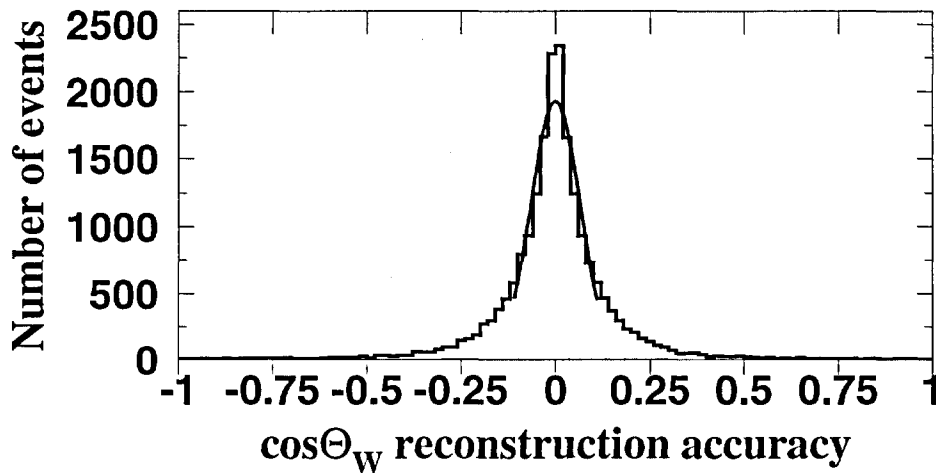

Figure 4.14: Reconstruction accuracy of $\cos\Theta_{W^-}$ in the semileptonic W^+W^- decay channel at $\sqrt{s} = 189$ GeV.
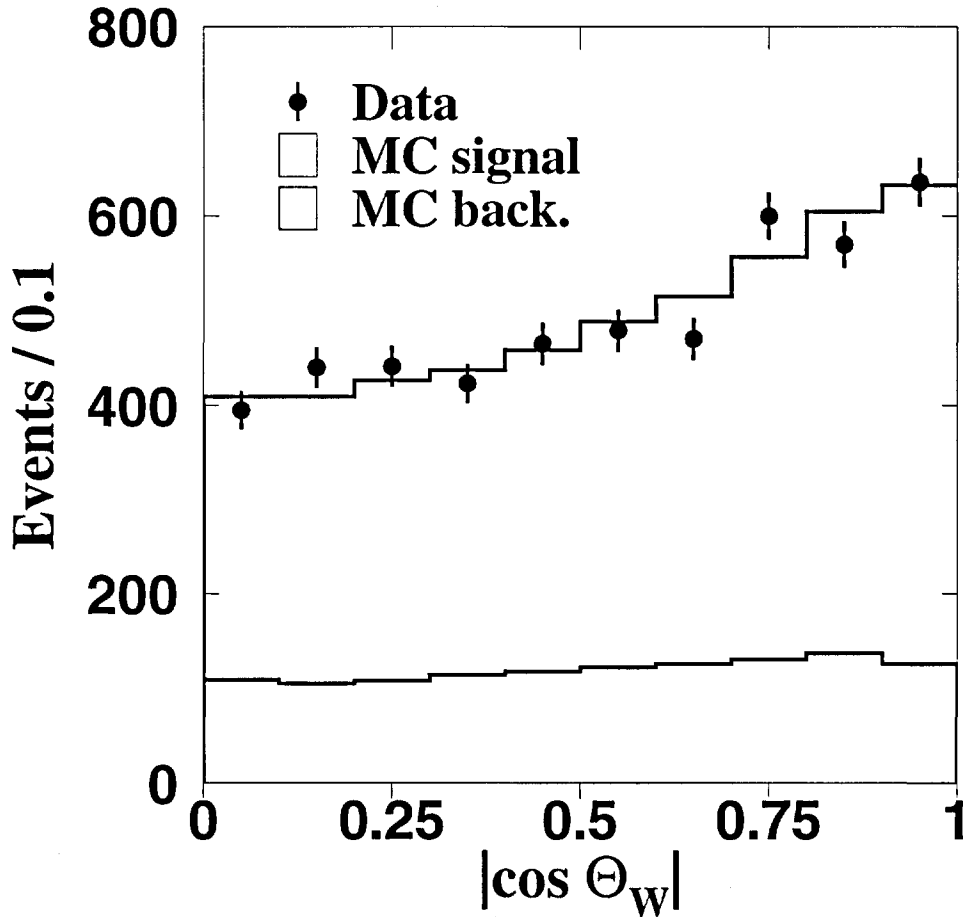
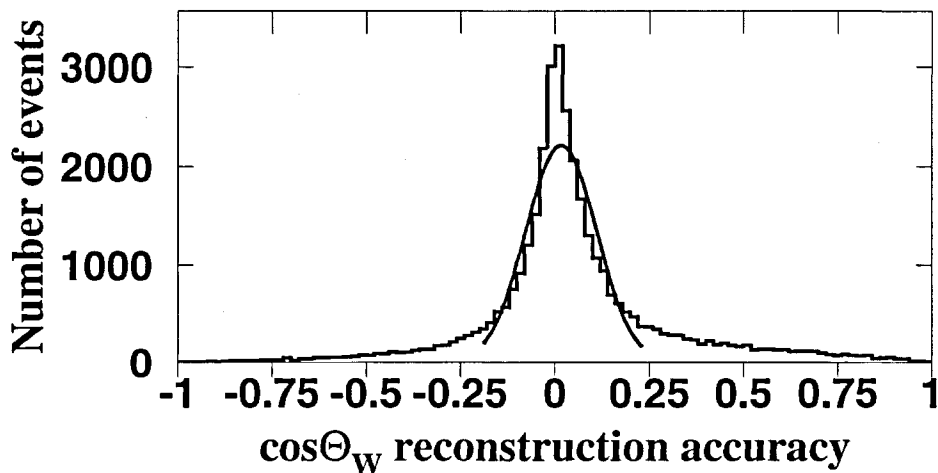**Figure 4.15:** Reconstructed $|\cos \Theta_{W^-}|$ in the fully hadronic W^+W^- decay channel.

Figure 4.16: Reconstruction accuracy of $\cos \Theta_{W^-}$ in the fully hadronic W^+W^- decay channel at $\sqrt{s} = 189$ GeV.

Chapter 5

Measurement of W Helicity Fractions

5.1 Introduction

In Chapters 1 and 2, we described in detail how W bosons with different helicities are produced in e^+e^- collisions and explained the importance of the longitudinally polarised W boson and its connection with the Higgs sector of the Standard Model. Any deviation from the Standard Model predictions would indicate a non-standard structure of the Triple Gauge Couplings ZWW and γWW in the $e^+e^- \rightarrow W^+W^-$ process.

In this Chapter, the measurement of W helicity fractions and in particular the longitudinal polarisation is described. The results for helicity fractions are compared with the Standard Model predictions. The helicity fractions are derived directly from the polar decay angles of the W bosons. The selected $W^+W^- \rightarrow e\nu q_1\bar{q}_2$ and $W^+W^- \rightarrow \mu\nu q_1\bar{q}_2$ final states are used to study the entire data sample and each final state separately. The W^- and W^+ samples are compared to test for CP invariance. The helicity fractions are measured also as a function of the W^- scattering angle, $\cos\Theta_{W^-}$. They are also expected to vary with the centre-of-mass energy, however this energy dependence is too small to be observable with the samples collected at the particular centre-of-mass energies.

Studies of systematic effects are performed with a precision adequate to the size of the measured effect. To correct for efficiency and resolution, a method appropriate to the precision of the measurement is used: applying an efficiency correction in bins of the measured quantity and correcting for additional resolution effects afterwards.

5.2 Analysis of W Helicity Fractions

The W boson, being a massive spin-1 particle, has helicity states $-1, +1$ or 0. Due to the nature of the decay of the spin-1 W boson into two spin $\frac{1}{2}$ particles, the probability that a decay particle is emitted in a certain flight direction depends on the helicity of the W boson.

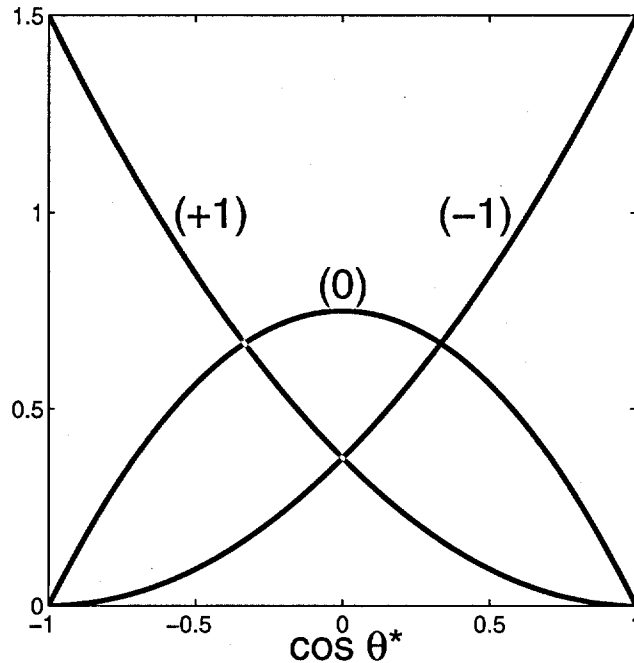For simplicity, only the case of the W^- boson is discussed in the following. Assuming

Figure 5.1: Lepton angular distribution in the W$^-$ rest frame for helicity $-1, +1$ and 0 as a function of $\cos\theta_\ell^*$.

CP invariance, all statements apply also for W$^+$ bosons with helicity $\bar{\lambda} = -\lambda$. Using this assignment, the helicity fractions for W$^-$ and W$^+$ are combined in the following unless stated otherwise.

In the leptonic decay of the W$^-$ boson in its centre-of-mass frame, W$^- \rightarrow \ell\bar{\nu}$, the anti-neutrino is right-handed, *i.e.* produced with spin $+\frac{1}{2}$ due to parity violation. Because of spin conservation, the anti-neutrino must be emitted preferably in the direction of the spin of the W$^-$ boson. For a W$^-$ with helicity $+1$, *i.e.* spin parallel to the flight direction, the anti-neutrino is emitted preferably in the forward direction, while the charged lepton is produced preferably anti-parallel to the flight direction of the W$^-$. Similarly, for a W$^-$ with helicity -1, the charged lepton is produced mainly in the flight direction of the W$^-$, and in the case of helicity 0, both anti-neutrino and charged lepton are emitted perpendicular to the flight direction of the W$^-$.

The W boson decay is a statistical process which results in an angular distribution of the decay products. If one considers the leptonically decaying W$^-$ boson and its polar decay angle, θ_ℓ^*, between the charged lepton and the W$^-$ direction in the W$^-$ rest frame, transversely polarised W$^-$ bosons with helicity $+1$ have an angular distribution $(1 - \cos\theta_\ell^*)^2$, W$^-$ bosons with helicity -1 have a distribution $(1 + \cos\theta_\ell^*)^2$. W$^-$ bosons with helicity 0 must have a $\sin^2\theta_\ell^*$ dependence. The three different shapes of the angular distributions as described by the expressions above are shown in Figure 5.1.

After we normalise the particular expressions and add them, multiplying each by a

parameter f_λ, we obtain the following differential distribution for the W-decay angle:

$$\frac{1}{N}\frac{\mathrm{d}N}{\mathrm{d}\cos\theta_\ell^*} = f_-\frac{3}{8}\left(1+\cos\theta_\ell^*\right)^2 + f_+\frac{3}{8}\left(1-\cos\theta_\ell^*\right)^2 + f_0\frac{3}{4}\sin^2\theta_\ell^*. \tag{5.1}$$

The parameter f_λ statistically describes the probability for a W$^-$ boson to have the helicity λ. Within the Standard Model, the helicity fractions f_λ are also functions of the centre-of-mass energy, $\sqrt{s}$, and the W$^-$ scattering angle, $\cos\Theta_{\mathrm{W}^-}$.

The helicity fractions f_λ can thus be obtained by a fit of the $\cos\theta_\ell^*$ distribution of the lepton coming from a W decay using the above equation. In addition, the sum of all fractions is constrained to unity[1]. This method assumes that no angular momentum states are produced in the W decay, which is a good assumption within the Standard Model.

The behaviour of the decay quarks in the hadronic decay of the W boson is in principle identical to the lepton and neutrino in the leptonic decay. Here the down-type quark takes the role of the charged lepton, hence the polar decay angle θ_d^* has an identical behaviour as θ_ℓ^*. However, the identification of the down-type quark in the hadronic decay is very difficult, and the measurement of θ_q^* in the full range $-1 \leq \cos\theta_\mathrm{q}^* \leq +1$ is essentially impossible.

For this reason we use $|\cos\theta_\mathrm{q}^*|$ for the hadronically decaying W boson with $0 \leq |\cos\theta_\mathrm{q}^*| \leq 1$. Still, the fraction of transversely polarised W bosons, $f_\pm=f_++f_-$, can be distinguished from f_0. The folded distribution becomes:

$$\frac{1}{N}\frac{\mathrm{d}N}{\mathrm{d}|\cos\theta_\mathrm{q}^*|} = f_\pm\frac{3}{4}(1+|\cos\theta_\mathrm{q}^*|^2) + f_0\frac{3}{2}(1-|\cos\theta_\mathrm{q}^*|^2). \tag{5.2}$$

The helicity fractions can thus be obtained from the event distributions, $\mathrm{d}N/\mathrm{d}\cos\theta_\ell^*$ and $\mathrm{d}N/\mathrm{d}|\cos\theta_\mathrm{q}^*|$, by fitting the Equations 5.1 and 5.2 to them.

5.2.1 Monte Carlo Generator Level Studies

We use different Monte Carlo generators to obtain predictions and to test the analysis method. First the $e^+e^- \rightarrow W^+W^-$ process is studied on generator level using the EEWW, KORALW and YFSWW Monte Carlo programs. Large samples of signal events are generated using all three Monte Carlo programs.

KORALW, a widely recognised Monte Carlo program, is used to obtain the Standard Model predictions for our measurements. EEWW uses the zero-width approximation for the W boson and assigns, in contrast to KORALW, W helicities on an event-by-event basis, hence a direct readout of the helicity fractions is possible. However, it does not include higher order radiative corrections and interference terms. The newer Monte Carlo program YFSWW is used as a cross-check, as it includes improved O(α) corrections for the process $e^+e^- \rightarrow W^+W^-$.

---

[1]The fractions are however not explicitly constrained to lie between 0 and 1, thus they could have unphysical values due to statistical fluctuations in the data.

Helicity fraction	f_-	f_+	f_0
EEWW generated	0.606	0.161	0.233
EEWW fit	0.606 ± 0.003	0.159 ± 0.002	0.236 ± 0.003
KORALW fit	0.596 ± 0.003	0.167 ± 0.002	0.238 ± 0.003
YFSWW fit	0.590 ± 0.003	0.159 ± 0.002	0.252 ± 0.004

Table 5.1: Helicity fractions for the luminosity combined samples for centre-of-mass energies $\sqrt{s} = 189 - 209$ GeV, obtained directly from EEWW and from fits to the generated decay distributions obtained using EEWW, KORALW and YFSWW. The errors reflect Monte Carlo statistics and are a factor of 10 smaller than the expected error on the data.

Helicity fraction	f_-	f_+	f_0
183 GeV	0.532 ± 0.004	0.198 ± 0.003	0.270 ± 0.004
189 GeV	0.561 ± 0.006	0.177 ± 0.005	0.262 ± 0.006
192 GeV	0.568 ± 0.006	0.182 ± 0.005	0.250 ± 0.006
196 GeV	0.600 ± 0.006	0.169 ± 0.005	0.231 ± 0.006
200 GeV	0.605 ± 0.006	0.167 ± 0.004	0.228 ± 0.007
202 GeV	0.608 ± 0.006	0.156 ± 0.004	0.235 ± 0.006
206 GeV	0.620 ± 0.006	0.157 ± 0.004	0.224 ± 0.006
183 - 209 GeV	0.590 ± 0.003	0.169 ± 0.002	0.241 ± 0.003

Table 5.2: Helicity fractions for the particular centre-of-mass energies obtained from a fit to the distributions from KORALW and their luminosity weighted average. The errors reflect Monte Carlo statistics.

The helicity fractions are obtained from the Monte Carlo samples by fitting the normalised generated decay angular distributions for each value of $\sqrt{s}$ using Equation 5.1. From the fit, the helicity fractions f_- and f_0 are obtained, while the fraction f_+ follows by constraining the sum of all three parameters to unity.

The helicity fractions for the luminosity combined sample for centre-of-mass energies $\sqrt{s} = 189 - 209$ GeV obtained from EEWW from the direct assignment of the helicity, together with the numbers obtained from a fit to the generated distributions from EEWW, KORALW and YFSWW, are shown in Table 5.1. The EEWW fractions obtained from a fit to the distributions are in agreement with the fractions read out directly. The fractions obtained from KORALW and YFSWW are in agreement with the fractions from EEWW within the statistical errors. KORALW and YFSWW predictions are in agreement, the differences of about 1.5% are smaller than the expected statistical errors of about 3%. This shows also that for all practical purposes, the effects from higher order processes are essentially negligible, and the Born level formulæ 5.1 and 5.2 are an excellent approximation.

Table 5.2 shows the numbers obtained from a fit at the particular centre-of-mass energies using KORALW. The dependence of the helicity fractions on the centre-of-mass
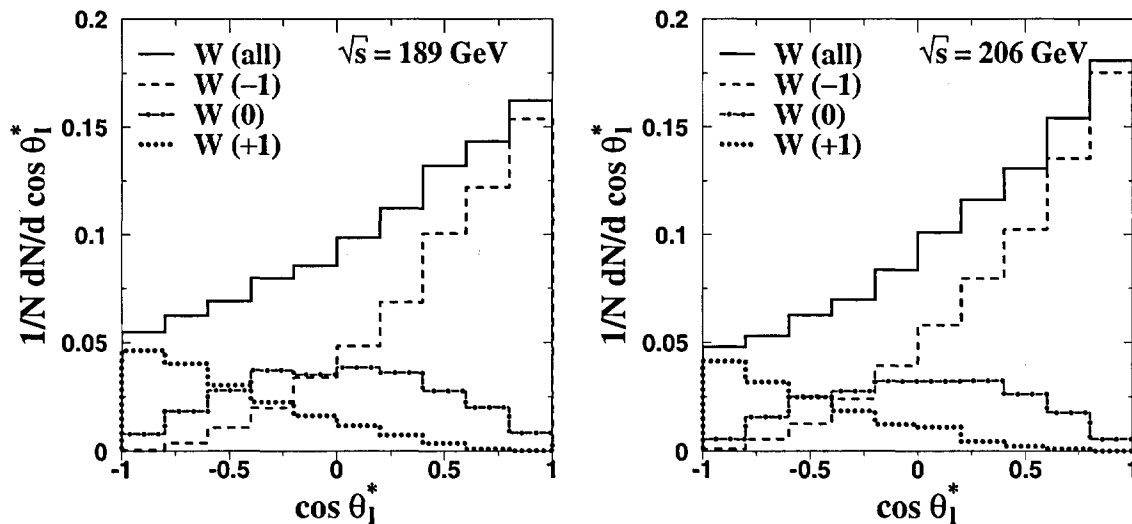
Figure 5.2: Normalised generated $\cos\theta_\ell^*$ distributions at $\sqrt{s}$ = 189 and 206 GeV using EEWW Monte Carlo. The particular distributions for the helicity states are also shown. The two distributions demonstrate the energy dependence of the helicity composition. For the higher energy, also the fraction of helicity states -1 is generally higher.

energy is unfortunately too small to be measurable with the available data sample. To observe an energy dependence, one would need about an order of magnitude more data. *E.g.* to see a difference of three standard deviations for the fraction f_- between $\sqrt{s}$ = 189 GeV and 206 GeV, the two high statistics bins, one would need a factor of 20 more data.

As an example, Figure 5.2 shows the generated $\cos\theta_\ell^*$ distributions at $\sqrt{s}$ = 189 and 206 GeV using EEWW, together with the particular contributions from the helicity states. The distributions at the particular centre-of-mass energies are quite similar, however we can observe a small increase in the helicity -1 states at higher energies.

Using KORALW Monte Carlo, the Standard Model expectations for f_-, f_+ and f_0, obtained by a luminosity weighted average over the different energies, are 0.590, 0.169 and 0.241, respectively.

5.2.2 Reconstruction and Detector Effects

The reconstructed distributions are obtained using fully simulated Monte Carlo events and all selection cuts. Figure 5.3 shows as an example three different distributions, obtained with the EEWW Monte Carlo program at $\sqrt{s}$ = 206 GeV. The full line is the distribution of the generated values of $\cos\theta_\ell^*$ for all Monte Carlo events, the dashed line is the distribution of generated $\cos\theta_\ell^*$ only for the selected events, and the data points represent the distribution of the reconstructed $\cos\theta_\ell^*$ for the selected events. From the comparison of the first two distributions one sees that, as a result of the detector acceptance and the selection mainly events in the forward region are missing. The comparison
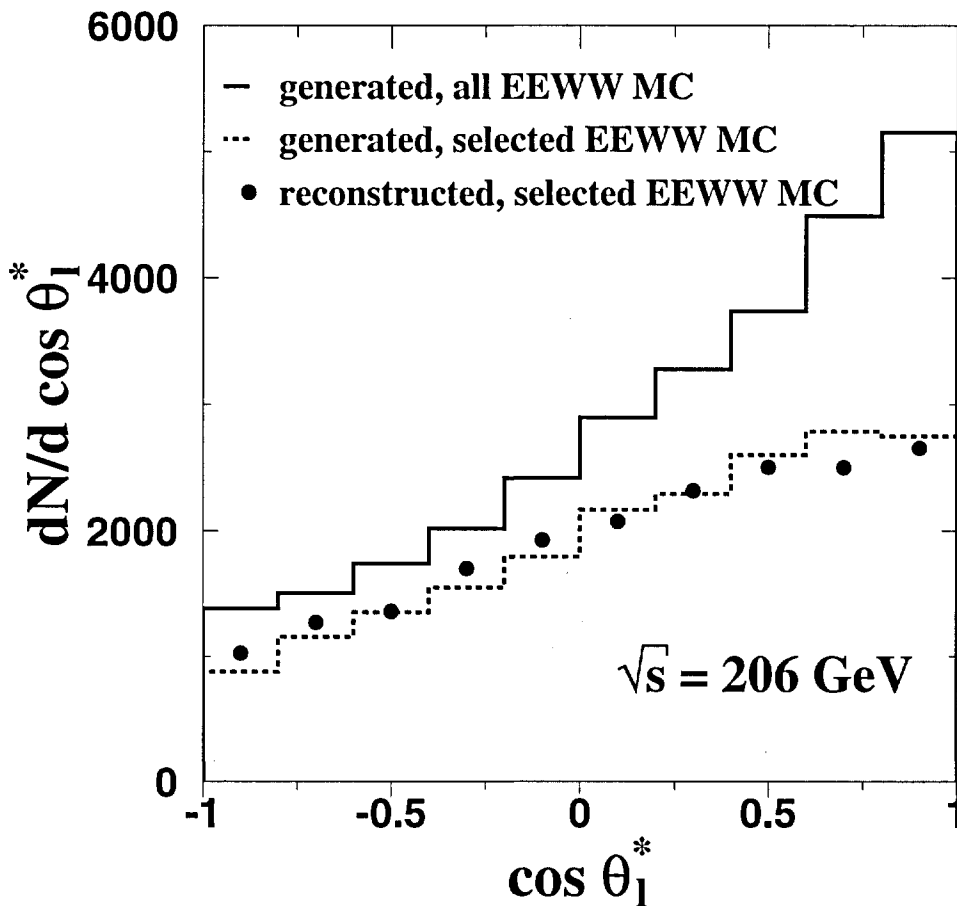
Figure 5.3: Unnormalised $\cos \theta_\ell^*$ distributions obtained with EEWW at $\sqrt{s} = 206$ GeV. The generated values for all events are plotted with a full line, the generated values for the selected events are plotted with a dashed line. The data points describe the reconstructed values for the selected events.

between the generated and the reconstructed distribution of the selected events shows the effects of the resolution of the detector and thus bin migration.

The efficiency in terms of an observable describes the ratio of the number of selected events to the total number of events. As can be seen in Figure 5.3, the shapes of the generated distribution for all events and the reconstructed distribution for the selected events differ considerably, indicating that the efficiency depends on the observable $\cos \theta_\ell^*$ itself.

Additionally, the data distributions contain a small background. This background, which cannot be removed entirely by cuts, has to be subtracted on a statistical basis using Monte Carlo. This background is very small, corresponding to about 3% of the selected candidates. As an example, Figures 5.4 and 5.5 show the raw reconstructed $\cos \theta_\ell^*$ and $|\cos \theta_q^*|$ distributions for data and Monte Carlo. The Monte Carlo distributions
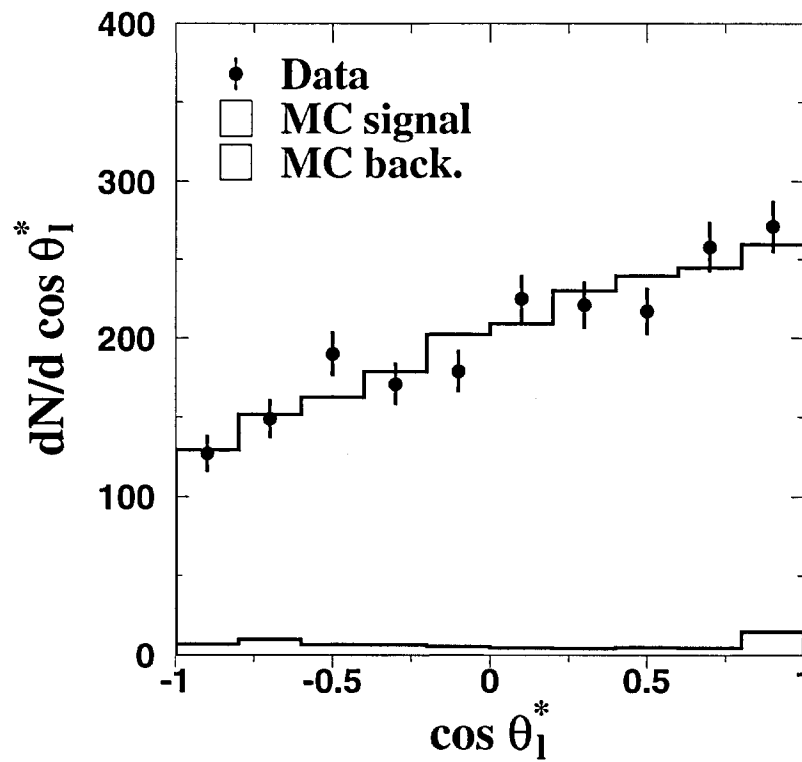
Figure 5.4: Unnormalised and uncorrected $\cos \theta_\ell^*$ distribution for data and Monte Carlo signal and background.
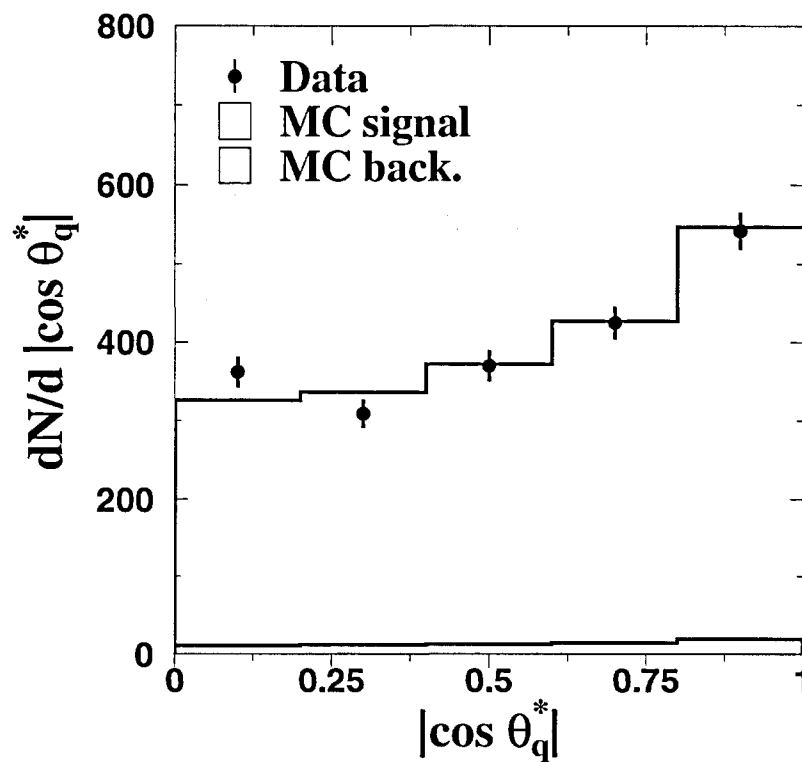

Figure 5.5: Unnormalised and uncorrected $|\cos \theta_q^*|$ distribution for data and Monte Carlo signal and background.

consist of the signal events and the simulated background events. From the observed good agreement between the data and Monte Carlo distributions, one sees already that data and Standard Model are in agreement.

5.2.3   Correction for Background, Efficiency and Migration Effects

Background corrections are determined for each centre-of-mass energy bin using background Monte Carlo events which passed the selection. The Monte Carlo distributions are normalised using the background cross-sections and the collected luminosity. The background is subtracted accordingly from the raw data distributions.

The efficiency correction function is determined for each centre-of-mass energy bin as the ratio of reconstructed to generated signal KORALW Monte Carlo distributions. The background corrected data distributions are divided by this efficiency correction function. This method of efficiency correction takes selection and effects from initial state radiation as simulated by the KORALW Monte Carlo into account. Migration effects, which are discussed in Section 4.6, are thus also taken into account.

The corrected decay angle distributions at the different centre-of-mass energies are combined into single distributions for leptonic and hadronic decays. These distributions are normalised and a binned χ^2 fit to the functions in Equations 5.1 and 5.2 is performed, using f_- and f_0 as the fit parameters. The fraction f_+ is obtained by constraining the sum of all three parameters to unity.

The efficiency correction function depends slightly on the helicity fractions, thus a small additional correction of the fit results for this bias is necessary. The bias correction, *i.e.* the correction for migration effects depending on the helicity fractions, is performed on the fractions and their errors obtained from the fit. This correction depends on several additional factors. The bias has been studied in detail using large samples of fully simulated and reconstructed EEWW Monte Carlo events at different centre-of-mass energies.

Correction functions are determined by varying the generated W helicity fractions over a large range. For example, purely longitudinally polarised leptonically decaying W bosons at $\sqrt{s} = 206$ GeV would be measured to have a helicity composition: $f_0 = 0.95, f_- = 0.04$ and $f_+ = 0.01$. For a centre-of-mass energy of $\sqrt{s} = 189$ GeV, purely longitudinally polarised leptonically decaying W bosons would be measured to have a helicity composition: $f_0 = 0.92, f_- = 0.03$ and $f_+ = 0.05$. To account for the dependence on the centre-of-mass energy, correction functions are determined using an EEWW Monte Carlo sample which includes all energy bins, normalised using the measured luminosities.

Figure 5.6 shows an example of the bias correction function for f_0 for leptonic W boson decays. For this bias correction function, the helicity fraction f_+ is kept at its measured value, $f_+ = 0.177$. The measured fraction f_0 is also shown, together with its statistical error, $f_{0,\text{reco}} = 0.216 \pm 0.033$. The corrected fraction f_0 and the corrected statistical error are indicated in the Figure, $f_{0,\text{gen}} = 0.221 \pm 0.036$.

The dependence of the correction functions for one particular helicity fraction on the remaining two helicity fractions has been studied in detail. Figure 5.7 shows as an
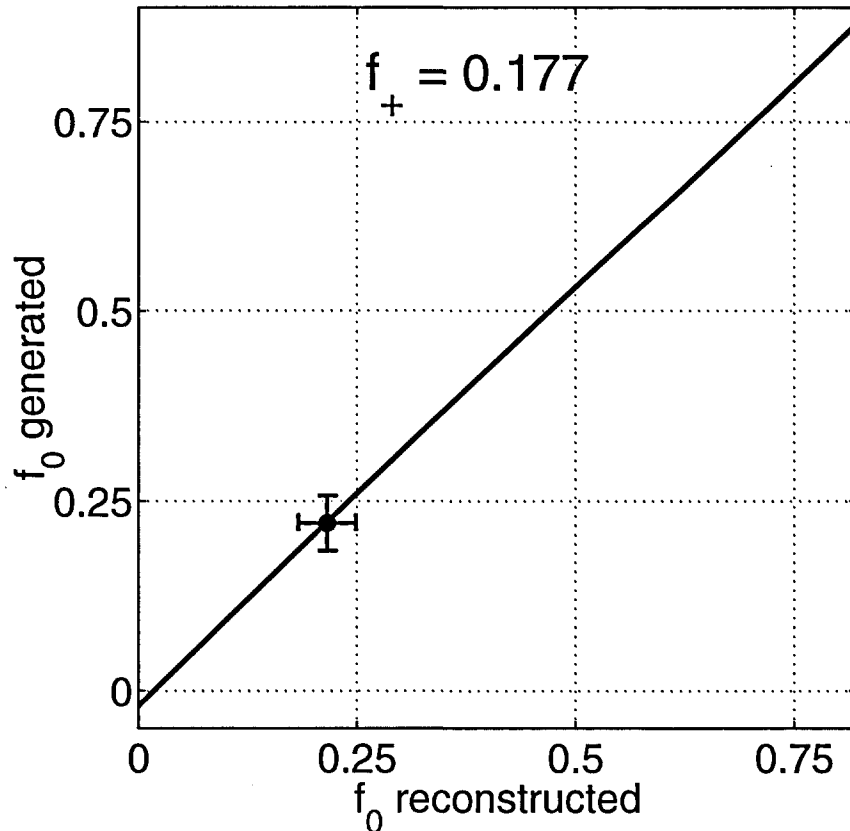
Figure 5.6: Bias correction function for f_0, for a reconstructed $f_+ = 0.177$. The data point indicates the measured fraction with its error, and the generated fraction with its error. The latter ones are derived from the shown function.

example the generated fraction f_0 as a function of the reconstructed fraction f_-, obtained using EEWW Monte Carlo. For this function, the reconstructed fraction f_0 is kept at its measured value, $f_{0,\mathrm{reco}} = 0.216$. The reconstructed fraction f_- and the generated fraction f_0 are also shown with their statistical errors.

One sees that the statistical error on the generated fraction f_0 (indicated in the Figure) is of the order of the whole variation of the bias correction function with the other two fractions. Thus the uncertainty on the generated fraction f_0 which is due to the statistical error on the reconstructed fraction f_- (indicated in the Figure) is negligible. Therefore this uncertainty is not taken into account for the determination of the total error of the corrected fraction f_0. The same behaviour is observed for all the other helicity fractions.

In order to avoid introducing another additional bias and thus enlarging the systematic uncertainty on the measured fractions, the other two fractions are used for the correction of the third fraction. If the ratio of two helicity fractions is constant the bias correction function of the third fraction is linear to a very good approximation. For the correction of f_0 in the hadronic W decay, the ratio f_-/f_+ is taken from the measurement in the leptonic W decay, as only the sum of f_+ and f_- is known from hadronic decays.
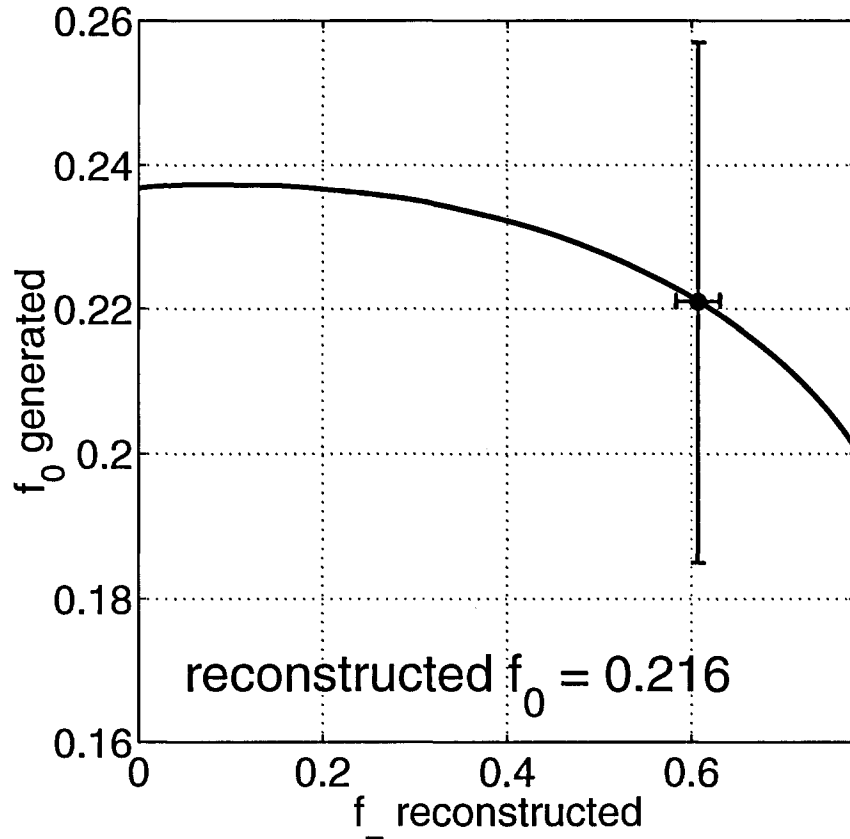
Figure 5.7: Generated fraction f_0 as a function of the reconstructed fraction f_-. The reconstructed fraction f_0 is kept at a value of 0.216. The data point indicates the measured fraction together with the errors.

The size of the correction is not negligible compared to the statistical error. As an example, the effect of the bias correction on the measured f_0 fraction is a change from 0.216 ± 0.033 to 0.221 ± 0.036 for leptonic decays, and from 0.259 ± 0.034 to 0.215 ± 0.042 for hadronic decays.

Bias correction functions are determined for the analysis of the complete data sample, separately for the W^+ and W^- events and as a function of the W^- scattering angle.

5.3   Systematic Effects

The systematic uncertainties on the results presented in chapter 5.4 are discussed in the following. In principle, the systematic error comes from the imperfect modelling of the detector and the simulation. As an example, Table 5.3 summarises the systematic effects on f_0. The largest uncertainties arise from selection criteria and for hadronic decays also from binning effects. All other effects are much smaller.

The total systematic uncertainties for the leptonically decaying W bosons are about

	W→$\ell\nu$	W→hadrons
Selection	0.013	0.024
Binning effects	0.007	0.029
Bias correction	0.006	0.011
Four fermion contamination	0.005	0.001
Background correction	0.004	0.001
Efficiency correction	< 0.001	< 0.001
Total	0.017	0.039
Statistical error	0.036	0.042

Table 5.3: Systematic uncertainties on the measurement of f_0 for leptonic and hadronic W decays. For comparison, the statistical error is also given.

half as large as the statistical error. For hadronically decaying W bosons, the systematic uncertainties are similar to the statistical error of the data sample. The combined systematic uncertainties for leptonic and hadronic decays are calculated by adding the systematic uncertainties from the particular sources in quadrature. The total systematic uncertainty for f_0, combining leptonic and hadronic decays in quadrature, is 0.016, still much smaller than the total statistical error of 0.029.

The selection can give a shift of the measured values if there is some migration between bins in the region of the cuts which is not described correctly by the detector simulation. To study this possibility, the selection cuts are varied over a small range around the actual value. The corresponding variation of the helicity fractions is taken as systematics.

Uncertainties on the corrections for bias and efficiency are determined with large Monte Carlo samples. The analysis is redone varying the bias and efficiency corrections within one standard deviation on both sides, and the difference is retained as systematics.

Background correction uncertainties can come from insufficient knowledge of the cross-sections or from the available Monte Carlo statistics. For the studied semileptonic channel, with its high purity, uncertainties on the cross-section of background processes do not play a significant role. The analysis is repeated varying the background levels according to Monte Carlo statistics for all background processes. The average absolute difference from the results using the standard background levels is retained as systematics.

Effects of binning of the considered quantities are studied by repeating all fits with one bin more or one bin less in the decay angle distributions. The average absolute difference from the results using the standard binning is retained as systematics.

The possible contamination from the non double-resonant four-fermion final states is studied by using the EXCALIBUR Monte Carlo. Two samples of 100000 e$\nu q_1 \bar{q}_2$ events each are generated using EXCALIBUR Monte Carlo, one containing only CC03 processes and the other one containing all four-fermion final state processes mediated by at least one W boson (CC20). The analysis is redone using both samples, yielding only very small differences in the fractions, which are at the level of the statistical error of the generated events. These differences are retained as systematics.

5.4 Results

5.4.1 Inclusive Helicity Fractions

The fits to the decay angle distributions for leptonic and hadronic W decays for the entire data sample are shown in Figures 5.8 and 5.9, respectively. The data are well described only if all three W helicity states are used. Fits omitting the helicity 0 state fail to describe the data.

For leptonic W decays, the χ^2 increases from 12.7 for eight degrees of freedom if all helicity states are included to 56.2 for nine degrees of freedom if only the helicities +1 and -1 are used in the fit. This corresponds to a probability of 0.123 if all helicity states are used comparing to a probability of $7.19 \cdot 10^{-9}$ if helicity 0 is omitted. For hadronic W decays, the χ^2 increases from 6.6 for four degrees of freedom if all helicity states are included to 59.1 for four degrees of freedom if only the helicities ± 1 are used. This means a change in the probability from 0.159 to $4.48 \cdot 10^{-12}$ when the helicity 0 state is omitted. This shows that the helicity 0 state of the W boson exists in the reaction $e^+e^- \rightarrow W^+W^-$ at $\sqrt{s} = 183 - 209$ GeV.

The measured fractions of the W helicity states in data, at an average centre-of-mass energy $\sqrt{s} = 196.7$ GeV, are presented together with the Standard Model expectation in Tables 5.4 and 5.5. Table 5.6 shows the combined fractions, where the fraction f_0 is obtained from leptonic and hadronic decays using the method of least squares. For +1 and -1 helicity states, the results from the leptonic decays are scaled such that their sum equals $(1 - f_0)$. The parameters f_- and f_0 derived from the fit are about 90% anti-correlated.

The measured W helicity fractions are in agreement with the Standard Model expectations for the leptonic and hadronic decays, as well as for the combined sample. In particular, the fraction of longitudinally polarised W bosons is measured as $f_0 = 0.218 \pm 0.027 \pm 0.016$, in good agreement with the KORALW prediction of 0.241 ± 0.003. Including systematic uncertainties, the longitudinal polarisation is observed with a significance of seven standard deviations.

A test has been performed to check for effects of additional angular momentum states in the W decay. The fit to the Equations 5.1 and 5.2 has been performed without the constraint of unity for the sum of the three helicities. The results of these fits are in excellent agreement with the standard fit method, the differences being negligible compared to the statistical error. The obtained statistical errors of the helicity fractions are also in excellent agreement between the two fit methods.

Within the Standard Model, CP symmetry is conserved in the reaction $e^+e^- \rightarrow W^+W^-$ and the helicity fractions f_+, f_- and f_0 for the W^+ are expected to be identical to the fractions f_-, f_+ and f_0, for the W^-, respectively. CP invariance is tested by measuring the helicity fractions for W^+ and W^- separately. The charge of the W bosons is obtained from the charge of the lepton. In total, 1020 $W^+ \rightarrow \ell^+ \nu$, and 990 $W^- \rightarrow \ell^- \bar{\nu}$ events are selected. Results of separate fits for the W^- helicity fractions are given in Tables 5.4, 5.5 and 5.6 for leptonic, hadronic and combined fits. Good agreement is found, consistent with CP invariance.
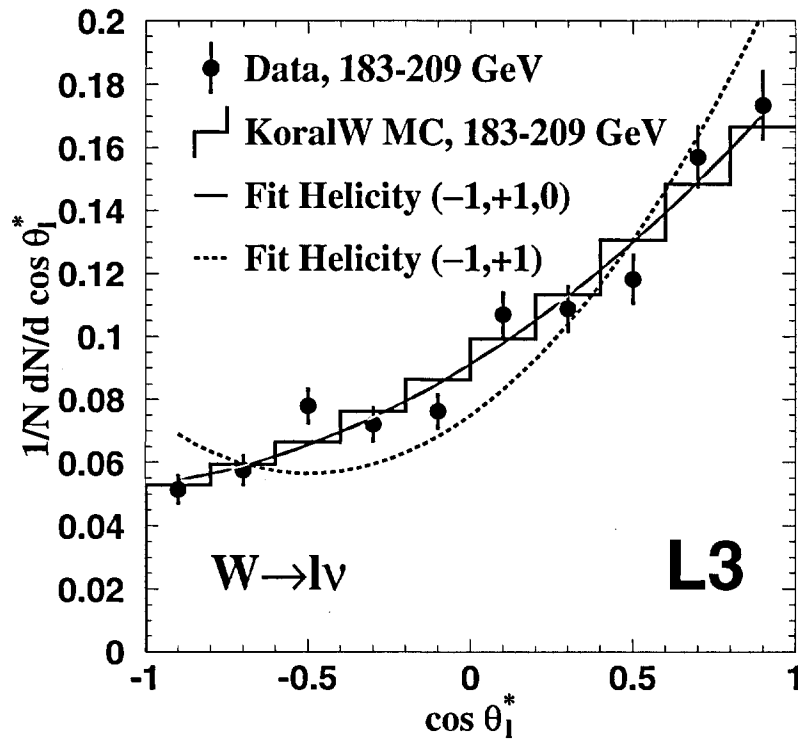
Figure 5.8: Corrected decay angle distributions for leptonic W decays at $\sqrt{s} = 183 - 209$ GeV. Fit results for the different W helicity hypotheses are also shown.
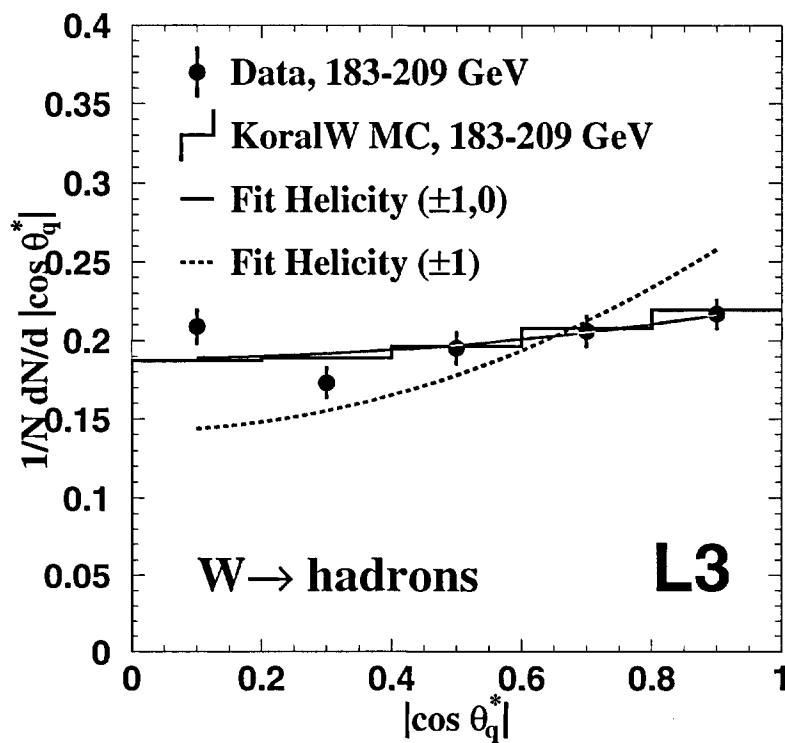

Figure 5.9: Corrected decay angle distributions for hadronic W decays at $\sqrt{s} = 183 - 209$ GeV. Fit results for the different W helicity hypotheses are also shown.

Sample	f_-	f_+	f_0
$W^- \to \ell^- \bar{\nu}$ Data	$0.559 \pm 0.038 \pm 0.016$	$0.201 \pm 0.026 \pm 0.015$	$0.240 \pm 0.051 \pm 0.017$
$W^+ \to \ell^+ \nu$ Data	$0.625 \pm 0.037 \pm 0.016$	$0.179 \pm 0.023 \pm 0.015$	$0.196 \pm 0.050 \pm 0.017$
$W^\pm \to e^\pm \nu$ Data	$0.598 \pm 0.036 \pm 0.016$	$0.187 \pm 0.023 \pm 0.015$	$0.215 \pm 0.049 \pm 0.017$
$W^\pm \to \mu^\pm \nu$ Data	$0.573 \pm 0.039 \pm 0.016$	$0.185 \pm 0.025 \pm 0.015$	$0.242 \pm 0.052 \pm 0.017$
$W^\pm \to \ell^\pm \nu$ Data	$0.589 \pm 0.027 \pm 0.016$	$0.189 \pm 0.017 \pm 0.015$	$0.221 \pm 0.036 \pm 0.017$
Monte Carlo	0.592 ± 0.003	0.170 ± 0.002	0.238 ± 0.004

Table 5.4: W^- helicity fractions for the leptonic decays for the combined data sample. All the helicities are converted to W^- parameters using CP invariance. The first uncertainty is statistical, the second systematic. The corresponding helicity fractions in the Standard Model as implemented in the KORALW Monte Carlo program are also given with their statistical uncertainties.

Sample	$f_\pm$	f_0
$W^- \to$ hadrons Data	$0.750 \pm 0.056 \pm 0.039$	$0.250 \pm 0.056 \pm 0.039$
$W^+ \to$ hadrons Data	$0.833 \pm 0.062 \pm 0.039$	$0.167 \pm 0.062 \pm 0.039$
$W^\pm \to$ hadrons Data ($e\nu q_1 \bar{q}_2$ events)	$0.917 \pm 0.058 \pm 0.039$	$0.083 \pm 0.058 \pm 0.039$
$W^\pm \to$ hadrons Data ($\mu\nu q_1 \bar{q}_2$ events)	$0.655 \pm 0.059 \pm 0.039$	$0.345 \pm 0.058 \pm 0.039$
$W^\pm \to$ hadrons Data	$0.785 \pm 0.042 \pm 0.039$	$0.215 \pm 0.042 \pm 0.039$
Monte Carlo	0.757 ± 0.004	0.243 ± 0.004

Table 5.5: W^- helicity fractions for the hadronic decays for the combined data sample. All the helicities are converted to W^- parameters using CP invariance. The first uncertainty is statistical, the second systematic. The corresponding helicity fractions in the Standard Model as implemented in the KORALW Monte Carlo program are also given with their statistical uncertainties.

Sample	f_-	f_+	f_0
W^- Data	$0.555 \pm 0.037 \pm 0.016$	$0.200 \pm 0.026 \pm 0.015$	$0.245 \pm 0.038 \pm 0.016$
W^+ Data	$0.634 \pm 0.038 \pm 0.016$	$0.181 \pm 0.024 \pm 0.015$	$0.185 \pm 0.039 \pm 0.016$
$W^\pm$ Data ($e\nu q_1 \bar{q}_2$ events)	$0.640 \pm 0.039 \pm 0.016$	$0.200 \pm 0.025 \pm 0.015$	$0.160 \pm 0.037 \pm 0.016$
$W^\pm$ Data ($\mu\nu q_1 \bar{q}_2$ events)	$0.538 \pm 0.037 \pm 0.016$	$0.173 \pm 0.024 \pm 0.015$	$0.289 \pm 0.039 \pm 0.016$
$W^\pm$ Data	$0.592 \pm 0.027 \pm 0.016$	$0.190 \pm 0.017 \pm 0.015$	$0.218 \pm 0.027 \pm 0.016$
Monte Carlo	0.590 ± 0.003	0.169 ± 0.002	0.241 ± 0.003

Table 5.6: W^- helicity fractions, measured combining leptonic and hadronic decays. All the helicities are converted to W^- parameters using CP invariance. The first uncertainty is statistical, the second systematic. The corresponding helicity fractions in the Standard Model as implemented in the KORALW Monte Carlo program are also given with their statistical uncertainties.

WW → eνqq
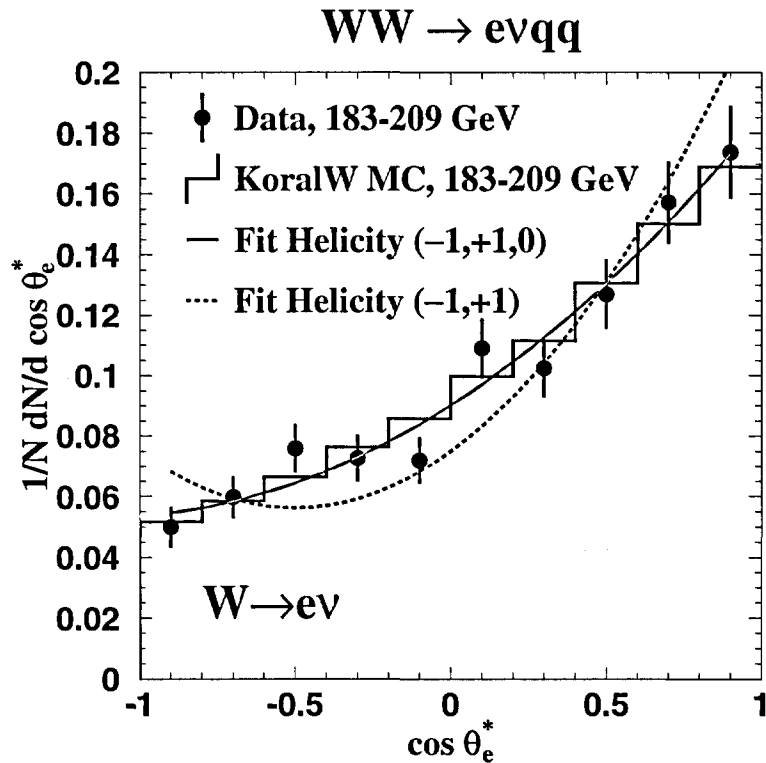
Figure 5.10: Corrected decay angle distributions for leptonic W decays at $\sqrt{s} = 183 - 209$ GeV for the $W^+W^- \rightarrow e\nu q_1\bar{q}_2$ process. Fit results for the different W helicity hypotheses are also shown.
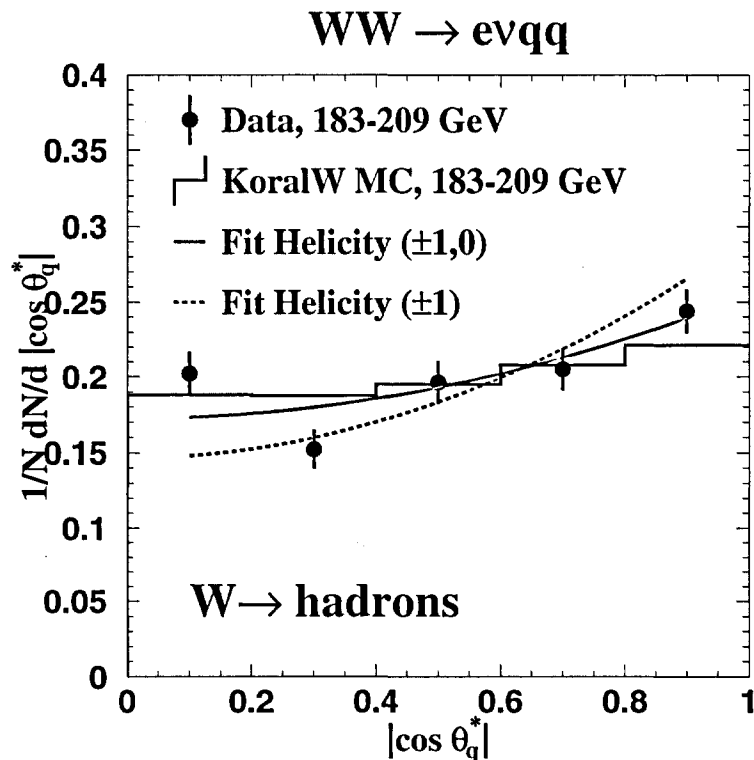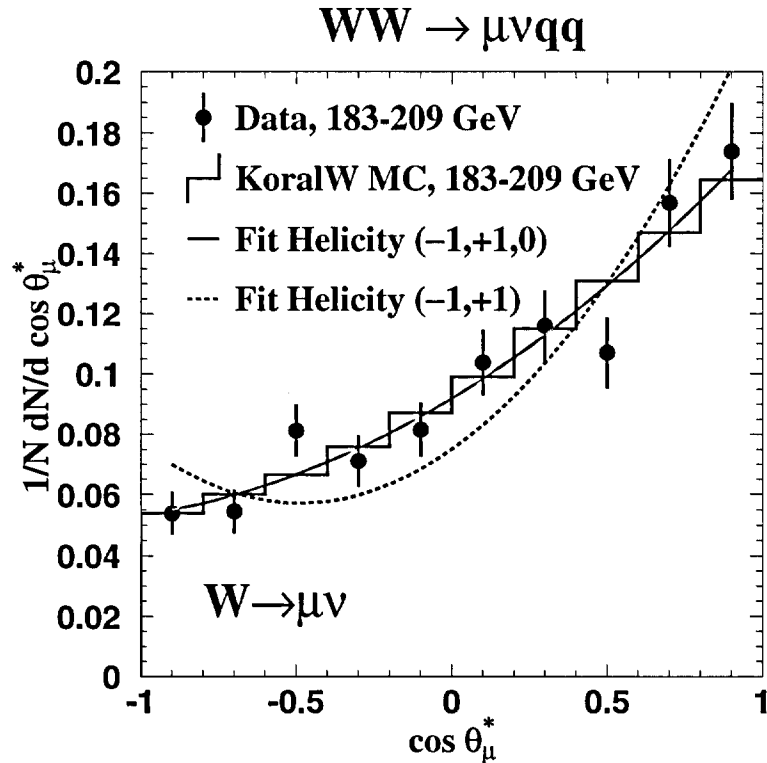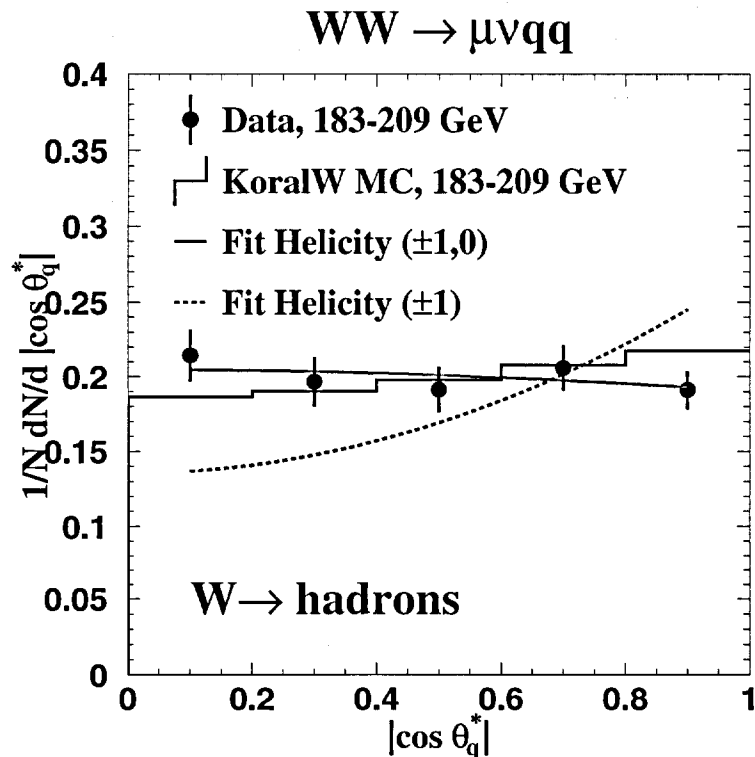
WW → eνqq

Figure 5.11: Corrected decay angle distributions for hadronic W decays at $\sqrt{s} = 183 - 209$ GeV for the $W^+W^- \rightarrow e\nu q_1\bar{q}_2$ process. Fit results for the different W helicity hypotheses are also shown.
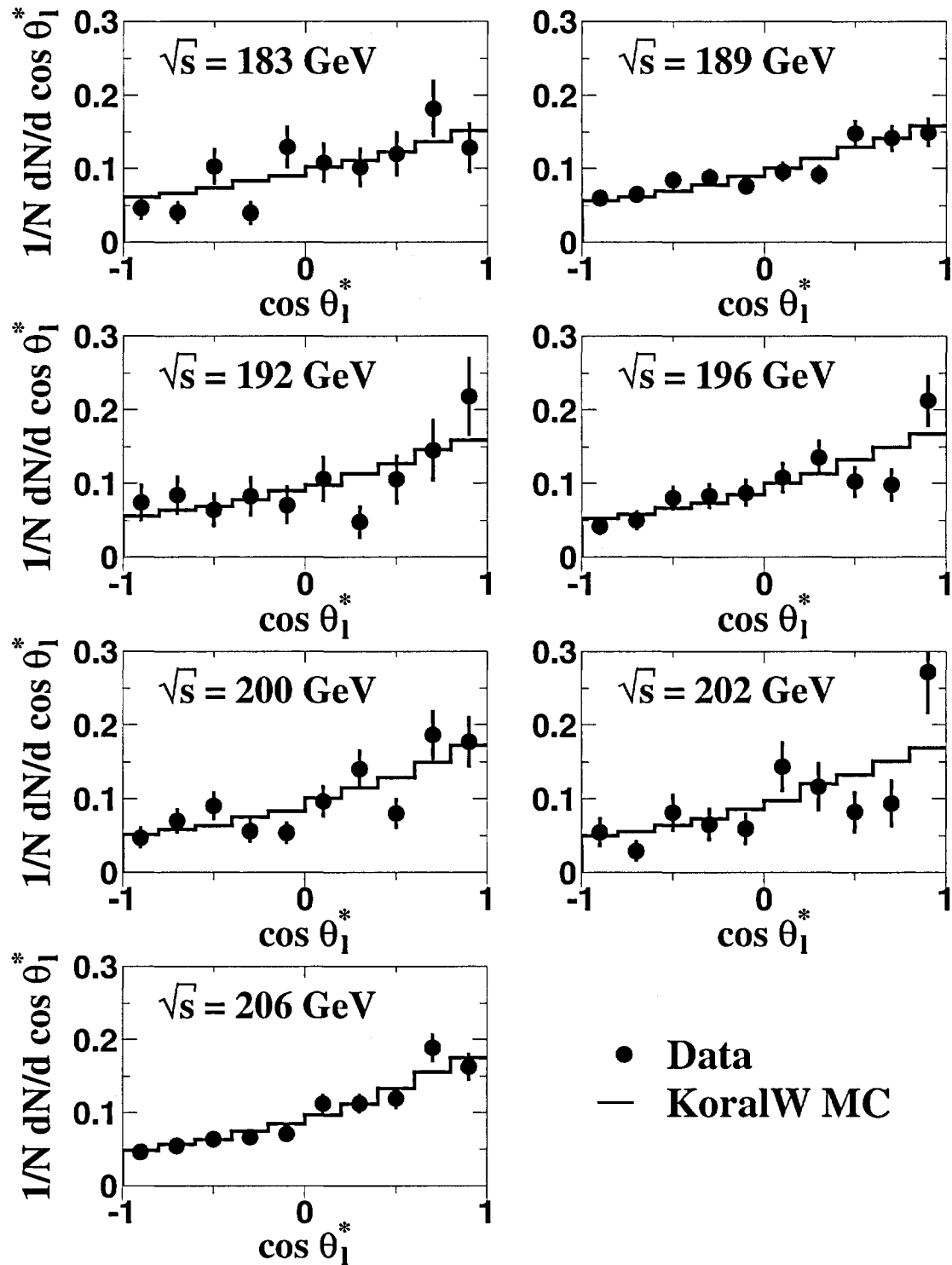
Figure 5.12: Corrected decay angle distributions for leptonic W decays at $\sqrt{s} = 183 - 209$ GeV for the $W^+W^- \rightarrow \mu\nu q_1 \bar{q}_2$ process. Fit results for the different W helicity hypotheses are also shown.

Figure 5.13: Corrected decay angle distributions for hadronic W decays at $\sqrt{s} = 183 - 209$ GeV for the $W^+W^- \rightarrow \mu\nu q_1 \bar{q}_2$ process. Fit results for the different W helicity hypotheses are also shown.

Figure 5.14: Corrected $\cos\theta_\ell^*$ distributions for all energy bins for data and KORALW Monte Carlo.
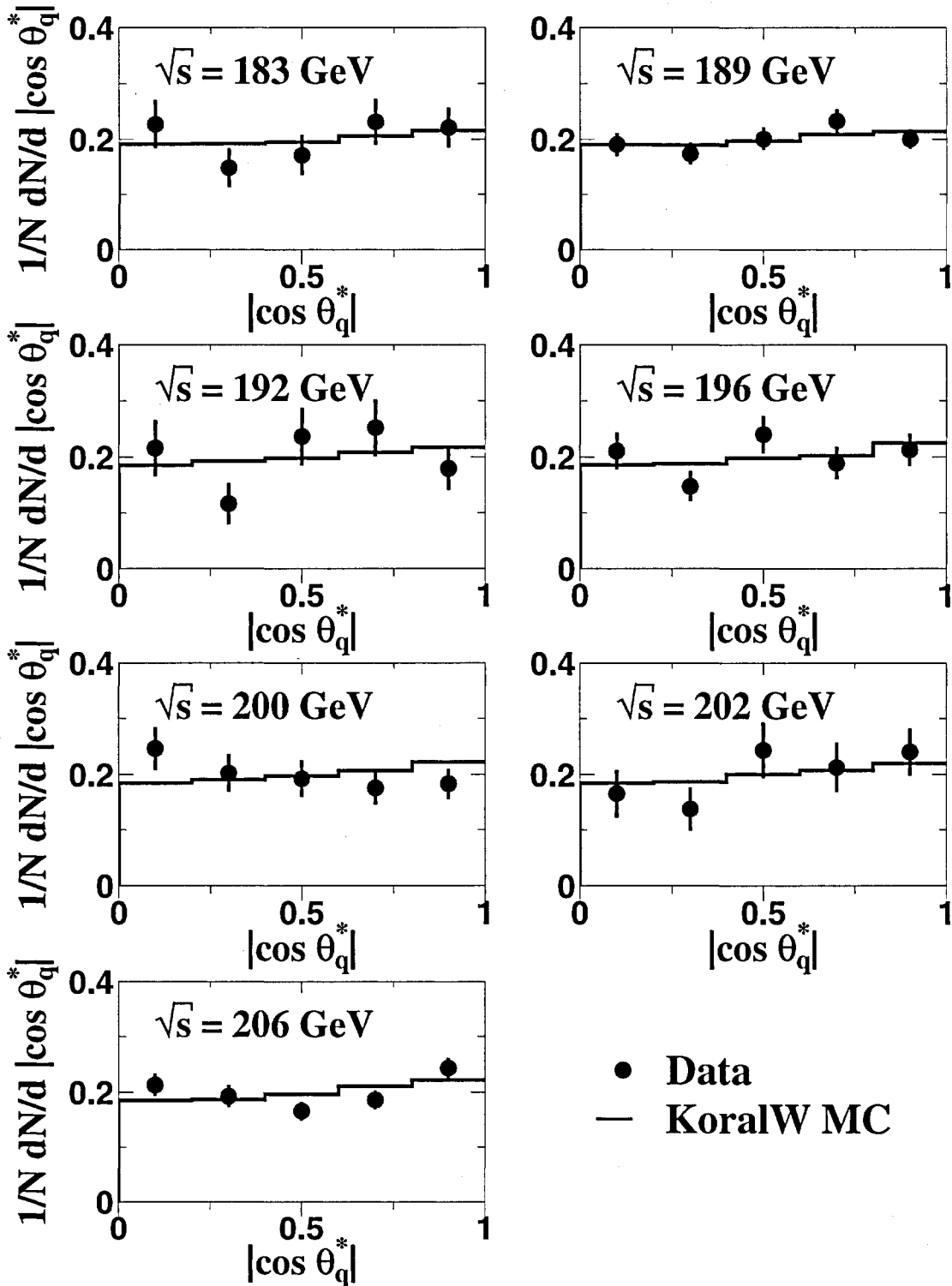
Figure 5.15: Corrected $|\cos\theta_q^*|$ distributions for all energy bins for data and KO-RALW Monte Carlo.

Figures 5.10 and 5.11 show the corrected $\cos\theta^*$ distributions for leptonic and hadronic W decays for the $W^+W^- \rightarrow e\nu q_1\bar{q}_2$ process, Figures 5.12 and 5.13 for the $W^+W^- \rightarrow \mu\nu q_1\bar{q}_2$ process. The fit results for the $W^+W^- \rightarrow e\nu q_1\bar{q}_2$ and the $W^+W^- \rightarrow \mu\nu q_1\bar{q}_2$ process are shown in Tables 5.4, 5.5 and 5.6 for leptonic, hadronic and combined fits, respectively. The agreement between these two final states is good for leptonic W decays. For hadronic W decays (see Table 5.5), the helicity fractions f_0 are $0.083\pm0.058\pm0.039$ for $e\nu q_1\bar{q}_2$ events and $0.345\pm0.058\pm0.039$ for $\mu\nu q_1\bar{q}_2$ events, corresponding to a fluctuation of 2.6 standard deviations. The combined fractions from leptonic and hadronic W decays for $e\nu q_1\bar{q}_2$ and $\mu\nu q_1\bar{q}_2$ final states are in good agreement.

The corrected $\cos\theta^*$ distributions for the particular centre-of-mass energy bins for leptonic and hadronic W decays are shown in Figures 5.14 and 5.15, respectively. Data and Monte Carlo distributions and fit results are in agreement at all centre-of-mass energies, but unfortunately the statistical errors do not allow to study the dependence on the centre-of-mass energy. One would need a factor of 10 more luminosity to measure this dependence.

5.4.2 Scattering Angle Dependence of the W Polarisation

Following the leading order analytical calculations from Chapter 2, it is easily seen that the W helicity fractions vary strongly with the W^- scattering angle, $\cos\Theta_{W^-}$. To demonstrate this, the contributions from the combinations of W^- and W^+ helicities, $(\lambda, \bar{\lambda})$, are summed up for a W^- with helicity $\lambda = +1, 0, -1$ and divided by the total differential cross-section:

$$f_\lambda(\cos\Theta_{W^-}) = \sum_{\bar{\lambda}=+1,0,-1} \frac{d\sigma\left(\lambda,\bar{\lambda}\right)}{d\cos\Theta_{W^-}} \bigg/ \frac{d\sigma}{d\cos\Theta_{W^-}} \ . \tag{5.3}$$

Figure 5.16 shows the result for 200 GeV. All three helicity contributions depend strongly on $\cos\Theta_{W^-}$. The contributions from $+1$ and 0 helicity states are very similar at $\cos\Theta_{W^-} < 0.6$. For larger $\cos\Theta_{W^-}$, the longitudinal contribution rises strongly, in contrast to the $+1$ helicity contribution. The -1 helicity state contributes very little in the backward direction, grows strongly with $\cos\Theta_{W^-}$ up to about 80%, and drops to about 50% at $\cos\Theta_{W^-} = 1$. The dominant contribution of the -1 helicity at high $\cos\Theta_{W^-}$ comes mainly from the t-channel diagram helicity amplitude for $(\lambda, \bar{\lambda}) = (-1, +1)$.

It is interesting to measure this variation of the helicity fractions with the W^- scattering angle. For this analysis, the data are grouped in four bins of $\cos\Theta_{W^-}$:

- backward: $-1.0 \leq \cos\Theta_{W^-} < -0.3$,

- central: $-0.3 \leq \cos\Theta_{W^-} < 0.3$,

- forward: $0.3 \leq \cos\Theta_{W^-} < 0.9$,

- very forward: $0.9 \leq \cos\Theta_{W^-} \leq 1.0$.

The ranges have been chosen such that large and statistically significant variations of the different helicity fractions are expected. In particular, the fraction of -1 helicity states
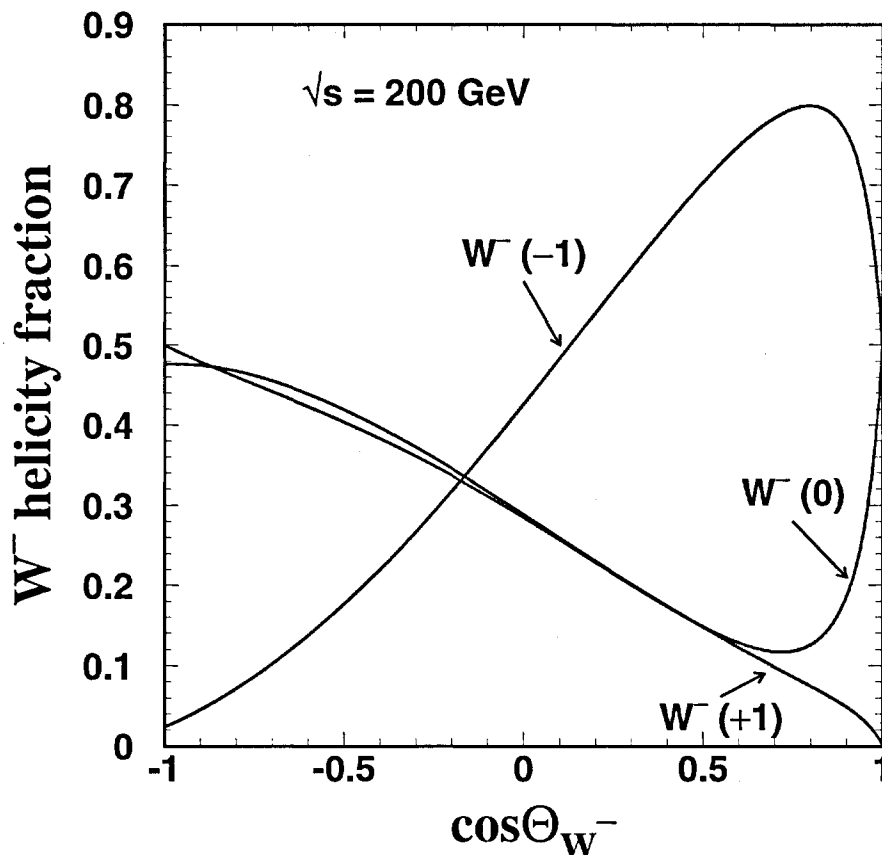
Figure 5.16: W^- helicity fractions as a function of the W production angle, $\cos \Theta_{W^-}$, for $\sqrt{s} = 200$ GeV.

is expected to change rapidly over $\cos \Theta_{W^-}$. Furthermore, the fraction of 0 helicity states in the very forward bin is expected to be slightly larger than in the forward bin.

Figures 5.17 and 5.18 show the four corrected decay angle distributions for the leptonic and hadronic W decays. A strong change in the shape of the distributions is observed, indicating a different helicity composition of the subsamples. The corrected distributions are fitted for leptonic and hadronic W decays separately in each bin of $\cos \Theta_{W^-}$.

The bias corrected fit results, combining leptonic and hadronic W decays, are given in Table 5.7 and shown in Figure 5.19, together with the Standard Model expectations from the KORALW Monte Carlo. The results are in agreement with the Standard Model description of the dynamics of the two Feynman diagrams contributing to W-pair production, and demonstrate a strong variation of the W helicity fractions with the W^- scattering angle.

As an example and combining statistical and systematic uncertainties, f_- rises from 0.173 ± 0.053 in the backward scattering bin to 0.708 ± 0.109 in the very forward scattering bin, while the fraction f_0 drops from 0.409 ± 0.097 in the backward scattering bin to 0.182 ± 0.047 in the forward scattering bin and rises again to 0.302 ± 0.101 for very forward scattered W bosons.
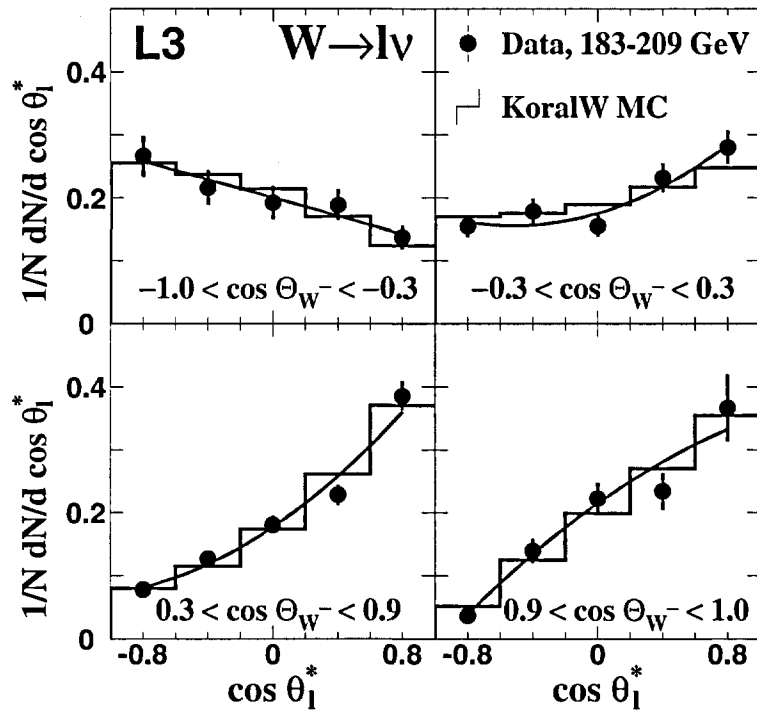
Figure 5.17: Corrected decay angle distributions for leptonic W decays separated into four different W^- scattering angle ranges, together with the KORALW expectation and fit results.
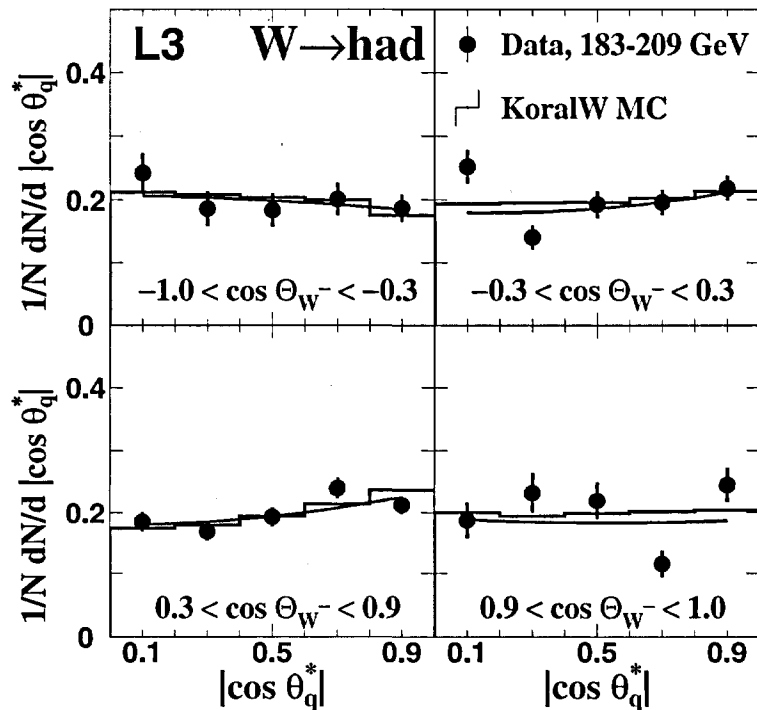

Figure 5.18: Corrected decay angle distributions for hadronic W decays separated into four different W^- scattering angle ranges, together with the KORALW expectation and fit results.

$\cos \Theta_{W^-}$	Fraction	$W^{\pm}$ Data	Monte Carlo
[-1.0, -0.3]	f_-	$0.173 \pm 0.041 \pm 0.033$	0.156 ± 0.006
	f_+	$0.418 \pm 0.060 \pm 0.043$	0.431 ± 0.008
	f_0	$0.409 \pm 0.082 \pm 0.051$	0.413 ± 0.008
[-0.3, 0.3]	f_-	$0.509 \pm 0.055 \pm 0.029$	0.446 ± 0.006
	f_+	$0.303 \pm 0.040 \pm 0.032$	0.282 ± 0.005
	f_0	$0.188 \pm 0.060 \pm 0.043$	0.272 ± 0.006
[0.3, 0.9]	f_-	$0.683 \pm 0.042 \pm 0.026$	0.723 ± 0.004
	f_+	$0.135 \pm 0.027 \pm 0.030$	0.119 ± 0.003
	f_0	$0.182 \pm 0.039 \pm 0.027$	0.158 ± 0.004
[0.9, 1.0]	f_-	$0.708 \pm 0.093 \pm 0.056$	0.647 ± 0.007
	f_+	$-0.010 \pm 0.055 \pm 0.028$	0.029 ± 0.004
	f_0	$0.302 \pm 0.082 \pm 0.059$	0.324 ± 0.007

Table 5.7: The W^- helicity fractions measured as a function of $\cos \Theta_{W^-}$, combining leptonic and hadronic W decays. The first uncertainty is statistical, the second systematic. The KORALW Monte Carlo expectations are also given with their statistical uncertainties.
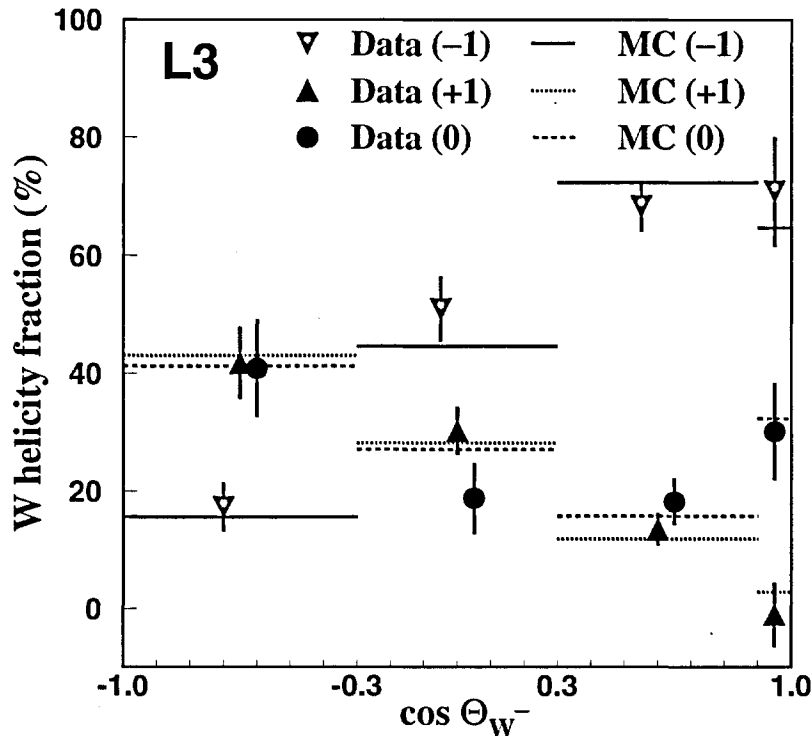

Figure 5.19: W helicity fractions f_-, f_+ and f_0 and their statistical uncertainties for four different bins of $\cos \Theta_{W^-}$ in the combined data sample and in the KORALW Monte Carlo for $\sqrt{s} = 183 - 209$ GeV.

5.4.3 Discussion of the Results

Several tests of basic principles and predictions of the Standard Model have been performed. First, the existence of the longitudinal polarised W boson has been clearly demonstrated by comparing the data to a hypothesis with longitudinal polarisation and a hypothesis with only transverse polarisation. The probability that the latter one is true is negligible. Combining statistical and systematic error, the fraction of longitudinal polarised W bosons is measured as 0.218 ± 0.031, which corresponds to a significance of seven standard deviations.

The measured values for all three helicity states are in good agreement with the Standard Model predictions, separately in the leptonic and hadronic decay, and also in the inclusive sample.

The helicity fractions obtained from separate measurements in the $e\nu q_1 \bar{q}_2$ and the $\mu\nu q_1 \bar{q}_2$ samples generally agree well with each other, although some minor deviations have been found in the hadronic decay.

CP invariance has been tested by measuring the helicity fractions separately for W^+ and W^-. The results agree well with each other.

The dynamics of W-pair production via s-channel and t-channel diagrams results in a strong dependence of the helicity fractions on the W^- scattering angle, $\cos\Theta_{W^-}$. The t-channel W-pair production results in a strong peak of the -1 helicity state slightly below $\cos\Theta_{W^-} = 1$. This behaviour is probed by measuring the helicity fractions in intervals of the W^- scattering angle. The measured helicity fractions confirm the Standard Model predictions and demonstrate indeed a significant variation with the W^- scattering angle.

The fraction of the longitudinal polarisation of W bosons has been measured at LEP also by the OPAL and DELPHI collaborations using the spin density matrix approach. These analyses use a set of weighted projection operators depending on the angles measured in the W-pair process to obtain estimators for the spin density matrix of a W boson, and obtain the fraction of longitudinal polarisation from one of its elements. The final results from OPAL [30] as well as the preliminary results from DELPHI [31] are in agreement with the presented L3 results. OPAL measures a fraction of $(23.9 \pm 2.4)\%$ for the longitudinal polarisation at centre-of-mass energies of $\sqrt{s} = 183 - 209$ GeV, using also semileptonic W-pair final states with a tau, DELPHI measures $(24.9 \pm 3.3)\%$ in data collected at $\sqrt{s} = 189 - 209$ GeV.

The sensitivity of the W boson polarisations to anomalous triple gauge couplings (TGC) has been studied using the standard method of parametrisation [24]. Fits using Monte Carlo events with different values of the CP-conserving TGC's $\Delta\kappa_\gamma$ (0.8, 0.4, -0.4, and -0.8) and λ_γ (0.4, 0.2, -0.2, and -0.4) have been compared to the Standard Model Monte Carlo fit results. The differences in the polarisation fractions are of the order of the statistical error. This is expected because anomalous TGS's are determined from the W-pair cross-section and the angular distributions, whereas the analysis presented in this thesis uses only the shape of the polar decay angle.

Chapter 6

Measurement of W^+W^- Spin Correlations

6.1 Introduction

In the previous chapters, the measurement of the longitudinal W bosons and the variation of the helicity composition of one W boson with the W scattering angle has been described and was found to be in very good agreement with the Standard Model

Based on these results and the developed analysis methods, spin correlations between W bosons have been studied[1]. The existence of correlations between the helicity states of W bosons in W-pair production is a basic test of the quantum mechanics. The theoretical behaviour, as calculated basing on the formulæ from chapter 2.2, is shown in Figure 6.1, where the differential cross-section of the particular combinations of W^+W^- helicities is plotted, as a function of the W^- scattering angle, $\cos\Theta_{W^-}$. The measurement of the magnitude of the spin correlations is a test of the Standard Model. Deviations from the Standard Model predictions would suggest effects from physics with a symmetry breaking mechanism which affects interactions of longitudinally polarised W bosons.

In this chapter, a measurement of correlations between the helicity states of W bosons in W-pair events is described. In particular, we focus on the helicity combination $(\lambda, \bar{\lambda}) = (-1, +1)$ as it is the dominant contribution to the W-pair differential cross-section in the forward direction and thus should give the most clearly observable spin correlations. This combination is also interesting, because as a $J_0 = 2$ state, it can only be produced via the t-channel neutrino exchange. The helicity combinations $(\lambda, \bar{\lambda}) = (0, 0)$ are also interesting because of the direct connection to the Higgs-sector of the Standard Model, as explained in chapter 2.3. To date, no direct evidence for this double-longitudinal state has been shown.

Using the EEWW Monte Carlo program, which assigns helicities on an event-by-event basis, the W spin correlations have been studied in detail for the centre-of-mass energy $\sqrt{s} = 189$ GeV. The helicity composition of one W boson with respect to a given helicity of the other W boson can be determined directly.

---

[1]Or, as I usually ask in conference talks: "Does one of the W's squeal when we pinch the other one ?"
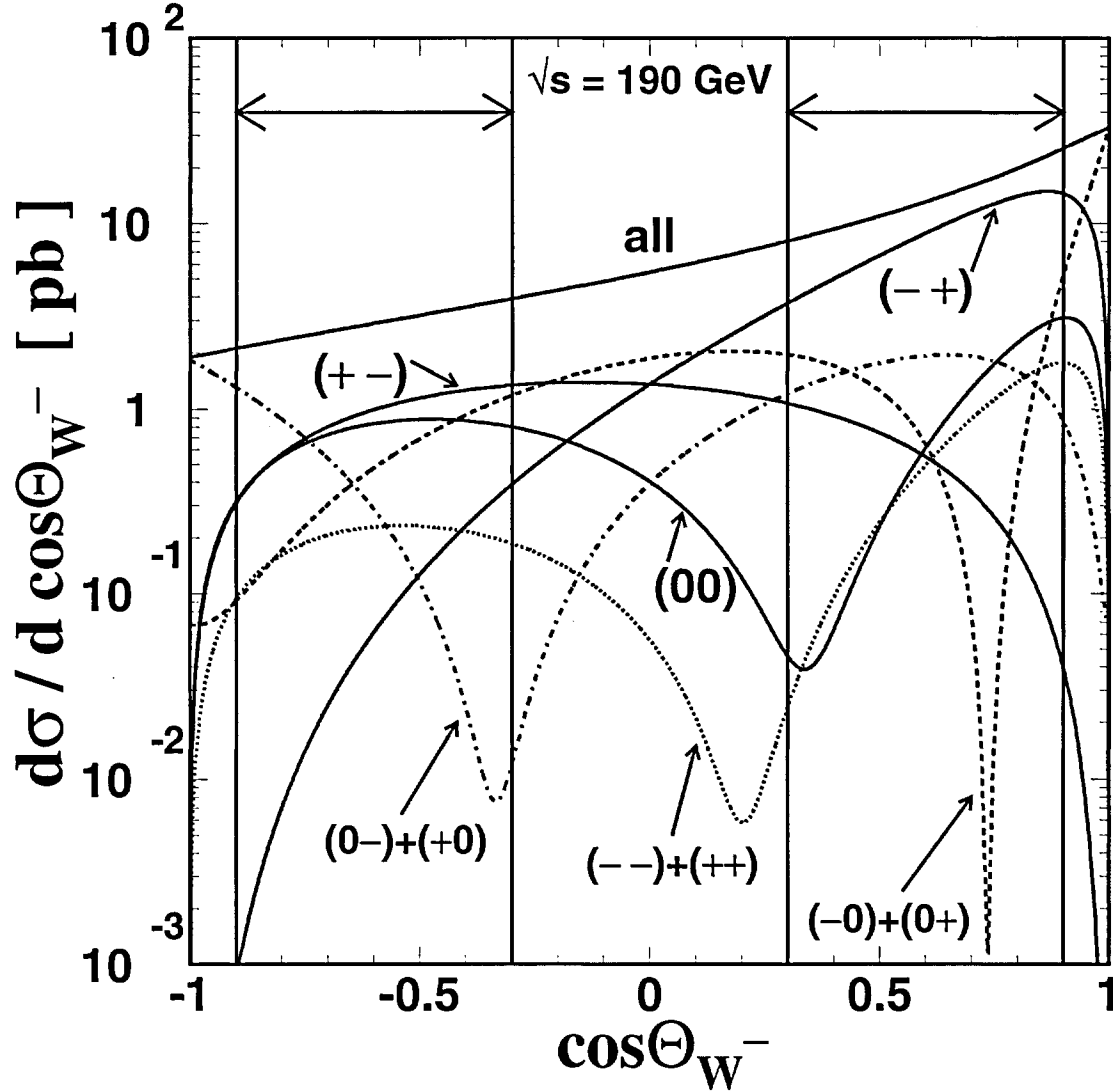
Figure 6.1: Differential cross section for pair production for different W^+W^- helicity states at $\sqrt{s} = 190$ GeV, averaged over initial electron polarisations. The W^- and W^+ helicities in the e^+e^- centre-of-mass frame are given in parentheses. The intervals used for the analysis of W spin correlations are indicated by the arrows.

Figure 6.2 shows the relative contributions of the particular helicity combinations to the total cross-section, as a function of the W^- scattering angle. One sees the forward peak of $(\lambda, \bar{\lambda}) = (-1, +1)$ and a relatively large fraction of the double-longitudinal state $(\lambda, \bar{\lambda}) = (0, 0)$ in the backward region.

Therefore, one can try to observe W spin correlations $(-1, +1)$ and $(0, 0)$ in regions where they are enriched. Two intervals have been chosen which provide reasonable statistics, fulfilling the above requirement. For this analysis, the intervals $0.3 < \cos\Theta_{W^-} < 0.9$
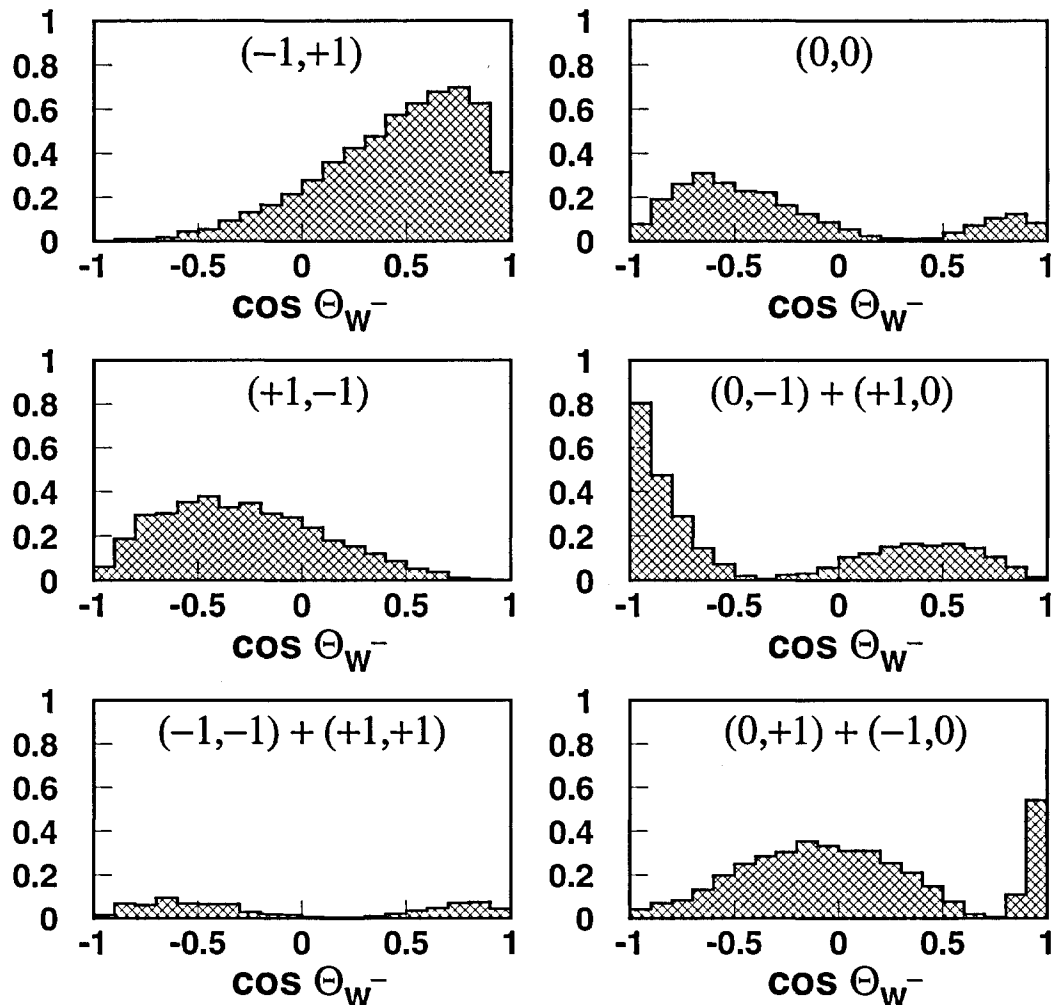
Figure 6.2: Relative contributions of the particular helicity combinations $(\lambda, \bar{\lambda})$ to the total W-pair cross-section, as a function of the W^- scattering angle, $\cos\Theta_{W^-}$.

and $-0.9 < \cos\Theta_{W^-} < -0.3$ are chosen, which are marked in Figure 6.1. Table 6.1 shows the generated fractions of W^-W^+ helicity combinations obtained using EEWW in the whole sample and in the two intervals used for the analysis. An increase in the fractions of $(-1, +1)$ and $(0, 0)$ compared to the inclusive sample is expected.

6.2 Analysis Strategy

In contrast to the EEWW Monte Carlo program, where the helicity of the W bosons can be identified unambiguously, in data or KORALW Monte Carlo events only statistical evidence can be hoped for. Measurements of W spin correlations are performed using the following strategy.

For the measurement, two subsamples of events are formed: the first is enriched in

		$W^+(-1)$	$W^+(+1)$	$W^+(0)$
	$W^-(-1)$	0.022	0.431	0.109
all $\cos\Theta_{W^-}$	$W^-(+1)$	0.106	0.021	0.053
	$W^-(0)$	0.055	0.108	0.094
	$W^-(-1)$	0.024	0.629	0.042
$0.3 < \cos\Theta_{W^-} < 0.9$	$W^-(+1)$	0.042	0.026	0.060
	$W^-(0)$	0.062	0.042	0.074
	$W^-(-1)$	0.037	0.043	0.090
$-0.9 < \cos\Theta_{W^-} < -0.3$	$W^-(+1)$	0.315	0.033	0.068
	$W^-(0)$	0.073	0.093	0.248

Table 6.1: Fractions of W^-W^+ helicity combinations $(\lambda, \bar\lambda)$ in the whole sample and in the considered $\cos\Theta_{W^-}$ intervals. The fractions are obtained using a sample of 100000 EEWW Monte Carlo events.

events where one of the W bosons has a transverse helicity state $\lambda = \pm 1$, and the second is depleted of these events. The helicity composition of the other W boson is then analysed in both subsamples, and the obtained fractions are compared to determine the correlation.

As the full helicity information $(-1, +1, 0)$ can be only retrieved from the W boson decaying into leptons, it is chosen as the one used for analysis of the helicity composition, while the W boson which decays into hadrons is used for the depletion and enrichment of the W-pair events with transverse helicity states. Given CP conservation, as verified in Chapter 5, which links the helicity states of a W^- to the opposite helicity states of a W^+, $\lambda = -\bar\lambda$, such a choice is equivalent to the use of e.g. W^+ for depletion and enrichment and W^- for the analysis of the helicity composition.

For the enrichment and depletion we make use of the fact that the helicity fractions of the hadronically decaying W boson change with the polar decay angle, $|\cos\theta_q^*|$. According to Equation 5.2, for small values of $|\cos\theta_q^*|$, the sample is depleted of helicity ± 1 states, while for large polar decay angles the sample is enriched in helicity ± 1 states, as shown in Figure 6.3. The interval $|\cos\theta_q^*| < 0.33$ is chosen for the $\lambda = \pm 1$ depleted sample and the interval $|\cos\theta_q^*| > 0.66$ for the $\lambda = \pm 1$ enriched sample. The helicity fractions of the W^- bosons decaying into leptons are then obtained from a fit of Equation 5.1 to the event distribution, $dN/d\cos\theta_\ell^*$.

As explained in the previous section, to increase the sensitivity of the measurement, subsamples of particular helicity combinations are selected. The following two intervals are considered:

- the forward bin, $0.3 < \cos\Theta_{W^-} < 0.9$, where the fraction of the helicity combination $(\lambda, \bar\lambda) = (-1, +1)$ is increased to about 63% of all W pairs, compared to an average value of 43% over the whole $\cos\Theta_{W^-}$ range, and

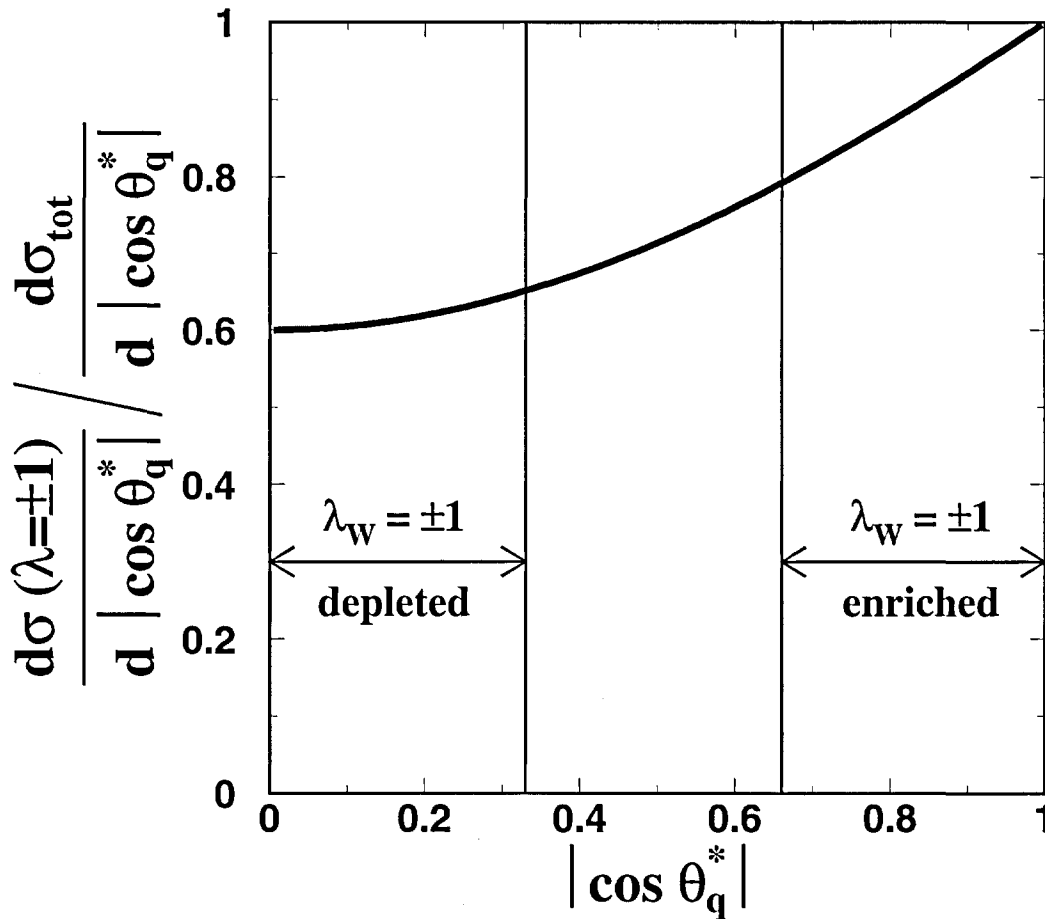- the backward bin, $-0.9 < \cos\Theta_{W^-} < -0.3$, where the fraction of the helicity

Figure 6.3: Relative contribution of the helicity states ± 1 to the $e^+e^- \to W^+W^- \to \ell\nu q_1\bar{q}_2$ differential cross section, as a function of $|\cos\theta_q^*|$. The intervals used for the analysis of W spin correlations are indicated.

combination $(\lambda, \bar{\lambda}) = (0, 0)$ is increased to about 25%, compared to an average value of 9%.

The Standard Model predictions for the fractions of helicity states for the leptonically decaying W boson in both $\cos\Theta_{W^-}$ and $|\cos\theta_q^*|$ bins are obtained from the distributions generated at different values of $\sqrt{s}$ using KORALW, combined according to the collected luminosity. The consistency of the predictions for W spin correlations has been tested also with large samples of signal events, which have been generated using the EEWW and YFSWW Monte Carlo programs. The predictions are found to agree with each other, within statistical uncertainties.

The size of the expected correlation effects is small and, given the available event statistics, only indications for W spin correlations might be observed. Still these measurements might reveal sizable deviations from the Monte Carlo predictions and demonstrate how these important predictions can be tested at future high luminosity colliders.

6.3   Analysis of W^+W^- Spin Correlations

The W-pair events are classified according to the values of $\cos\Theta_{W^-}$ and $|\cos\theta^*_q|$ to build four test samples:

$$0.3 < \cos\Theta_{W^-} <\ \ 0.9,\ \ |\cos\theta^*_q| < 0.33\ ;\ \ \ \ 0.3 < \cos\Theta_{W^-} <\ \ 0.9,\ \ |\cos\theta^*_q| > 0.66\ ;$$

$$-0.9 < \cos\Theta_{W^-} < -0.3,\ \ |\cos\theta^*_q| < 0.33\ ;\ \ \ -0.9 < \cos\Theta_{W^-} < -0.3,\ \ |\cos\theta^*_q| > 0.66\ .$$

In each of the samples, the fractions of W helicity states for W bosons decaying into leptons are obtained from the event distributions, $dN/d\cos\theta^*_\ell$. For each energy point, the background, as obtained from Monte Carlo simulations, is subtracted from the data. The resulting distributions are corrected for efficiencies as obtained from the ratio of the angular distributions for simulated and generated events for large samples of KORALW Monte Carlo events. This method of efficiency corrections accounts for selection efficiencies, the presence of initial state radiation and migration effects. The efficiencies differ only slightly for the particular centre-of-mass energies.

For each of the test samples, the corrected decay angle distributions for different values of $\sqrt{s}$ are combined into a single distribution. The resulting distributions are shown in Figures 6.4 and 6.5. They are then fitted with the function in Equation 5.1, using f_- and f_0 as the fit parameters. The fraction f_+ is obtained by constraining the sum of all three parameters to unity.

Finally, the fitted fractions are corrected for the bias as explained in Chapter 5.2.3. Bias correction functions are determined in each of the investigated $\cos\Theta_{W^-}$ and $|\cos\theta^*_q|$ ranges. The bias in these ranges was studied in detail. As for the inclusive studies, it depends on the centre-of-mass energy and the helicity fractions. Furthermore, the bias also depends on the detector region and thus each $\cos\Theta_{W^-}$ and $|\cos\theta^*_q|$ range has a different bias correction function.

Technically, the whole data sample in each bin is corrected for bias using a luminosity weighted sample of EEWW events at the particular energies, as opposed to correcting the fits results at each energy separately. This approach is beneficial because the linear approximation of the bias correction function is valid only in a small range around the measured value. If each energy was corrected separately, the correction of the relatively large errors would yield asymmetric errors which are more difficult to deal with.

The size of the bias correction varies from 1% to 15%, which is small compared to the statistical error. The statistical errors are enlarged by 20% on average.

6.4   Systematic Effects

For the results of the analysis, several sources of systematic uncertainties are considered. All systematic uncertainties are small compared to the statistical errors. The systematic uncertainties for the measurement of the helicity fractions f_- and f_0 for all bins of $\cos\Theta_{W^-}$ and $|\cos\theta^*_q|$ are summarised in Table 6.2. The largest uncertainties arise from selection criteria and binning effects.

| | $0.3 < \cos\Theta_{W^-} < 0.9$ | | | | $-0.9 < \cos\Theta_{W^-} < -0.3$ | | | |
| | ±1 depleted | | ±1 enriched | | ±1 depleted | | ±1 enriched | |
	f_-	f_0	f_-	f_0	f_-	f_0	f_-	f_0
Selection	0.034	0.045	0.010	< 0.001	0.053	0.048	0.050	0.087
Fit binning	0.027	0.021	0.030	0.057	0.078	0.097	0.020	0.051
Bias correction	0.018	0.026	0.010	0.013	0.031	0.055	0.016	0.034
Efficiency correction	0.003	0.001	0.005	0.004	0.004	0.006	0.002	0.005
Four fermions	0.001	0.006	0.006	0.003	0.012	0.024	0.003	0.026
Background levels	0.006	0.008	0.004	0.008	0.022	0.024	0.014	0.019
Total systematic	0.048	0.057	0.034	0.059	0.102	0.126	0.058	0.111
Statistical	0.086	0.116	0.057	0.072	0.136	0.316	0.082	0.215

Table 6.2: Systematic uncertainties on the measurement of f_- and f_0 for leptonic W decays in bins of $\cos\Theta_{W^-}$ and for samples depleted of and enriched in the ±1 helicity. For comparison, the statistical error is also given.

The selection cuts are varied over a small range around the actual value, including the cuts on $|\cos\theta_q^*|$. Shifting the selection cuts however results in a different number of selected events, and thus also a certain difference in the fit results is expected. The variation of the fitted helicity fractions due to the change of selected events is the statistical component:

$$\Delta\varepsilon = \Delta\sigma \sqrt{\frac{|\Delta N|}{N}} , \qquad (6.1)$$

where $\Delta\sigma$ reflects the statistical error of the considered quantity, N the number of selected events with the original cut, and ΔN the change in the number of selected events with the modified cut. The statistical component of the systematic uncertainty is then corrected for by subtracting $\Delta\varepsilon$ in quadrature from the systematic uncertainty. The obtained result is retained as systematics.

As shown in Table 6.2, the systematic error for the selection of f_0 in the forward bin, $0.3 < \cos\Theta_{W^-} < 0.9$, for $f_\pm$ enriched is considerably smaller than the others. This is the result of the data statistics being so small, which makes it insensitive to the variations in the selection procedure. This also happens if the variations of the selection cuts are somehow enlarged.

All fits are repeated with one bin more or one bin less in the angular distributions. The average difference is retained as systematics.

Uncertainties on the bias and the efficiency corrections are determined with large Monte Carlo samples. The analysis is redone varying the bias and efficiency correction functions by one standard deviation on both sides. The difference is retained as systematics.

Additional contamination from the non double-resonant four-fermion final states is evaluated using the EXCALIBUR Monte Carlo. Two samples of 100000 $e\nu q_1\bar{q}_2$ events each are generated using EXCALIBUR Monte Carlo, one containing only CC03 processes and the second one containing all four-fermion final state processes mediated by at least

one W boson (CC20). The analysis is redone using both samples, and the difference is retained as systematics.

Background levels are varied according to Monte Carlo statistics for the background processes. The analysis is repeated varying the background levels by one standard deviation on both sides, taking the difference as systematics.

Generally, the systematic errors for backward production of W bosons are considerably larger than for the forward production. Several effects account for this. For the uncertainty on the selection, the events which are in the backward bin have a lower purity and are thus closer to the cuts. The background contamination and the four-fermion contribution are relatively higher, and so are the uncertainties connected to their variation. As for the binning uncertainty, the data sets in the backward bin are much smaller, and thus statistical effects play a role. For the same reason, also the variation of the bias correction function is larger.

6.5   Results

The results of the fits are summarised in Table 6.3. For the two considered $\cos\Theta_W$-intervals, the helicity fractions of the W boson decaying into leptons are shown for data and KORALW Monte Carlo. The results are shown for the two subsamples of hadronically decaying W bosons which are depleted of ± 1 helicity or enriched in ± 1 helicity.

Comparing the helicity fractions measured in the ± 1 depleted sample for data and Monte Carlo, we observe good agreement. Small deviations occur for the fraction f_-, which is 0.521 ± 0.098 for data (combining statistical and systematic uncertainties) and 0.670 ± 0.008 for Monte Carlo in the forward bin. In the backward bin, f_- is 0.387 ± 0.170 for data and 0.186 ± 0.014 for Monte Carlo. For the ± 1 enriched sample, data and Monte Carlo are overall in good agreement.

W-pair spin correlations would manifest themselves as sizable differences between the values of the helicity fractions measured for the samples depleted of ± 1 helicity and enriched in ± 1 helicity. These differences are listed in boldface in Table 6.3.

The spin correlations in the data are strongest in the forward bin, $0.3 < \cos\Theta_{W^-} < 0.9$, where the difference between the two f_- fractions is -0.32 ± 0.12 (combining statistical and systematic uncertainties), and 0.28 ± 0.16 between the two f_0 fractions. This corresponds to a significance of 2.7 standard deviations for f_- and 1.8 standard deviations for f_0. The effect of the W-pair spin correlations in the backward bin is 0.24 ± 0.20 for f_- and -0.10 ± 0.42 for f_0. The significances are 1.2 standard deviations and 0.2 standard deviations for f_- and f_0, respectively.

The correlations observed with the data are slightly stronger than predicted by the KORALW Monte Carlo. In the forward bin, the differences for the fractions f_- and f_0 are about 1.7 and 1.4 standard deviations stronger than predicted, respectively. However, the somewhat even stronger differences between data and Monte Carlo observed with the lower energy data sample (collected at $\sqrt{s} = 183 - 202$ GeV) [2] are not confirmed with the year 2000 data.

The significances for the helicity fractions f_-, f_+ and f_0 cannot be simply added to

forward bin: $0.3 < \cos\Theta_{W-} < 0.9$: $(\lambda_{W-}, \lambda_{W+}) = (-1, +1)$ enriched		
f_-	f_+	f_0
Data ±1 depleted		
$0.521 \pm 0.086 \pm 0.048$	$0.121 \pm 0.058 \pm 0.035$	$0.358 \pm 0.116 \pm 0.057$
Data ±1 enriched		
$0.839 \pm 0.057 \pm 0.034$	$0.087 \pm 0.034 \pm 0.036$	$0.074 \pm 0.072 \pm 0.059$
Difference		
$\mathbf{-0.318 \pm 0.103 \pm 0.059}$	$\mathbf{0.034 \pm 0.067 \pm 0.050}$	$\mathbf{0.284 \pm 0.137 \pm 0.082}$
MC ±1 depleted		
0.670 ± 0.008	0.148 ± 0.006	0.182 ± 0.012
MC ±1 enriched		
0.781 ± 0.007	0.091 ± 0.004	0.128 ± 0.009
Difference		
$\mathbf{-0.111 \pm 0.011}$	$\mathbf{0.057 \pm 0.007}$	$\mathbf{0.054 \pm 0.015}$

backward bin: $-0.9 < \cos\Theta_{W-} < -0.3$: $(\lambda_{W-}, \lambda_{W+}) = (0, 0)$ enriched		
f_-	f_+	f_0
Data ±1 depleted		
$0.387 \pm 0.136 \pm 0.102$	$0.398 \pm 0.121 \pm 0.061$	$0.215 \pm 0.316 \pm 0.126$
Data ±1 enriched		
$0.152 \pm 0.082 \pm 0.058$	$0.530 \pm 0.101 \pm 0.087$	$0.318 \pm 0.215 \pm 0.111$
Difference		
$\mathbf{0.235 \pm 0.159 \pm 0.117}$	$\mathbf{-0.132 \pm 0.158 \pm 0.107}$	$\mathbf{-0.103 \pm 0.382 \pm 0.168}$
MC ±1 depleted		
0.186 ± 0.014	0.351 ± 0.016	0.463 ± 0.023
MC ±1 enriched		
0.158 ± 0.014	0.532 ± 0.017	0.310 ± 0.026
Difference		
$\mathbf{0.028 \pm 0.020}$	$\mathbf{-0.181 \pm 0.023}$	$\mathbf{0.153 \pm 0.035}$

Table 6.3: The helicity fractions of the leptonically decaying W boson measured for different intervals of $\cos\Theta_{W-}$, with their statistical and systematic uncertainties. The results are shown for different subsamples of W decays into hadrons depleted of or enriched in ±1 helicity, and their differences are also given. The corresponding helicity fractions in the Standard Model, as implemented in the KORALW Monte Carlo program, are also given with their statistical uncertainties. For further explanations see text.

	$f_- - f_0$ correlation coefficient			
	Data		Monte Carlo	
	± 1 depleted	± 1 enriched	± 1 depleted	± 1 enriched
$0.3 < \cos\Theta_{W^-} < 0.9$	-92%	-93%	-88%	-91%
$-0.9 < \cos\Theta_{W^-} < -0.3$	-76%	-77%	-80%	-78%

Table 6.4: Correlation coefficients between the fit parameters f_- and f_0. The errors on these coefficients are negligible.

obtain a conclusion, because they are strongly correlated. Table 6.4 shows the correlation coefficients of the parameters f_- and f_0 derived from the fit. To calculate the total χ^2 of the effect, the covariance matrix must be taken into account:

$$\chi^2 = \vec{\sigma}^{\,T} \, W \, \vec{\sigma}, \quad \text{with} \quad W = \frac{1}{1-\rho^2} \begin{pmatrix} \frac{1}{\sigma_1^2} & \frac{-\rho}{\sigma_1\sigma_2} \\ \frac{-\rho}{\sigma_1\sigma_2} & \frac{1}{\sigma_2^2} \end{pmatrix}, \tag{6.2}$$

where $\vec{\sigma} = (\sigma_1, \sigma_2)$ is the vector of standard deviations and $\rho = \frac{cov_{1,2}}{\sigma_1\sigma_2}$ the correlation coefficient.

Two consistency tests are performed, calculating the χ^2 according to Equation 6.2 and the confidence level for compatibility of the results with this hypothesis. This calculation is based on the differences in the f_- and f_0 fractions as listed in Table 6.3 and taking into account the correlation coefficients as listed in Table 6.4.

In the first test, only data is considered and a confidence level is calculated for the absence of W-boson spin correlations, i.e. a difference of 0 in all fractions and bins. The χ^2 for the absence of spin correlations is 12.9, which corresponds to a confidence level of 1.2%.

The second test compares the data with the Standard Model KORALW Monte Carlo. The χ^2 for this hypothesis is 4.5, which corresponds to a confidence level of 34.7%.

The presented analysis constitutes the first direct and model independent measurement of W spin correlations. The results allow to conclude that W-boson spin correlations are observed with a significance of about three standard deviations, and that data and Standard Model Monte Carlo are in good agreement.

The results would be statistically more significant if one could combine the results of all LEP experiments. The significances, presently at the 2 to 3 standard deviation level, would be twice as big if similar results from all four experiments could be used. Unfortunately, none of the other LEP experiments has performed this measurement.
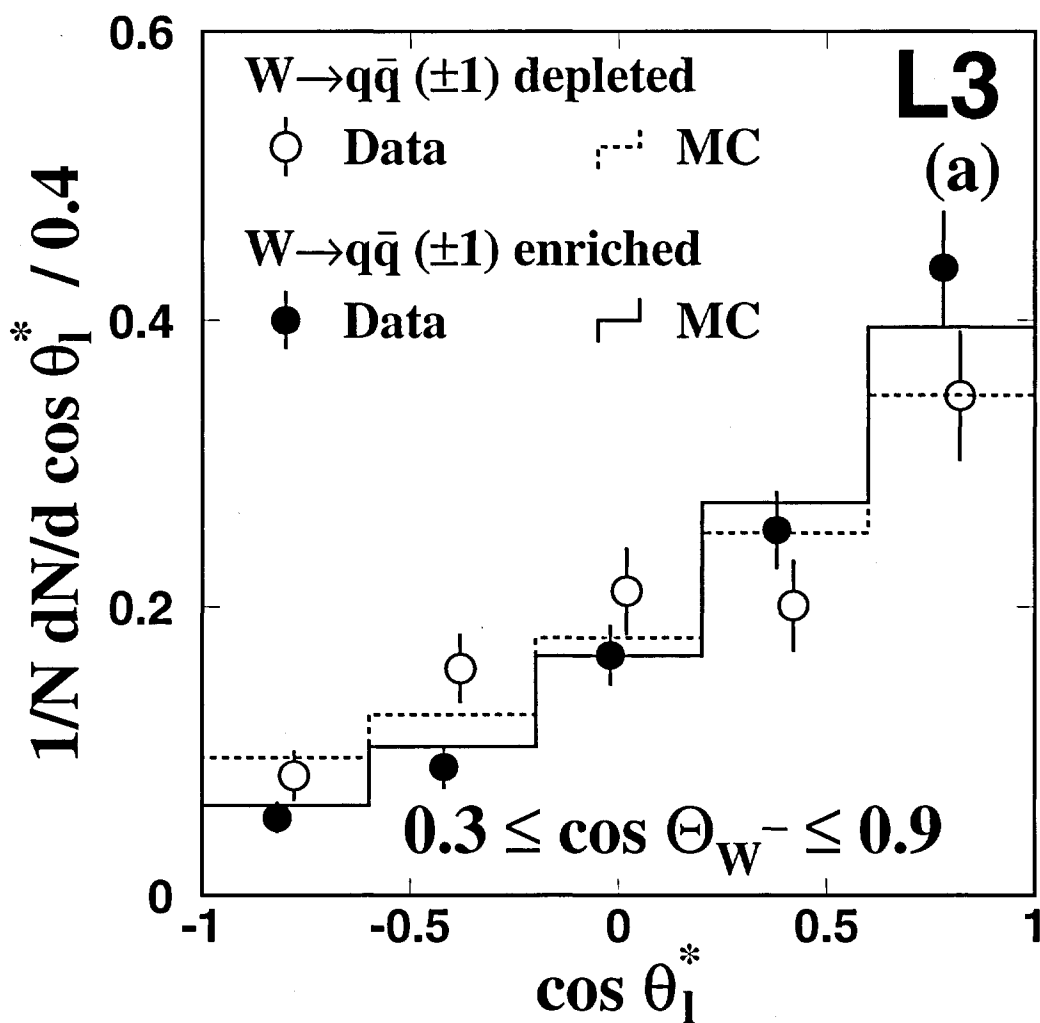
Figure 6.4: Corrected $\cos\theta_\ell^*$ distributions for $W \to \ell\nu$ decays for data and the KORALW Monte Carlo in the interval $0.3 < \cos\Theta_{W^-} < 0.9$. The distributions are shown for subsamples of W decays into hadrons depleted of and enriched in ± 1 helicity. For clarity, the data points are slightly shifted. In absence of spin correlations, the two histograms and data point sets would match.
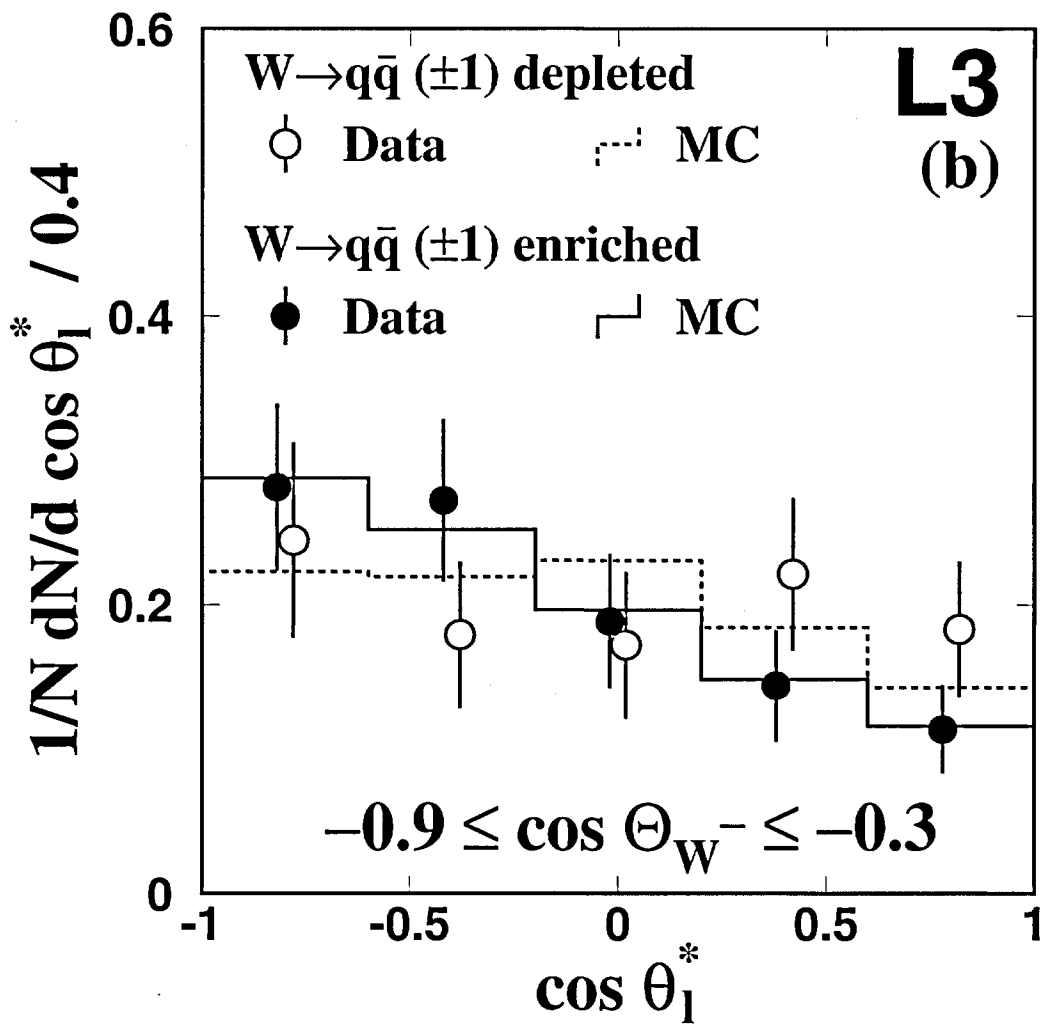
Figure 6.5: Corrected $\cos\theta_\ell^*$ distributions for $W \to \ell\nu$ decays for data and the KORALW Monte Carlo in the interval $-0.9 < \cos\Theta_{W^-} < -0.3$. The distributions are shown for subsamples of W decays into hadrons depleted of and enriched in ±1 helicity. For clarity, the data points are slightly shifted. In absence of spin correlations, the two histograms and data point sets would match.

Chapter 7

Measurement of WW Decay Plane Correlations

7.1 Introduction

An important test for new physics is the measurement of correlations between the decay planes of the W boson pair. Decay-plane correlations can be studied using the absolute value of the angle between the planes defined by the decay products of the two W bosons in the rest frame of the W-pair system.

$$|\Delta\phi| = |\phi_\ell - \phi_q| \tag{7.1}$$

The orientation of the two decay planes with respect to each other is measured by the parameter D of the differential distribution [61, 62]:

$$\frac{1}{N}\frac{dN}{d|\Delta\phi|} = 1 + D\cos 2|\Delta\phi|. \tag{7.2}$$

According to an a priori estimate, D must be smaller than $(m_W^2/m_{WW}^2)^2$.

Decay plane correlations might be sensitive to new physics which only negligibly modify the W-pair cross-section and thus would not be visible with other W observables. While the cross-section is sensitive to the $\mathcal{M}_{\lambda,\bar\lambda}$ helicity amplitudes $\mathcal{M}_{+1,-1}$, $\mathcal{M}_{-1,+1}$ and $\mathcal{M}_{0,0}$, modifications of $\mathcal{M}_{+1,+1}$ and $\mathcal{M}_{-1,-1}$ mostly contribute to decay plane correlations. New physics which gives only transverse polarised W bosons and which contributes to leading order in m_{WW}^2 yields a non-zero D. Within the Standard Model, D must be smaller than $(m_W^2/m_{WW}^2)^2$ or a few percent, thus any value significantly higher suggests new physics.

7.1.1 Leading Order Analytical Calculation

The decay plane correlation parameter D is calculated using the formulæ given in chapter 2.2 and [62].

$$D = \frac{1}{4N}\left(\mathcal{P}_{-1,-1}^{+1,+1} + \mathcal{P}_{+1,+1}^{-1,-1}\right), \tag{7.3}$$
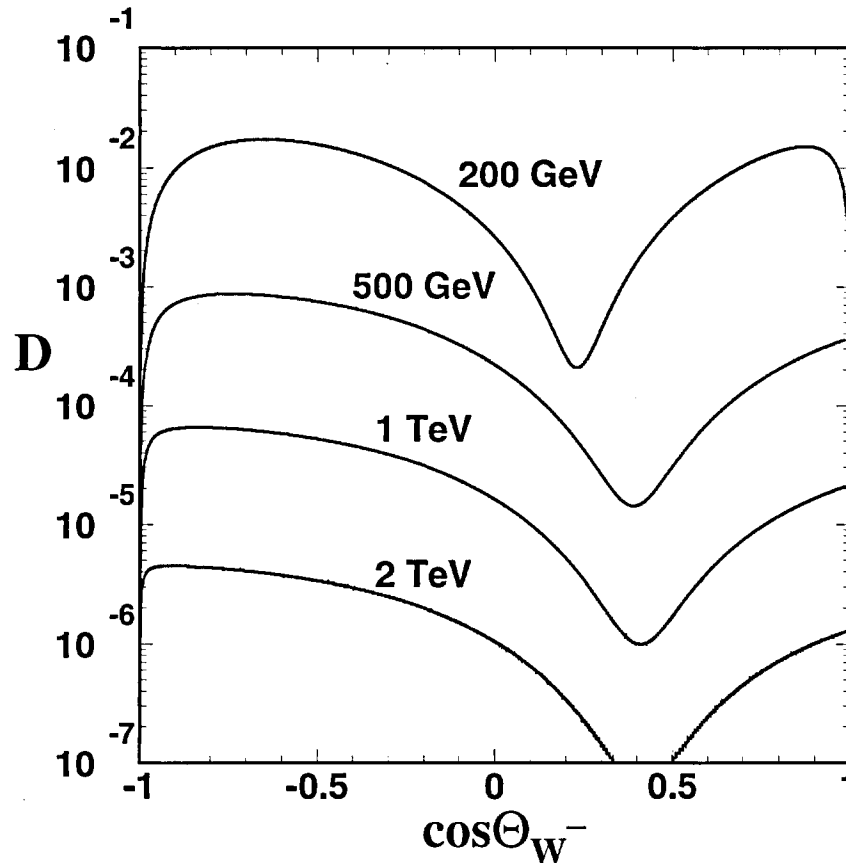
Figure 7.1: The decay plane parameter D as a function of the W^- scattering angle $\cos\Theta_{W^-}$ for center-of-mass energies of 200 GeV, 500 GeV, 1 TeV and 2 TeV. The numbers are obtained using a leading order analytical calculation.

where $\mathcal{P}$ is the production tensor from Equation 2.8 and the normalisation

$$N = \sum_{\lambda,\bar{\lambda}} |\mathcal{M}_{\lambda,\bar{\lambda}}|^2 \ . \tag{7.4}$$

Using these Equations, the decay plane correlation parameter has been calculated in leading order as a function of the energy and the W^- scattering angle[1]. Figure 7.1 shows the results of such a calculation for different centre-of-mass energies. The angular variation of D with the W^- scattering angle cannot be measured with the available statistics, also the integrated value is too small to measure. One can however perform a test for big effects, to see whether this observable shows any signs of new physics.

Figure 7.2 shows the evolution of the decay plane correlation parameter D with energy. The values have been obtained by integrating Equation 7.3 up to an energy of 1 TeV. It can be seen that D is falling strongly over this range.

---

[1]The calculations have been done using a routine which I developed for this analysis.
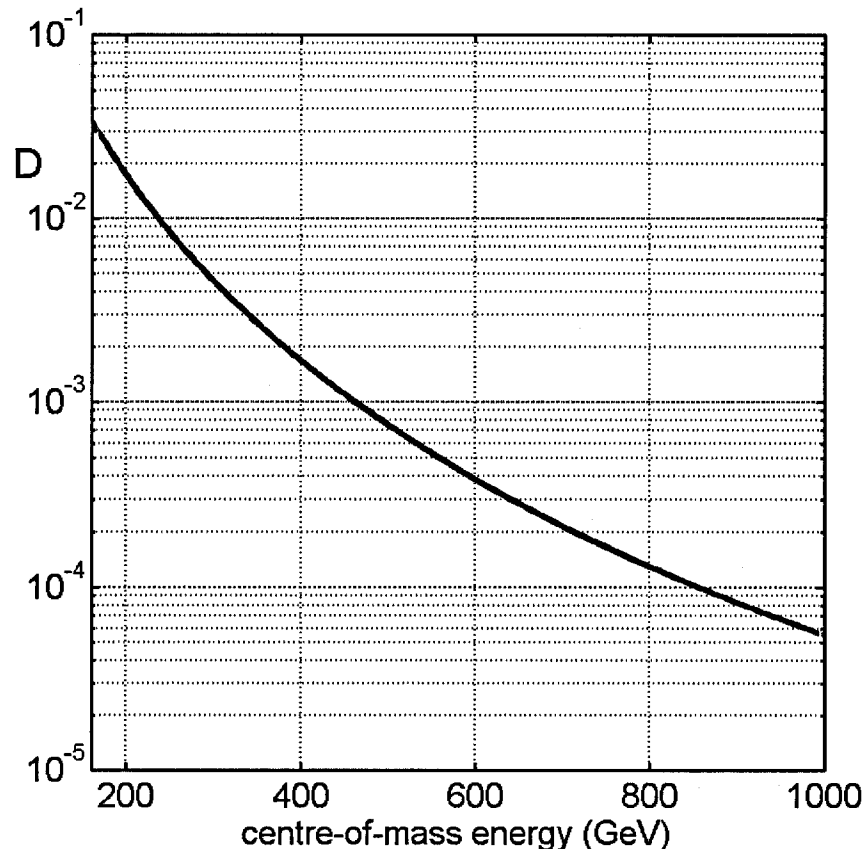
Figure 7.2: The decay plane parameter D as a function of the center-of-mass energy. The numbers are obtained using a leading order analytical calculation.

The leading order analytical calculation is used to obtain theoretical values for the parameter D for the $\sqrt{s}$ range under investigation. D varies from 0.021 at $\sqrt{s} = 189$ GeV to 0.015 at $\sqrt{s} = 209$ GeV, with a luminosity-weighted average of 0.018.

7.1.2 Monte Carlo Predictions

The Standard Model predictions are obtained from the different values of $\sqrt{s}$ using the KORALW Monte Carlo program, consistent numbers are obtained using the YFSWW Monte Carlo program.

For the $\sqrt{s}$ range under investigation and combining the $\ell\nu q_1 \bar{q}_2$ and $q_1 \bar{q}_2 q_3 \bar{q}_4$ final states, KORALW predicts $D = 0.010 \pm 0.002$, where the uncertainty is statistical. The prediction from YFSWW is $D = 0.008 \pm 0.002$. The Monte Carlo predictions differ from the analytical calculation probably due to the inclusion of radiative effects in the Monte Carlo. Various other Monte Carlo generators (EEWW, KandY, RacoonWW) were used to estimate the effects of radiative corrections on the predictions, the results however are not totally satisfactory to explain the difference. Still there is a general agreement that the size of the decay plane correlations is of the order of a few percent. As the experimental
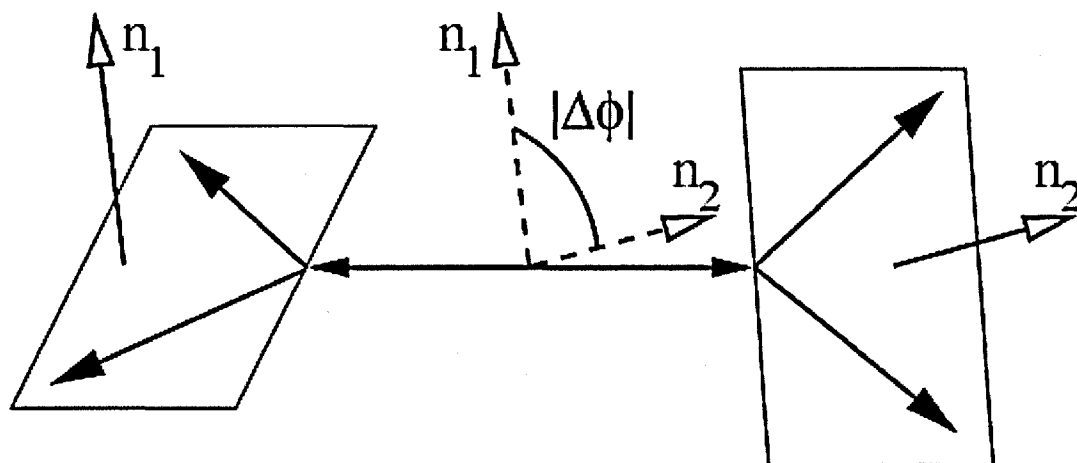
Figure 7.3: Determination of the angle $|\Delta\phi|$ between the W boson decay planes.

error will be much larger, we suggest that this problem should be investigated by the different authors of the Monte Carlo programs.

7.2   Analysis of Decay Plane Correlations

Experimentally, the angle $|\Delta\phi|$ between the decay planes is measured in the following way (see Figure 7.3): first, the normal vectors $\vec{n}_1$ and $\vec{n}_2$ to the decay planes are determined in the centre-of-mass system of the W-pair. Afterwards, $|\Delta\phi|$ is determined from the scalar product of the normal vectors:

$$\cos|\Delta\phi| = \vec{n}_1 \cdot \vec{n}_2 . \tag{7.5}$$

For $e^+e^- \rightarrow W^+W^- \rightarrow \ell\nu q_1\bar{q}_2$ events, the decay plane of the W boson decaying into leptons is determined from the lepton and the neutrino directions. The decay plane of the W boson decaying into hadrons is determined from the thrust axis of the hadrons in the W rest frame and the W flight direction.

For $e^+e^- \rightarrow W^+W^- \rightarrow q_1\bar{q}_2q_3\bar{q}_4$ events all reconstructed jets are first boosted into the centre-of-mass frame of the two W bosons. The decay planes are determined by the two jets assigned to each reconstructed W boson.

The angle $|\Delta\phi|$ between the decay planes of the two W bosons is then calculated. The reconstruction accuracies of $|\Delta\phi|$ for semileptonic and for fully hadronic events are shown in Figures 7.4 and 7.5, respectively. A fit with a Gaussian is performed in the central range of the distributions, in such a way that about 90% of the events are contained in the fit, as described in chapter 4.6. Again, the 90% range is a convention, since the quality of this fit (in terms of the χ^2) is rather poor. The result for the semileptonic events is a very small shift of -0.8 degrees and a standard deviation of 7.5 degrees. For fully hadronic events, the shift is 1.4 degrees and the standard deviation 10.0 degrees.
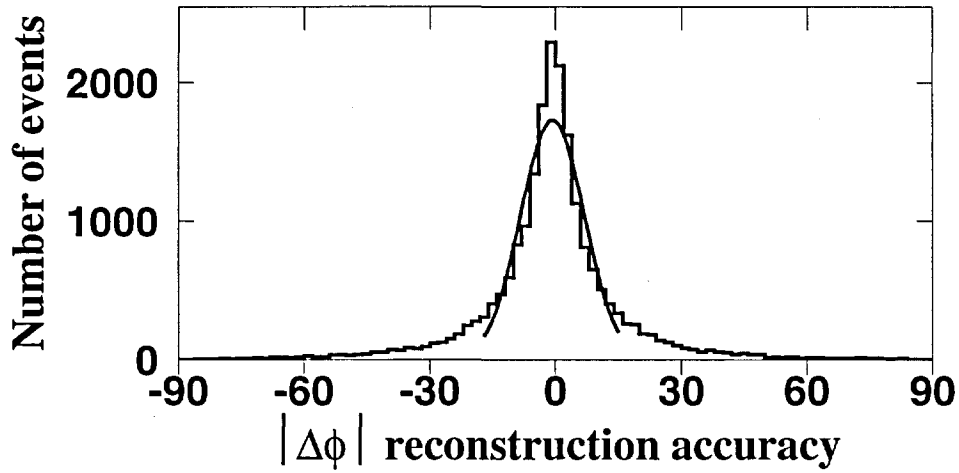
Figure 7.4: Reconstruction accuracy of $|\Delta\phi|$ in the semileptonic W^+W^- decay process at $\sqrt{s} = 189$ GeV.
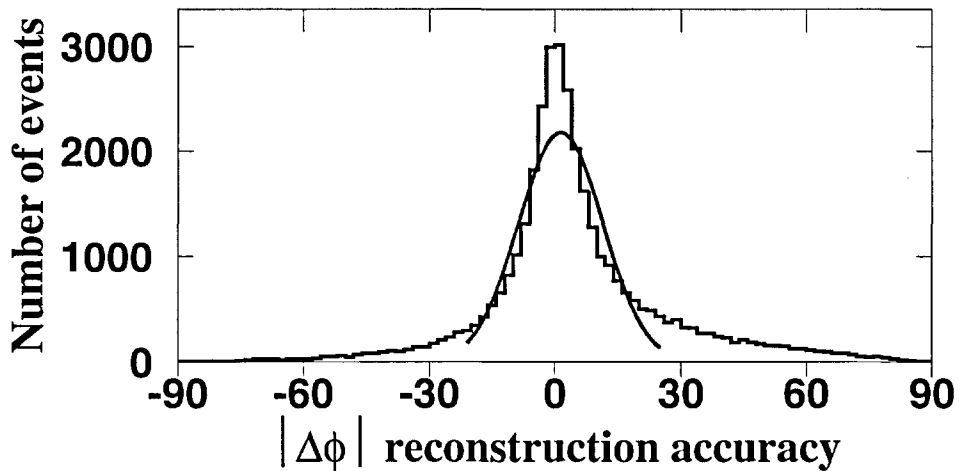
Figure 7.5: Reconstruction accuracy of $|\Delta\phi|$ in the fully hadronic W^+W^- decay process at $\sqrt{s} = 189$ GeV.

Background corrections are determined for each centre-of-mass energy bin using background Monte Carlo events that passed the selection cuts. These background distributions are normalised using the background cross-section and the collected luminosity. For $e^+e^- \rightarrow W^+W^- \rightarrow q_1\bar{q}_2q_3\bar{q}_4$ events, the background of $e^+e^- \rightarrow q\bar{q}(\gamma)$ is scaled by $+10\%$ to reproduce the measured four jet event rate of the $e^+e^- \rightarrow q\bar{q}(\gamma)$ background [63].

For the $q_1\bar{q}_2q_3\bar{q}_4$ final state, the wrongly-paired events also have to be taken into account as background on a statistical basis. For the Monte Carlo signal events, the pairing of the jets is determined using the generator information, assigning the jets directly to the generated quarks. The optimal assignment is chosen as the one with the smallest value of $\Sigma_{i=1}^4 \alpha_i$, where α_i is the angle between the reconstructed jet and the generated quark. The pairing obtained using the standard analysis method is then compared to the optimal pairing. The wrongly-paired event distributions are determined, and normalised

	$e^+e^- \rightarrow W^+W^- \rightarrow \ell\nu q_1\bar{q}_2$	$e^+e^- \rightarrow W^+W^- \rightarrow q_1\bar{q}_2q_3\bar{q}_4$
Selection	0.013	0.007
Jet pairing	—	0.011
Fit binning	0.012	0.007
Background levels	0.002	0.007
Efficiency correction	0.001	0.002
Four fermions	0.005	—
Total systematic	0.019	0.016
Statistical	0.033	0.028

Table 7.1: Systematic uncertainties on the measurement of the decay-plane correlation parameter D.

using the signal cross-section and the collected luminosity.

The $|\Delta\phi|$ distributions of the background events are consistent with flat distributions, and thus this correction only increases the statistical error. The resulting background distributions are subtracted from the raw data distributions.

The efficiency correction functions are determined for each centre-of-mass energy and include effects from selection, initial state radiation and migration. The efficiency is found to be largely independent of the values of D. No bias correction is necessary, and the data distributions are corrected by these efficiency functions.

The corrected distributions at the different centre-of-mass energies are combined and normalised. The distributions are shown for semileptonic and for fully hadronic events in Figures 7.6 and 7.7, respectively. A binned fit according to Equation 7.2 is performed.

7.3 Systematic Effects

The systematic uncertainties on the decay plane correlation parameter D are summarised in Table 7.1. The biggest sources are selection criteria, binning effects and, for fully hadronic events, the jet pairing algorithm.

The selection cuts are varied in a small range around the actual value. The corresponding variation of the helicity fractions, corrected for its statistical component as described in section 6.4, is taken as systematics.

For $e^+e^- \rightarrow W^+W^- \rightarrow q_1\bar{q}_2q_3\bar{q}_4$ events, several pairing algorithms are used as a cross-check. The largest difference in the fit results to the standard smallest mass difference algorithm (see chapter 4.5.2) arises from an approach using a neural network [58]. This difference in the fit results is taken as a systematic uncertainty.

All fits are repeated with one bin more or one bin less in the $|\Delta\phi|$ angular distributions. The average difference is retained as systematics.

Background levels are varied according to Monte Carlo statistics for the background processes. The analysis is repeated varying the background within one standard deviation, the average difference is assigned to systematic error. For $e^+e^- \rightarrow W^+W^- \rightarrow q_1\bar{q}_2q_3\bar{q}_4$

events, uncertainties on the cross-section of the background process $e^+e^- \to q\bar{q}(\gamma)$ are higher than the uncertainties due to Monte Carlo statistics. As explained in chapter 7.2, this background is scaled by $+10\%$ to reproduce the measured four jet event rate of the $e^+e^- \to q\bar{q}(\gamma)$ background. Half of the effect is retained as systematics.

Uncertainties on the efficiency corrections are determined with large KORALW Monte Carlo samples. The analysis is redone varying the efficiencies within one standard deviation on both sides. The difference is retained as systematics.

Additional contamination from the non double-resonant four-fermion final states is evaluated using the EXCALIBUR Monte Carlo. Two samples of 100000 $e\nu q_1\bar{q}_2$ events each are generated using EXCALIBUR Monte Carlo, one containing only CC03 processes and the second one containing all four-fermion final state processes mediated by at least one W boson (CC20). The analysis is redone using both samples, and the difference is retained as systematics.

7.4 Results

The corrected $|\Delta\phi|$ distributions and the fit results for semileptonic and fully hadronic events for the entire data sample are shown in Figures 7.6 and 7.7, respectively. Generally, good agreement between data and Monte Carlo distributions is found.

The resulting value of D for $e^+e^- \to W^+W^- \to \ell\nu q_1\bar{q}_2$ events is found to be $0.051 \pm 0.033 \pm 0.019$, where the first uncertainty is statistical and the second systematic. It is consistent with zero, and also in agreement with the prediction from the KORALW Monte Carlo of $D = 0.006 \pm 0.004$, where the error reflects the Monte Carlo statistics. For $e^+e^- \to W^+W^- \to q_1\bar{q}_2q_3\bar{q}_4$ events, D is found to be $-0.016\pm0.028\pm0.016$, consistent with zero, and also in agreement with the KORALW prediction of $D = 0.013 \pm 0.003$.

Combining the two decay channels, a value $D = 0.012\pm0.021\pm0.012$ is found in data, in agreement with the combined value from the KORALW Monte Carlo of $D = 0.010\pm0.002$.

In conclusion, decay-plane correlations have been studied for the first time, and, if they exist like in the Standard Model, are found to be very small. No large effect, which could hint to new physics, has been observed. However, the obtained result demonstrates how this measurement can be done and what errors can be obtained. This measurement can thus be considered as a proof of principle for future high luminosity e^+e^- colliders.
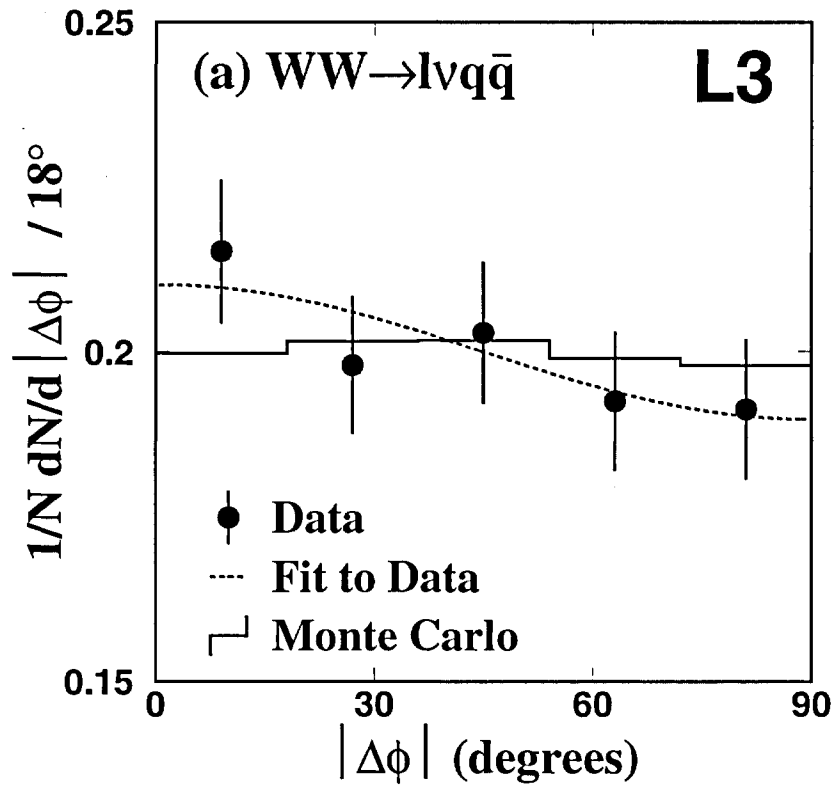
Figure 7.6: Corrected $|\Delta\phi|$ distributions for $e^+e^- \rightarrow W^+W^- \rightarrow \ell\nu q_1\bar{q}_2$ events for data and the KORALW Monte Carlo. The fit results are also shown.
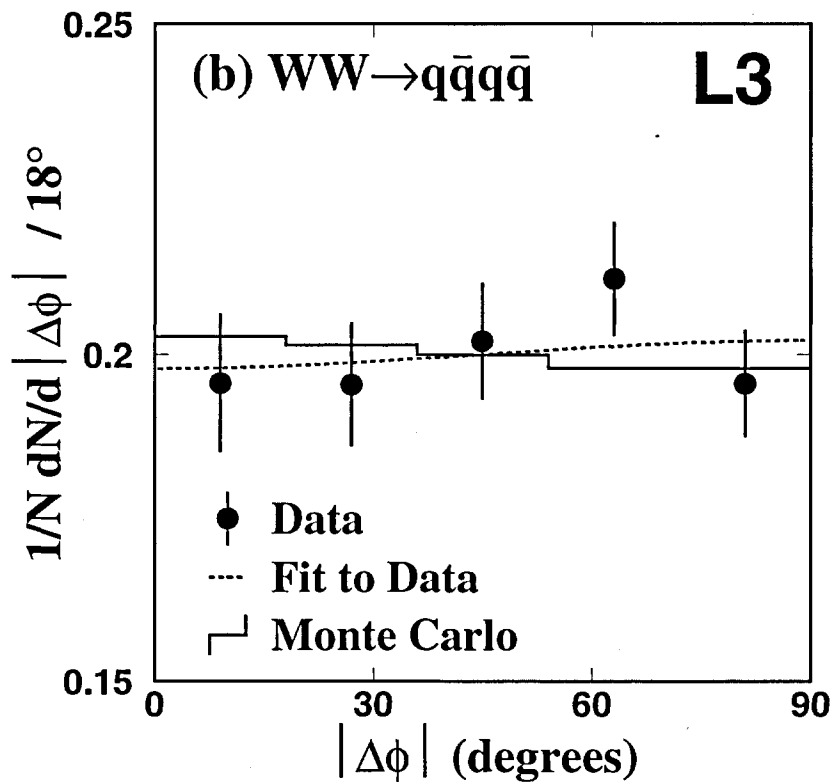

Figure 7.7: Corrected $|\Delta\phi|$ distributions for $e^+e^- \rightarrow W^+W^- \rightarrow q_1\bar{q}_2q_3\bar{q}_4$ events for data and the KORALW Monte Carlo. The fit results are also shown.

Chapter 8

Summary and Conclusions

The data collected with the L3 detector at LEP at centre-of-mass energies between 183 GeV and 209 GeV have been used to measure the helicity fractions of the W boson and to investigate W spin correlations in a model independent way. The measurement is performed using $e^+e^- \to W^+W^- \to \ell\nu q_1\bar{q}_2$ events, with ℓ denoting either an electron or a muon. The fractions of the helicity states are measured in the inclusive sample and as a function of the W^- scattering angle, $\cos\Theta_{W^-}$. For the first time, a measurement of W boson spin correlations and of decay-plane correlations is performed.

The work presented in this thesis uses a model independent technique for the measurement of the helicity composition. The data are corrected for experimental effects and background and the results can be compared directly with theoretical models.

The existence of the longitudinal W polarisation state is proved beyond doubt, and all three helicity states of the W boson are required in order to describe the data. The fraction of longitudinally polarised W bosons is measured as $(21.8 \pm 2.7 \pm 1.6)\%$, in agreement with the Standard Model Monte Carlo prediction of $(24.1 \pm 0.3)\%$. The helicity fractions and their variations as a function of the W^- scattering angle are in agreement with the Standard Model expectation. Separate analyses of the W^+ and W^- events are consistent with CP conservation.

W boson spin correlations and decay-plane correlations are measured in the data sample at centre-of-mass energies of $\sqrt{s} = 189 - 209$ GeV. Spin correlations are studied by "tagging" the helicity of the W boson which decays into hadrons and measuring the helicity of the W boson decaying into leptons. Two samples of W-pair events are formed: the first is enriched in events with transversely polarised W bosons decaying into hadrons, while the second sample is depleted of these events. W spin correlations are then measured from the difference of the two samples with respect to the helicity composition of the W boson decaying into leptons.

The data confirms the existence of spin correlations, and their size is in agreement with the Standard Model predictions. The strongest spin correlations are found for the range $0.3 \le \cos\Theta_{W^-} \le 0.9$ of the W^- scattering angle. The fraction of W bosons with helicity -1 varies by $(-32 \pm 12)\%$ and the fraction of W bosons with helicity 0 varies by $(28 \pm 16)\%$ between the two W-pair samples, corresponding to a significance of 2.7 and 1.8 standard deviations, respectively.

Furthermore, WW decay-plane correlations are studied as a "proof of concept", using a parametrisation of the azimuthal angle between the two decay planes of the W bosons. The Standard Model predicts small correlations, not accessible with the size of the data sample collected at LEP. Any large decay-plane correlations would therefore be due to new physics. The results obtained using $e^+e^- \to W^+W^- \to \ell\nu q_1 \bar{q}_2$ and $e^+e^- \to W^+W^- \to q_1\bar{q}_2 q_3\bar{q}_4$ events are in agreement with zero or small correlations and thus with the Standard Model prediction.

The presented analyses of the helicity states of W bosons, together with the measurements of triple gauge couplings and of the spin density matrix which have been performed by the LEP collaborations complete the picture of the structure of the ZWW and γWW vertices in the $e^+e^- \to W^+W^-$ process. No signs of new physics have been observed within the precision which was achievable at LEP II.

The techniques used and developed in this work could be fully exploited at a future high-luminosity linear e^+e^- collider, which would operate at centre-of-mass energies up to several TeV.

Bibliography

[1] L3 Collaboration, M. Acciarri *et al.*, *Direct Observation of Longitudinally Polarised $W^{\pm}$ Bosons*, Phys. Lett. **B 474** (2000), 194, and CERN-EP/99-176.

[2] R.Ofierzynski, *Evidence for WW-Spin Correlations with L3 at LEP*, Diploma Thesis, ETH Zürich (2000), L3 Note 2536.

[3] L3 Collaboration, P. Achard *et al.*, *Measurement of W Polarisation at LEP*, Phys. Lett. **B 557**, 147, and CERN-EP/2002-092, and hep-ex/0301027.

[4] L3 Collaboration, P. Achard *et al.*, *Study of Spin and Decay-Plane Correlations of W Bosons in the $e^+e^- \to W^+W^-$ Process at LEP*, Eur. Phys. J. **C** (2005), DOI: 10.1140/epjc/s2005-02137-9, CERN-EP/2003-072, and hep-ex/0501036.

[5] S. L. Glashow, *Partial Symmetries of Weak Interactions*, Nucl. Phys. **22** (1961) 579.

[6] S. Weinberg, *A Model of Leptons*, Phys. Rev. Lett. **19** (1967) 1264.

[7] A. Salam, in *Elementary Particle Theory*, ed. N. Svartholm, Stockholm, Almqvist and Wiksell (1968), 367.

[8] F. Halzen, A.D. Martin, *Quarks & Leptons: An Introductory Course in Modern Particle Physics*, John Wiley & Sons, New York, 1984.

[9] M. Chanowitz and M.K. Gaillard, Nucl. Phys. **B 261** (1985) 379.

[10] H. Veltman, Phys. Rev. **D 41** (1990) 2294; Phys. Rev. **D 43** (1991) 2236.

[11] UA1 Collaboration, G. Arnison *et al.*, *Experimental Observation of Isolated Large Transverse Energy Electrons with Associated Missing Energy at $\sqrt{s} = 540$ GeV*, Phys. Lett. **B 122** (1983) 103.

[12] UA2 Collaboration, M. Banner *et al.*, *Observation of Single Isolated Electrons of High Transverse Momentum in Events with Missing Transverse Energy at the CERN $p\bar{p}$ Collider*, Phys. Lett. **B 122** (1983) 476.

[13] UA1 Collaboration, G. Arnison *et al.*, *Experimental Observation of Lepton Pairs of Invariant Mass around 95 GeV/c^2 at the CERN SPS Collider*, Phys. Lett. **B 126** (1983) 398.

[14] UA2 Collaboration, P. Bagnaia *et al.*, *Evidence for $Z \to e^+e^-$ at the CERN $p\bar{p}$ Collider*, Phys. Lett. **B 129** (1983) 130.

[15] CDF Collaboration, F. Abe *et al.*, *Observation of Top Quark Production in $p - \bar{p}$ Collisions with the Collider Detector at Fermilab*, Phys. Rev. Lett. **74** (1995) 2626.

[16] D0 Collaboration, S. Abachi *et al.*, *Observation of the Top Quark*, Phys. Rev. Lett. **74** (1995) 2632.

[17] DONUT Collaboration, K. Kodama *et al.*, *Observation of Tau Neutrino Interactions*, Phys. Lett. **B 504** (2001) 218, hep-ex/0012035.

[18] The LEP Collaborations ALEPH, DELPHI, L3, OPAL, the LEP Electroweak Working Group, the SLD Electroweak and Heavy Flavour Groups, *A Combination of Preliminary Electroweak Measurements and Constraints on the Standard Model*, December 2004, CERN-PH-EP/2004-069, and hep-ex/0412015.

[19] The L3 Collaboration, O. Adriani *et al.*, *Results from the L3 Experiment at LEP*, Phys. Rep. **236** (1993) 1.

[20] ALEPH, DELPHI, L3 and OPAL Collaborations, the LEP Working Group for Higgs Boson Searches, *Search for the Standard Model Higgs Boson at LEP*, CERN-EP/2003-011.

[21] Joint LEP2 SUSY Working Group webpage, http://lepsusy.web.cern.ch/lepsusy/.

[22] LEP Exotica Working Group webpage, http://lepexotica.web.cern.ch/LEPEXOTICA/.

[23] K. Hagiwara *et al.*, Phys. Rev. D 66, 010001 (2002) and 2003 off-year partial update for the 2004 edition available on the PDG WWW pages (URL: http://pdg.lbl.gov/).

[24] Z. Ajaltouni *et al.*, *Triple Gauge Boson Couplings*, 1996, CERN Yellow Reports 96-01, Vol.1 (Physics at LEP2), 525.

[25] L3 Collaboration, P. Achard *et al.*, *Measurement of Triple-Gauge-Boson Couplings of the W Boson at LEP*, Phys. Lett. **B 586** (2004) 151.

[26] M. S. Bilenky, J. L. Kneur, D. Schildknecht, *Trilinear couplings among the electroweak vector bosons and their determination at LEP-200*, Nucl. Phys. **B 409** (1993), 22.

[27] G. Gounaris, D. Schildknecht, F. M. Renard, *Genuine tests of CP invariance in $e^+e^- \to W^+W^-$*, Phys. Lett. **B 263** (1991), 291.

[28] G. Gounaris, J. Layssac, G. Moultaka, F. M. Renard, *Analytic expressions of cross-sections, asymmetries and W density matrices for $e^+e^- \to W^+W^-$ with general three boson couplings*, Int. J. Mod. Phys. **A 8** (1993), 3285.

[29] L3 Collaboration, E. Delmeire, *Spin Density Matrix Analysis in W-pair Production at $\sqrt{s}$ = 189 - 209 GeV*, March 2003, L3 Note 2793.

[30] OPAL Collaboration, G. Abbiendi *et al.*, *W Boson Polarisation at LEP2*, PL B **585** (2004) 223.

[31] DELPHI Collaboration, C. De Clercq, *Study of W boson polarisations in the reaction $e^+e^- \to W^+W^-$ at energies between 189 and 208 GeV*, June 2003, DELPHI 2003-052 CONF 672.

[32] F.A. Bardin, R. Kleiss, R. Pittau, Nucl.Phys. B **424** (1994) 308.

[33] K. Hagiwara, R.D. Peccei, D. Zeppenfeld and K. Hikasa, *Probing the Weak Boson Sector in $e^+e^- \to W^+W^-$*, Nucl. Phys. B **282** (1987), 253.

[34] M. Bourquin *et al.*, Preprint 86-02, ECFA, 1981.

[35] R. W. Assmann, *LEP Operation and Performance with Electron-Positron Collisions at 209 GeV*, Proceedings of the 11th Chamonix Workshop on LHC.

[36] B. Adeva *et al.*, *The Construction of the L3 Experiment*, Nucl. Inst. Meth. A **289** (1990) 35.

[37] M. Acciarri *et al.*, *The L3 Silicon Microvertex Detector*, Nucl. Inst. Meth. A **351** (1994) 300.

[38] A. Adam *et al.*, *Performance on Test Beam of the L3 Double Sided Silicon Microstrip Detector*, Nucl. Inst. Meth. A **348** (1994) 436.

[39] F. Beissel *et al.*, *Construction and Performance of the L3 Central Tracking Detector*, Nucl. Inst. Meth. A **332** (1993) 33.

[40] R.L. Gluckstern, *Uncertainties in Track Momentum and Direction, due to Multiple Scattering and Measurement Errors*, Nucl. Inst. Meth. **24** (1963), 381.

[41] K. Deiters *et al.*, *The Construction and Performance of a Large Cylindrical Wire Chamber with Cathode Readout*, Nucl. Inst. Meth. A **323** (1992) 162.

[42] J. Bakken *et al.*, *Study of the Energy Calibration of a High Resolution Electromagnetic Calorimeter*, Nucl. Inst. Meth. A **280** (1989) 25.

[43] G. Basti *et al.*, *The L3 Lead-Scintillating Fiber Calorimeter*, Nucl. Inst. Meth. A **374** (1996) 293.

[44] The L3 Collaboration, O. Adriani *et al.*, *Hadron Calorimetry in the L3 Detector*, Nucl. Inst. Meth. A **302** (1991) 53.

[45] B. Adeva *et al.*, *A High Resolution Muon Detector*, Nucl. Inst. Meth. A **323** (1992) 109.

[46] S. Lanzano *et al.*, *Test Results of the L3 Precision Muon Detector*, Nucl. Inst. Meth. **A 289** (1990) 335.

[47] M. Fabre, *The Dimuon Mass Resolution of the L3 Experiment at LEP*, ETH Zürich, Ph.D. Thesis 9696 (1992).

[48] A. Adam *et al.*, *The Forward Muon Detector of L3*, Nucl. Inst. Meth. **A 383** (1996) 342.

[49] I.C. Brock *et al.*, *Luminosity Measurement in the L3 Detector at LEP*, Nucl. Inst. Meth. **A 381** (1996) 236.

[50] The L3 detector simulation is based on GEANT version 3.21; R. Brun *et al.*, *GEANT 3*, preprint CERN DD/EE/84-1 (1984), revised 1987.

[51] H.Fesefeldt, RWTH Aachen Preprint PITHA 85/02 (1985).

[52] PYTHIA version 5.722 is used.
T. Sjöstrand, *PYTHIA 5.7 and JETSET 7.4 Physics and Manual*, CERN-TH/7112/93 (1993), revised August 1995; Comp. Phys. Comm. **82** (1994) 74.

[53] KORALW version 1.42 is used.
M. Skrzypek, S. Jadach, W. Placzek and Z. Wąs, Comp. Phys. Comm. **94** (1996) 216;
M. Skrzypek, S. Jadach, M. Martinez, W. Placzek and Z. Wąs, Phys. Lett. **B 372** (1996) 289;
S. Jadach, W. Placzek, M. Skrzypek, B.F.L. Ward and Z. Wąs, CERN-TH/98-242.

[54] EEWW version 1.1 is used;
J. Fleischer *et al.*, Comput. Phys. Commun. **85** (1995) 29.

[55] YFSWW3 version 1.14 is used;
S. Jadach *et al.*, Phys. Rev. **D 54** (1996) 5434; Phys. Lett. **B 417** (1998) 326; Phys. Rev. **D 61** (2000) 113010; UTHEP-00-0101, CERN-TH/2000-337, hep-ph/0007012 to be submitted to Phys. Lett. **B**.

[56] EXCALIBUR version 1.11 is used;
F.A. Berends, R. Kleiss and R. Pittau, Nucl. Phys. **B 424** (1994) 308; Nucl. Phys. **B 426** (1994) 344; Nucl. Phys. (Proc. Suppl.) **B 37** (1994) 163;
R. Kleiss and R. Pittau, Comp. Phys. Comm. **83** (1994) 141;
R. Pittau, Phys. Lett. **B 335** (1994) 490.

[57] KK2F version 4.12 is used;
S. Jadach, B. F. L. Ward and Z. Wąs, Comp. Phys. Comm. **130** (2000) 260.

[58] L. Malgeri, private communication.

[59] S. Catani *et al.*, Phys. Lett. **B 269** (1991) 432;
S. Bethke *et al.*, Nucl. Phys. **B 370** (1992) 310.

[60] S. Moretti, L. Lönnblad, T. Sjöstrand, *New and Old Jet Clustering Algorithms for Electron-Positron Events*, hep-ph/9804296.

[61] M.J. Duncan, G.L. Kane, W.W. Repko, *New Standard-Model Test for Future Colliders*, Phys. Rev. Lett. **55** (1985), 773.

[62] M.J. Duncan, G.L. Kane, W.W. Repko, *WW Physics at Future Colliders*, Nucl. Phys. **B 272** (1986), 517.

[63] L3 Collaboration, M. Acciarri *et al.*, *Measurement of the W-pair Production Cross Section and W-Decay Branching Fractions in e^+e^- Interactions at $\sqrt{s} = 189$ GeV*, Phys. Lett. **B 496** (2000), 19, and CERN-EP/2000-104.

[64] R.Ofierzynski, *Measurement of W Polarisation with L3 at LEP*, in *Particles and the Universe, Proceedings of the 18th Lake Louise Winter Institute 2003*, World Scientific (2004).

[65] R.Ofierzynski, *W Polarisation Studies at LEP2*, Proceedings of the International Europhysics Conference on High Energy Physics 2003, Aachen, Germany, Eur. Phys. J. **C 33**, (2004), 714.

Seite Leer /
Blank leaf

Acknowledgements

Seite Leer /
Blank leaf

Curriculum Vitae

Personal Data

Date and place of birth: 29. November 1973, Poznań (Poland)

Nationality: Polish

Education

1980 – 1981   Primary school in Poznań, Poland

1981 – 1984   Primary school in Aachen, Germany

1984 – 1987   Secondary school (Gymnasium) in Aachen, Germany

1987 – 1989   Secondary school in Neuhausen am Rheinfall, Switzerland

1989 – 1994   High school (Kantonsschule) in Schaffhausen, Switzerland

1994 – 2000   Study of Physics at the Swiss Federal School of Technology (ETH) in Zürich, Switzerland. Diploma in Physics [2], April 2000.

2000 – 2005   Ph.D. thesis (this work) at the Institute of Particle Physics, performed at the European Centre for Nuclear Research (CERN) in the framework of the L3 experiment at LEP. Author of various L3 internal notes submitted to main conferences, conference proceedings ([64, 65]), main author of two publications with the L3 collaboration ([3, 4]).
Participation in the software development for the Detector Control System of the electromagnetic calorimeter of the CMS experiment at LHC.